Research on an improved Overhauser magnetometer

Huan Liu[1,2] **and Haobin Dong**[1,2]

[1]School of Automation, China University of Geosciences, Wuhan, China

[2]Hubei Key Laboratory of Advanced Control and Intelligent Automation for Complex Systems, Wuhan, China

Key Points:

- The noise model of FID signal is first established and different types of noises are investigated, including white noise, narrow-band noise, phase noise, colored noise, random noise and singular noise
- A high-precision multi-channel frequency measurement algorithm is designed
- A new secondary tuning algorithm based on the SVD and STFT is proposed

Corresponding author: Haobin Dong, donghb@cug.edu.cn

Abstract

Background: The Overhauser magnetometer based on dynamic nuclear polarization (DNP) effect is a high-precision device for weak magnetic field measurement. The Larmor precession of excited protons around the geomagnetic field can generate a free induction decay (FID) signal. The strength of the magnetic field can be obtained by measuring the frequency of this signal. However, with the advances in the exploration technology, there is a need for the Overhauser magnetometer to have higher accuracy and higher sensitivity.

Methods: The goal of this work is trying to research on an improved Overhauser magnetometer with higher accuracy and sensitivity. Our approach is characterized by four key components: 1) the noise model of FID signal is established and different types of noises are investigated. Moreover, the measurement error has been analyzed and the measurement accuracies effected by different signal to noise ratios (SNRs) are determined; 2) a multi-channel frequency measurement algorithm is developed to improve the accuracy of the measured magnetic fields in a broader dynamic range and in a noisier environment; 3) a secondary tuning algorithm based on singular value decomposition (SVD) and shot time Fourier transform (STFT) is designed, which cannot only improve the accuracy of the sensor's tuning but also shorten the time of tuning process; 4) numerous laboratory and field tests on the developed prototype including noise level, frequency measurement accuracy, magnetic field measurement accuracy, geomagnetic observation and ferromagnetic target localization compared with one of the commercially available Overhauser magnetometers in the world market are conducted.

Results: The relationship between the total noise model of FID signal and the error of frequency measurement is formulated in a quantitative way. The simulation results show that when the SNR reached up to 10 dB, the improvement of accuracy is not obvious while in the field tests, the SNR is about 30 dB. As a whole, the trend of the simulation and the field test results are approximately consistent. The absolute error measured by the proposed frequency measurement algorithm is about 7.75 times smaller than that measured by the original method with a single channel. In addition, the sensitivity is reduced to 0.036 nT, which is improved by 11.4 times. The proposed tuning algorithm has higher accuracy and higher speed than the current commonly used methods, peak detection and auto-correlation, even in the interferential environment. It makes up for the insufficiency of the existing tuning methods by improving the magnetometer's ability to adapt to the environment, thereby solving the detuning phenomenon in the process of measurement. The longtime geomagnetic observational data recorded by the prototype and a commercial Overhauser magnetometer confirm that, the proposed device has a mean square error (a little larger than 0.3 nT) that is close to one for the commercial magnetometer (no more than 0.3 nT). Furthermore, the prototype shows a strong ability in magnetic anomaly detection and localization. The integrative structure is adopted, which can ensure the convenience and reliability of operation in the field.

Keywords: Optimization of Overhauser magnetometer, free induction decay signal, noise modeling, secondary tuning, multi-channel frequency measurement.

Contents

List of Figures

List of Tables

Chapter 1

Introduction

1.1 Background

Continuous observations of the geomagnetic are carried out with the characteristic times spanning from seconds to decades at magnetic observations [1]. Likewise, the natural elements such as ore, iron, etc., which have different magnetic properties, will lead to the magnetic field anomalies [2]. A proton precession magnetometer is used to measure a slowly varying or constant weak magnetic field. It is the oldest instrument in the history of quantum weak magnetic measurement instruments [3], and has been one of the most widely used geomagnetic survey instruments for more than half a century due to its easy operation and superior stability [4]. A certain excitation condition is adopted to keep the proton in the solution of the sensor alive, and the proton's Larmor precession around the geomagnetic field can generate a free induction decay (FID) signal in the sensor after turning off the excitation condition [5]. Because the FID signal frequency is proportional to the strength of the magnetic field, the value of the magnetic field can be obtained by measuring the frequency of the FID signal after being amplified, filtered, and wave-shaped [6]. According to the different principles of excitation, proton precession magnetometers are divided into two types: ordinary proton magnetometers and Overhauser magnetometers. They are widely used in space exploration [7], near-surface exploration [8], ocean exploration [9], military technology [10] and more [11–13]. The Overhauser magnetometer can be regarded as an improved proton magnetometer based on the principle of dynamic nuclear polarization (DNP) effect. This type of magnetometers have the advantages of low power consumption, high accuracy, high sensitivity, etc.

The resolution of an ordinary proton magnetometer is 0.1 nT and the accuracy is 1.0 nT, while that of an Overhauser magnetometer are 0.01 nT and 0.1 nT, respectively. However, with the advances in the exploration technology, there is a need for the Overhauser magnetometer to have higher accuracy and higher sensitivity[14,15].

1.2 Related Work

The proton precession magnetometer belongs to a branch of the atomic magnetometer as shown in Figure 1-1. According to different principles, the atomic magnetometers mainly consist of nuclear precession magnetometer and optical pumping magnetometer. The proton precession magnetometer has the advantages such as power consumption, high sensitivity, simple operation and superior stability. The optically pumped magnetometer has the advantages of high sensitivity and fast response, whereas it is of the drawbacks such as large power consumption, complex apparatus (light source and lens system), need of preheating, and heading error[16–18], hence it is not advisable for a portable instrument. Whereas the nuclear precession magnetometer could meet the requirements of high precision, small size, low power consumption for field magnetic prospecting. Furthermore, the proton magnetometer and Overhauser magnetometer both belong to the nuclear precession magnetometer.

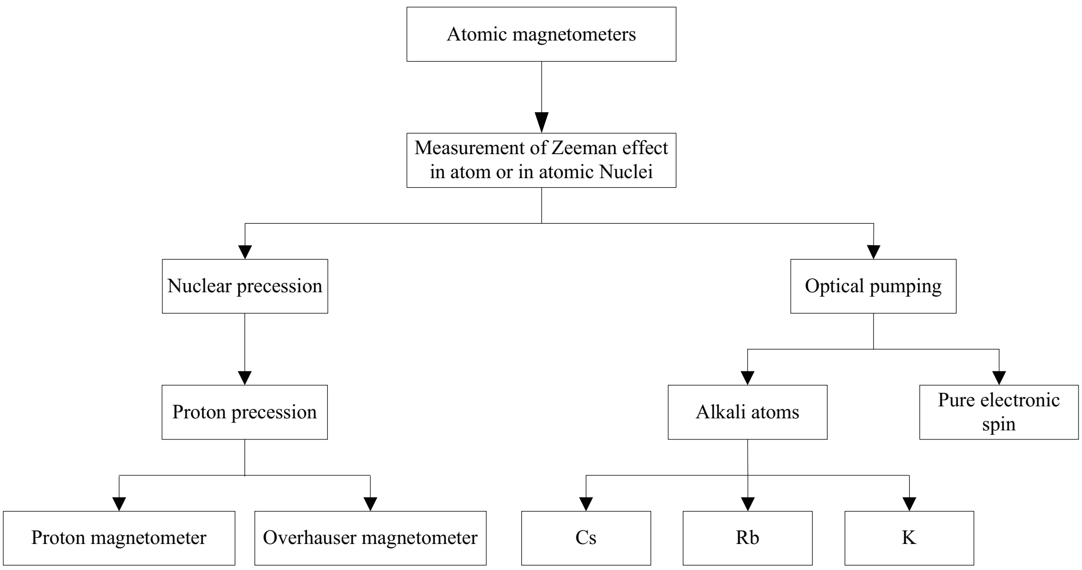

Figure 1-1: The branches of atomic magnetometer.

In 1954, M.Packard and R.Varian first invented the proton precession magnetometer[19,20]. This kind of magnetometer adopt discontinuous measurement, the sensitivity was 0.1 nT and the accuracy was 1 nT. It had advantages including high sensitivity, high precision, easy operation, stable and durable performance. However, there were also various limitations such as long period, high power consumption, etc. It was gradually replaced by the Overhauser magnetometer.

The Overhauser effect was first discovered by A.W.Overhauser in 1953[21], while Slichter gave the first demonstration. Afterwards, Abragam further investigated the Overhauser effect in nonmetals and paramagnetic liquids[22]. Furthermore, several researchers have developed the magnetometers based on the Overhauser effect. Duret et al. designed an Overhauser magnetometer based on the self-oscillating method for the Oersted satellite[23–25]. The magnetometer is still operational; however, its design was not described in great detail. This self-oscillating structure is composed of two flasks, which contain a pair of solvents, and requires an additional feedback circuit to feed the proton precession signal back to the coils to produce the continuous polarization field; hence, the major advantage over this method is great speed in following magnetic field changes. This may require a more complex design, a larger volume and higher power consumption. Using a brief diagram, Sapunov[26] and Hrvoic[27,28] simply introduced the differences between the proton magnetometer and the Overhauser magnetometer, and preliminarily analyzed the absolute and random errors, thermal effects and calibration. However, the design of the Overhauser magnetometer was not mentioned. In the early 1960s, A. Abragam and I. Solomon applied patents for the manufacture of magnetometers using Overhauser effect[29]. In the 1980s, France, Canada and Russia developed the Overhauser magnetometers in succession and applied them to the surface, ocean and satellite[30–32]. The Oersted satellite launched by Denmark in 1999[33], the CHAMP satellite launched by Germany in 2000[34] even the helicopter and anti-submarine aircraft were all equipped with the Overhauser magnetometer developed by Atomic Energy Commission of French. To date, numerous commercial Overhauser magnetometers have been invented. The POS series[5] developed by the Russia Quantum lab and GSM-19 series[35] developed by Canada GEM company have already been commercialized, which are leading the way in the research of Overhauser magnetometer. There are lots of literature report the geomagnetic observatories that constructed by the instruments from the both series. However, the contents are all about their technology application and data analysis, few of them report the related tutorials on how to develop the device. However, with the advances in the exploration technology, the performance of Overhauser magnetometer could not meet the requirements of some applications.

To sum up, although there are some commercial Overhauser magnetometers, few published papers and patents involve any detailed design[37,38].

Since 2000, domestic (refer to China) research in the area of instruments for weak magnetic detection has made great achievements, especially some research institutions and manufacturers have developed ordinary proton magnetometers such as CZM-4, WCZ-3, etc.[39,40], while there were no reports about the Overhauser magnetometer. To date, China has no commercial Overhauser magnetometer products, and the number of theoretical and technical literature is too little due to the foreign technology embargo. In addition, the development of an Overhauser magnetometer involves numerous specialized fields so that it is difficult to make a core technology research from the principle.

Dong and Tan developed a prototype of Overhauser magnetometer[41] and applied for a patent on it[42]. A gradiometer based on Overhauser effect was proposed in[43] and the detection technology of near-surface unexploded ordnance (UXO) using it was presented in[44]. Furthermore, the simulation research on an RF circuit for excitation[45], the development of a JOM-1 model Overhauser magnetometer[46], the noise characteristics research of the sensor[47] and other related studies[48–50] were proposed and well accepted. However, due to some of the key technologies cannot be grasped, the measurement accuracy is relatively low so that the domestic use of Overhauser magnetometers all rely on imports currently.

1.3 Existed Problem

Generally, an Overhauser magnetometer always needs a radio frequency (RF) excitation to obtain the Larmor precession signal[21]. The excitation system is one of the critical factors that determine the quality of sensing signal. For the excitation solution in the sensor, the nitroxide free radical usually acts as the main sample, which contains hydrogen, electron and nitrogen are commonly used due to its stable chemical property[51]. Related research only considers the energy transfer between hydrogen and electrons[43,46,52,53]. The sensor implements the double resonance of the unpaired electron spin system and the hydrogen proton spin system to obtain the FID signal. However, the energy transfer is incomplete. Since nitrogen is relatively close to electrons and can be polarized in the same frequency, the nitrogen should not be ignored[54].

Recently, the development of a high-precision Overhauser magnetometer has attracted many researchers' attention. Current worldwide research has reported that there still exist the following problems.

- Due to the fast decay of FID signal, the effective time is less than one second, especially when there exist magnetic field anomalies. Hence, how to extract the center frequency of FID signal effectively and accurately in a short time still remains a problem to be overcome.

- Basically, the accuracy of frequency measurement will increase with the SNR of the FID signal. However, such relationship has not been well identified and should be further investigated.

- The frequency measurement time is limited due to the fast decay of FID signal, so how to reach a higher accuracy of frequency measurement in a short time is also a problem to be overcome.

1.4 Organization of the Thesis

Writing a thesis about the critical techniques for an improved Overhauser magnetometer including different architectures, algorithms, mathematical modules is not an straight forward task. I tried to make the reader familiar with the sufficient background whenever needed. Thinking about design an Overhauser magnetometer without a background in electrical & instrumentation, DNP theory and to some extent the optimization, is rather impossible.

Starting with a brief introduction to the proton precession magnetometer and its applications in different areas. A complete discussion and overview about the related work in domestic and foreign is taken place in chapter 1.

In chapter 2, the basic concepts of Overhauser nuclear effect and Larmor precession signal are introduced, respectively, focused mainly on a conceptual understanding of the whole DNP procedure and the corresponding derivation process.

In chapter 3, the design and development of the improved Overhauser magnetometer are discussed briefly. An alternative design of a geomagnetic sensor with differential dual-coil structure is proposed. In addition, a test apparatus for measuring the critical parameters of this sensor is developed. The signal acquisition and processing system including the polarization unit and signal conditioning unit are presented. Furthermore, the theoretical calculation of the sensor and preamplifier noise is implemented.

In chapter 4, the first objective of this section is to establish different types of noise models for the FID signal, which are further applied to evaluate the influence of noise on the FID signal quality. Simulation is first conducted to identify how the measurement accuracy effected by different SNRs. Moreover, the error for the frequency measurement of the FID signal has been analyzed and the measurement accuracy for the SNR of the amplified FID signal is determined. The second objective is to develop a multi-channel frequency measurement algorithm to improve the accuracy of the measured magnetic fields in a broader dynamic range and in a noisier environment. The third objective is to propose a secondary tuning algorithm based on singular value decomposition (SVD) and shot time Fourier transform (STFT), which cannot only improve the accuracy of the sensor's tuning but also shorten the time of tuning process.

In chapter 5, numerous laboratory and field tests on the proposed prototype including noise level, frequency measurement accuracy, magnetic field measurement accuracy, geomagnetic observation in 24 h and ferromagnetic target localization compared with one of the commercially available Overhauser magnetometers in the world market are conducted. A specific discussion and expectation about the Overhauser magnetometer is taken place in chapter 6.

Multiple sources and references (more than 100 references) have been used, this provides readers with different possible approaches which makes the comparisons more sensible. For instance, in the case of frequency measurement algorithm in chapter 4, several existing and proposed methods for FID signal are discussed, or in the case of tuning algorithm, both philosophical-historical background and practical point of view are considered.

Chapter 2

Theory

In this chapter, the basic concepts of Overhauser nuclear effect and Larmor precession signal are introduced, respectively, focused mainly on a conceptual understanding of the whole optimized dynamic nuclear polarization (DNP) procedure.

2.1 Dynamic Nuclear Polarization

The DNP effect was first discovered by Overhauser in 1953[21]. Slichter et al. gave the first demonstration of the DNP effect. Afterwards, Abragam et al. further investigated the DNP effect in nonmetals and paramagnetic liquids[22]. At present, the DNP effect is widely used in nuclear magnetic resonance (NMR) experiments, with a view toward being applied in medicine and chemistry.

According to the basic theory of NMR and quantum, in the motion of spin, the magnetic moment of electron and nucleus spins are not continuous but quantized[24], and taking the proton as example, there are only two energy levels (assume them are E_1 and E_2 respectively) of the proton magnetic moment μ_p, and the energy gap is:

$$\Delta E = E_2 - E_1 \tag{2.1}$$

where, γ is the proton gyromagnetic ratio, which is a constant and only has relationship with the charge and the mass of the proton, h is the Planck constant. When the proton is put into a external magnetic field B_0, a torque $\mu_p \times B_0$ is produced, which causes that the proton acts as a gyroscope rotating with Larmor precession around B_0. Where the

Larmor angular frequency of the proton is ω, according to Bloch equation there is[21]:

$$\omega_p = \gamma_p B_0 \tag{2.2}$$

where, ω_p is the angular frequency of proton. Based on this equation above, ω_p is proportional to B_0, and only by measuring ω_p could the value of B_0 be obtained.

When the external magnetic field is weak, due to the thermal motion of lattices, the proton magnetic moments drift off the external magnetic field and distribute randomly, which makes the macro proton magnetic moment $\boldsymbol{M}_p$ is very weak in thermal equilibrium, hence it is very arduous to receive the FID signal directly. At present, the continuous wave and pre-polarization method are usually used to realize the enhancement of the macro moment, which could strengthen the FID signal.

The continuous wave method is shown in Figure 2-1a, according to the NMR theory, when a radio frequency (RF) alternating field is imposed on the direction which is perpendicular to B_0 at a frequency f_r, and the RF field obey the following equation:

$$\Delta E = h f_r \tag{2.3}$$

In this case, the RF field could saturate the proton spin relaxation between two levels, hence the initial phase of proton spin changes from random distribution to be in the same direction, which implies the enhancement of $\boldsymbol{M}_p$. In the Larmor precession, $\boldsymbol{M}_p$ cut a receiving coil periodically to change the magnetic flux of coil, then an induced electromotive force is generated in the receiving coil, accordingly the FID signal is extracted. Subsequently, the magnetic field measurement could be realized through the detection circuit and cymometer.

Since the energy splitting is rather small in the magnetic field of which intensity is below about 50 mT, when the continuous wave method measures the weak geomagnetic field, the SNR of the FID signal is very low, which leads to low magnetic sensitivity, hence it is not suitable for weak geomagnetic field measurement but could be used to measure the strong magnetic field.

Aiming at the insufficient of the continuous wave method, the pre-polarization method is ordinarily tried to further enhance the FID signal[55]. As shown in Figure 2-1b, the axis of the polarizing coil is perpendicular to the external magnetic field B_0, when charg-

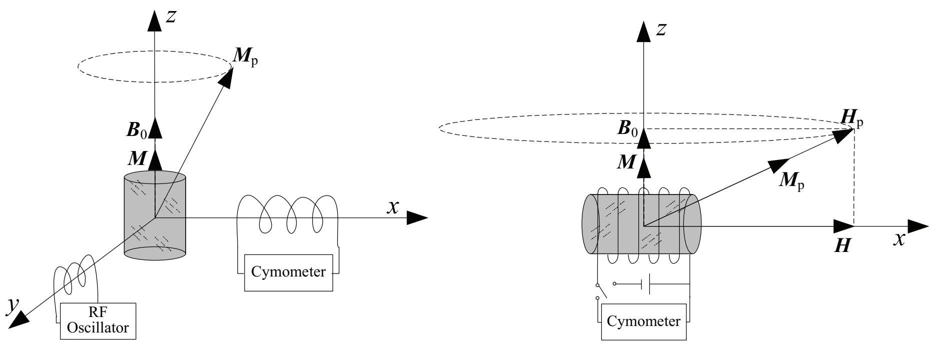

(a) Continuous wave (b) Pre-polarization

Figure 2-1: The commonly used methods for macro moment enhancement.

ing a strong direct current (DC) into the coil, a transverse polarization magnetic field $\boldsymbol{H}$ is generated, which is several hundred times larger than B_0, and then the proton spin transition is produced. Accordingly, the proton magnetic moments, which present random permutation, change from drifting off B_0 to arranging along the magnetic field $\boldsymbol{H}_p$ which consists of $\boldsymbol{H}$ and B_0. For the proton spin only has two energy levels, at this moment the phases of the proton magnetic moments keep consistent, thus a new macro moment $\boldsymbol{M}_p$ is established after several seconds of the DC polarization. If the $\boldsymbol{H}$ is suddenly withdrawn, which means DC is suddenly disconnected, after that the proton magnetic moments will soon lose their phase consistency and come back to the direction of B_0, at the same time $\boldsymbol{M}_p$ would spin around B_0 at the Larmor frequency, likewise the FID signal could be induced by the receiving coil.

Compared with the continuous wave method, the pre-polarization method could improve the magnetic sensitivity of the sensor to a certain extent, however, due to the low gyromagnetic ratio of the proton, it is very arduous for this method to implement high-precision measurement for weak geomagnetic field. Moreover, the sensor needs several seconds ($1 \sim 3$ seconds) for pre-polarization before magnetic field measurement, which obviously increases power consumption, and the FID signal is exponentially decaying, in fact that effective frequency measurement time is only about 500 ms, therefore the continuous measurement could not be implemented. In allusion to the low sensitivity of the pre-polarization and continuous wave methods, the DNP effect could be utilized to solve this problem.

The achievement paths of the DNP effect include four distinct mechanisms[56]: the solid effect, which has limited experimental use; the Overhauser effect, which is the only one that has an appreciable effect for liquids; and the cross effect/thermal mixing, which is the predominant effect for contemporary solid-state and dissolution DNP. According to[21], the transverse relaxation time determines the interval available for the measurements of the frequency of the FID signal. In liquids, the transverse relaxation time may reach several seconds, whereas in solids, the transverse relaxation time is only milliseconds. Therefore, in this thesis, we focus on DNP in liquid free radicals and present only a summary of the Overhauser effect.

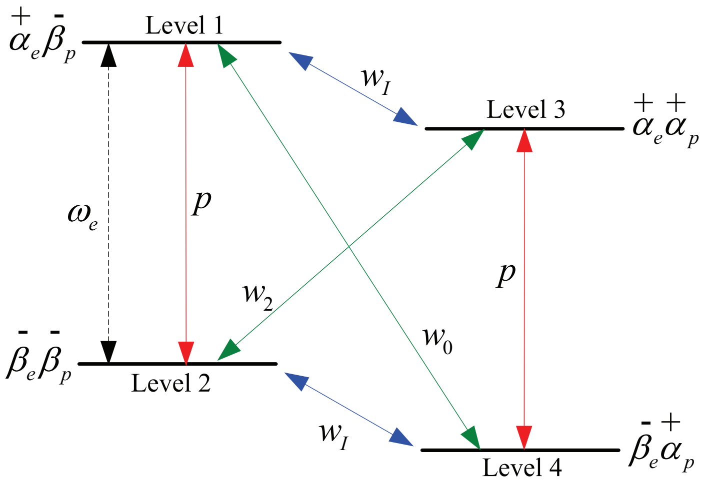

Figure 2-2: Four-level energy diagram for an electron spin S = 1/2 coupled to a ^{1}H proton spin I = 1/2.

As shown in Figure 2-2, the Overhauser effect for two spins (an electron spin S = 1/2 and ^{1}H proton spin I = 1/2) is typically described by a four-level diagram. Here, p is the electron spin relaxation rate, w_1 is the proton spin relaxation rate, w_2 is the double quantum relaxation rate and w_0 is the zero quantum relaxation rate. The basic theory of the Overhauser enhancement is as follows: an RF alternating field that angular frequency is ω_e saturates the electron spin relaxation, which creates a non-equilibrium population distribution of the electron spins. The electron-proton cross-relaxation then transfers the electron spin polarization from the electron spin to the proton spin. A non-equilibrium proton spin polarization is thereby achieved, implying that the proton magnetization is also enhanced[57–59]. According to the above analyses, the sample in the Overhauser sensor must simultaneously maintain a stable electron-proton spin system. Typically, an organic solvent rich in protons and a free radical are used to provide stable proton and electron spin systems, respectively

The enhancement of the proton polarization E is defined as[51]:

$$E = \frac{\langle I_z \rangle}{\langle I_0 \rangle} \approx 1 - \rho f s \frac{\gamma_e}{\gamma_p} \tag{2.4}$$

where $\langle I_z \rangle$ is the expectation value of the DNP, $\langle I_0 \rangle$ is its thermal equilibrium value[60], γ_e is the proton gyromagnetic ratio and γ_e is the electron gyromagnetic ratio. The saturation factor s is the degree of saturation of electron spin resonance (ESR), and varies from 0 to 1, depending on the power of the applied RF electromagnetic field[56]. In equation 2.4, ρ can be written as:

$$\rho = \frac{w_2 - w_0}{w_2 + 2w_1 + w_0} \tag{2.5}$$

and f is:

$$f = 1 - \frac{T_1}{T_1'} \tag{2.6}$$

where, T_1 is the longitudinal relaxation time of the solvent in the presence of the free radical, while T_1' is that in the absence of the free radical. The coupling factor ρ is understood as the ratio of the electron-proton spin cross-relaxation rate (w_2 - w_0) and the proton spin relaxation rate due to the electrons (w_2 + $2w_1$ + w_0)[58]. ρ expresses the efficiency of coupling between the electron and proton spins and ranges from - 1 (pure scalar coupling) to 0.5 (pure dipolar coupling)[61]. For free radicals dissolved in solution, the coupling of the electron spins to solvent protons can be either scalar or dipolar[62], and hence, ρ can be safely assumed to be one.

The leakage factor f relates to the electron's ability to relax the proton spin and can be expressed in terms of the longitudinal relaxation times T_1 and T_1' of the solvent in the presence and absence of the free radical, respectively. A leakage factor of one implies that all relaxations of the protons are caused by electrons, whereas a leakage factor of zero occurs when all relaxations of the protons are through other sources[56]. Ideally, s_{max} = 1 and f_{max} = 1 can be safely assumed; therefore, there is[61]:

$$E_{max} = 1 + \gamma_e / \gamma_p \approx 660 \tag{2.7}$$

In other words, the amplitude of the FID signal can in theory be increased by 660 times. However, the theoretical increase E_{max} cannot be achieved for several reasons, one being that other paths of relaxation are present.

To sum up, through the above theoretical analysis of the DNP effect, it could draw the following conclusions:

1) Compared with the pre-polarization and continuous wave methods, the DNP effect could greatly improve the proton polarization and macro proton magnetic moment, which provides a technology approach to improve the amplitude of the FID signal and overcome the disadvantages of the optically pumped sensor at the same time.

2) The prerequisite of the DNP effect is that the sensor must contain the sample which consists of electron spins and proton spins at the same time.

2.2 Larmor Precession Signal

The proton system in the sensor solution of proton precession magnetometer, whose magnetization component in the direction of the geomagnetic field is referred to as the longitudinal component of magnetization. When an external transverse component of magnetization M_x is applied, the initial phase of protons will be densely distributed in a certain direction. Once the external factor is removed, the protons' phase will tend to random distribution. In this process, the transverse component of magnetization M_x will undergo an exponential decay, which is called spin-spin relaxation. And the time it takes M_x to decay to the initial value of $1/e$ times is defined as the transverse relaxation time T_2 mentioned before, as shown in Figure 2-3.

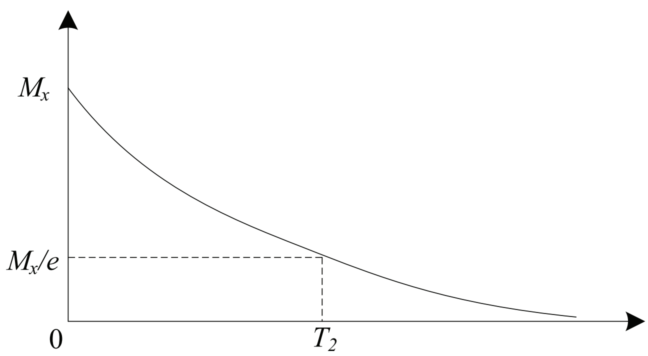

Figure 2-3: Curve of the transverse component of magnetization decay after polarization. Initially, the value of the transverse component of magnetization is M_x, and the time it takes it to decay to M_x/e is called the transverse relaxation time.

The amplitude of a FID signal generated by Larmor precession effect can be written as[21]:

$$\varepsilon(t) = \mu n A M \omega_0 \sin^2\theta \times e^{-t/T_2} \sin\omega_0 t \tag{2.8}$$

where μ is the permeability, M is the magnetic intensity of a proton and ω_0 is the angular frequency. A is the cross sectional area and n is the number of turns of the receiving coil, respectively. θ represents the angle between the axis of coil and the external magnetic field, and T_2 is the transverse relaxation time, which is usually less than 1 s. Figure 2-4 shows the FID signal waveform. It can be seen that the FID signal is a sinusoidal wave with an exponential decay of the magnitude and the frequency remains unchanged.

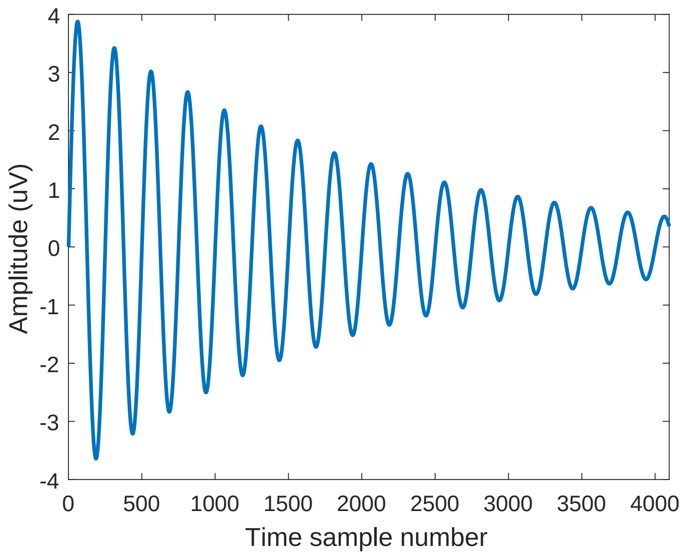

Figure 2-4: A sample FID signal.

According to equation 5.2, the relationship between the frequency f_0 and the magnetic field strength B_0 can be written as:

$$B_0 = 23.4874 \times f_0 \tag{2.9}$$

From equation 2.9, we can see that f_0 is proportional to B_0. Basically, the geomagnetic field is in the range from 20000 nT to 100000 nT and the frequency of FID signal is in the range from 850 Hz to 4300 Hz. In general, the FID signal is a sinusoidal wave at micro volt level with considerable noises, which introduce the challenge to measurement.

Chapter 3

Design of the Improved Overhauser Magnetometer

The basic framework of the improved Overhauser magnetometer is shown in Figure 3-1. The main functional blocks consist of sensor, polarization unit, signal conditioning system, frequency meter and controller. The sensor is consisted of high frequency

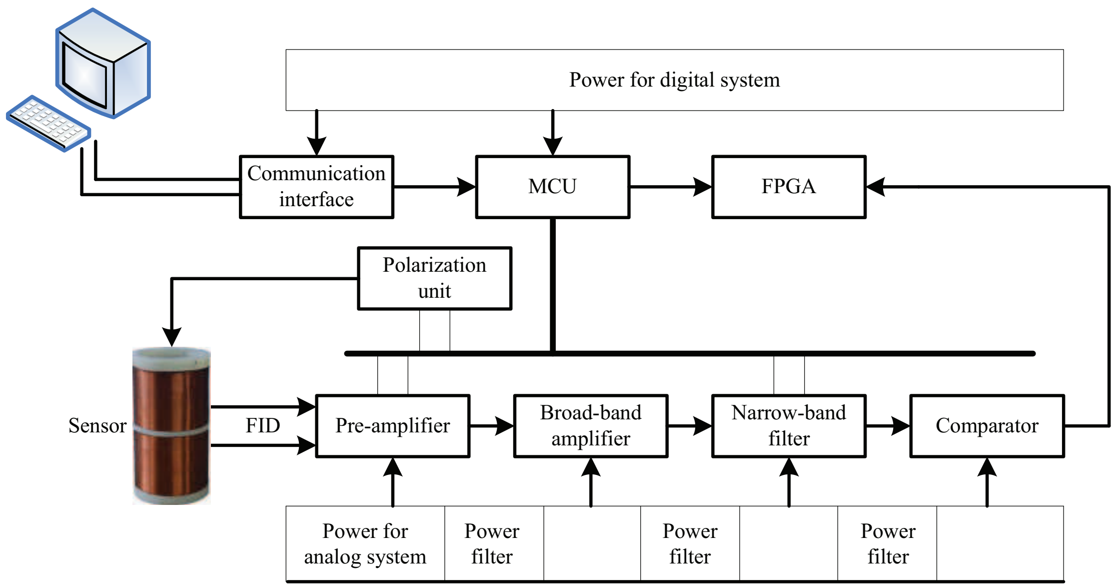

Figure 3-1: Scheme of the improved Overhauser magnetometer.

excitation coil, low frequency coil and free radical solution rich of hydrogen proton. The polarization unit, including RF and DC pulse generator, is used to polarize the free radical solution and produce transverse magnetic moment, respectively. The signal conditioning system is used to tune, amplify, filter and reshape the initial FID signal.

The field programmable gate array (FPGA) is used as frequency meter to measure the frequency, while the micro controller unit (MCU) works as the controller that controls the whole systems.

3.1 The Sensor

Generally, in a classical proton precession sensor, the proton polarization and the deflection into the plane of precession for the enhanced proton magnetization are achieved simultaneously[67]. By contrast, for the Overhauser sensor, the DNP effect can further enhance the proton polarization. Figure 3-2 shows the scheme of the Overhauser sensor based on the DNP effect is designed with a polarization coil, a sample (proton-rich organic solvent and free radical) and a pick-up coil.

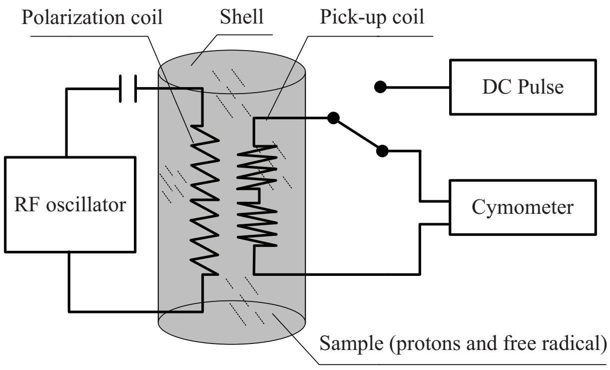

Figure 3-2: Scheme of the Overhauser geomagnetic sensor.

Figure 3-3 shows the enhancement and deflection of the proton magnetization in the sensor. As shown in Figure 3-3a and 3-3b, the sensor realizes the DNP effect using an alternating field generated by an RF oscillator and polarization coil, and pick-up coil, respectively; thereby, the proton magnetization $\boldsymbol{M}$ along the external magnetic field $\boldsymbol{B}_0$ is enhanced. Next, as shown in Figure 3-3c, after full proton polarization, the RF oscillator are both switched off, and a 90^o narrow pulse (the width is only dozens of milliseconds) is injected into the pick-up coil to generate a DC deflection field $\boldsymbol{H}$, which deflects the enhanced proton magnetization into the plane of precession and establishes a new proton magnetization $\boldsymbol{M}_p$. As shown in Figure 3-3d, after disconnecting the pulser, as with the classic proton precession sensor, $\boldsymbol{M}_p$ would rotate around the external magnetic field $\boldsymbol{B}_0$ and restore to the state as shown in Figure 3-3a. In the back haul, an

FID signal is induced in the pick-up coil, whose mathematical expression is given in equation 2.8.

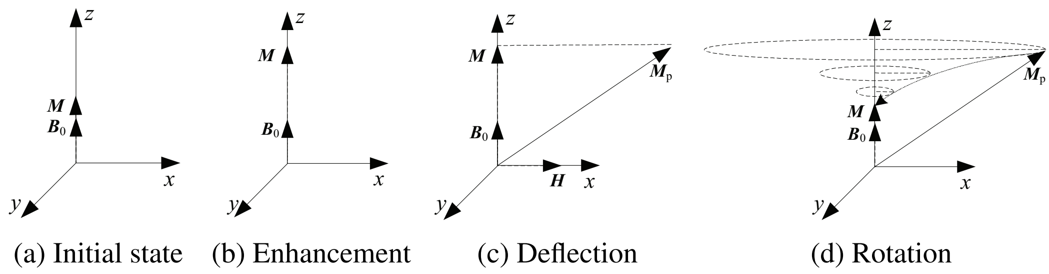

Figure 3-3: Enhancement and deflection of proton magnetization.

3.1.1 Free Radical Solution

The free radical usually contains unpaired electrons, and the magnetic moments of spin electrons do not completely cancel, hence it is paramagnetic. In consequence, the free radical usually acts as the main carrier for free electron, wherein the nitroxide free radical is commonly used due to its stable chemical property. The nitroxide free radical could be divided into four categories[69]: (1) piperidine nitroxides, (2) pyrrolidine nitroxides, (3) oxazolidine nitroxides, (4) proxyl nitroxides, where (1) $\sim$ (3) above are widely used. The chemical constitution of the representative nitroxide free radicals are shown in Figure 3-4, where the right half is 3-Carboxy-PROXYL, and the left half is the chemical constitution of 4-Oxo-TEMPO. Considering the stability requirement for the geomagnetic sensor, most of Overhauser magnetometers' sensors select the 4-Oxo-TEMPO (piperidine nitroxide) as the free radical currently.

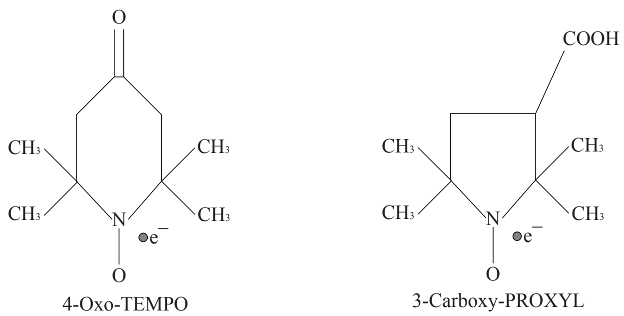

Figure 3-4: Chemical constitution of representative nitroxide free radicals.

Essentially, the of the polarization of free radical solution is to enable the nuclear to be polarized by exciting the unpaired electrons. Accordingly the sensor realizes the double resonance of unpaired electron spin system in 4-Oxo-TEMPO and the proton spin system in dimethyl ether. According to the principle of electron paramagnetic resonance (EPR), the relationship between the resonance frequency of free electron paramagnetic and external magnetic field can be written as:

$$f_p \approx 28.025 \cdot B \tag{3.1}$$

where f_p is the polarization frequency (unit: GHz), and B is magnetic field strength (unit: T). The free radical molecules can be seen as an electronic system, and the organic solvent itself contains a large number of protons, which can be seen as a proton system. Therefore, there are two systems include electron and proton in the solution, which can meet the double resonance condition at the same time. If one puts the solution in a stable magnetic field, and adopts a radio frequency (RF) electromagnetic wave directly irradiates it, when the frequency meets the EPR condition of free radical unpaired electrons, the double resonance is occurred, which called dynamic nuclear polarization (DNP).

The unpaired electrons of 4-Oxo-TEMPO are in the nuclear magnetic field that is produced by nitrogen-atoms, whose value is about 2.1 mT. According to equation 3.1, we can derive that the resonance of unpaired electrons is about 60 MHz. In other words, by utilizing a 60 MHz alternating field, the free radical solution can realize the double resonance. For the free electrons, without the nitrogen nuclear field, the frequency of RF field must change with geomagnetic field. As the magnetic field acting on the unpaired electrons in 4-Oxo-TEMPO is about 100 times more than that acting on the free electrons, which could greatly increase the DNP factor. Theoretically, the DNP factor of the free electron is 330, by striking contrast, that of the unpaired electron in 4-Oxo-TEMPO could reach up to 10000[57].

The polarization of unpaired electrons is essentially the transition of energy level[69]. Figure 3-5 shows the energy level diagram of 4-Oxo-TEMPO, from which we can observe that, without the external magnetic field, the energy splitting of the unpaired electrons will also happen, namely zero-field splitting, while when the external magnetic field is applied, the hyperfine energy splitting will happen. There are four energy levels: $|1\rangle$, $|2\rangle$, $|3\rangle$, and $|4\rangle$. When an RF electromagnetic wave irradiates the solution, if the unpaired electrons transit from $|1\rangle$ to $|2\rangle$, the positive DNP will happen, and the value

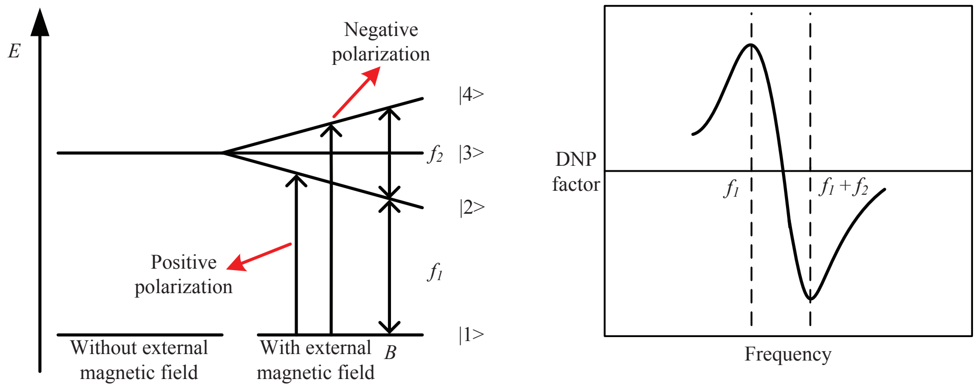

(a) Energy level (b) DNP factor

Figure 3-5: Diagram of energy level transition.

of DNP factor is positive. If they transit from $|1\rangle$ to $|4\rangle$, the negative DNP will happen, and the value of DNP factor is negative. Therefore, DNF will be generated under the condition that, if a constant magnetic field is acting on the free radical solution, as the B being the magnetic field strength in Figure 3-5a, and an RF electromagnetic wave with enough power and variable frequency irradiates the solution. When the frequency value is f_1, the solution generates positive DNP, while if continue increasing the frequency value to $f_1 + f_2$, the negative DNP will happen, as is shown in Figure 3-5b. Through differential structure, the signal superposition can be realized, and the SNR is increased, thereby improving the measurement accuracy.

3.1.2 Design of Anti-Interference

The original electromotive force of Larmor precession signal received by the sensor is only a few microvolts[46]. Hence, the sensor can easily disturbed by a variety of noises when measured in the outdoor, such as external electromagnetic interference (EMI) sources and man-made noise. Indeed, the signal can be swamped seriously. Therefore, the anti-interference capability is a critically parameter for the sensor to function.

A differential dual-coil structure[24,25] consisting of two series-opposing coils is applied as shown in Figure 3-6a, which can eliminate the external interference, thereby enhance the common-mode rejection ratio of the sensor effectively. Basically, the external EMI can be assumed to be uniformly distributed as the size of sensor is small. According to the principle of Faraday and Lenz, the electromotive forces of V_1 and V_2 induced in the two coils are equal while the directions are opposite. Hence, the induced

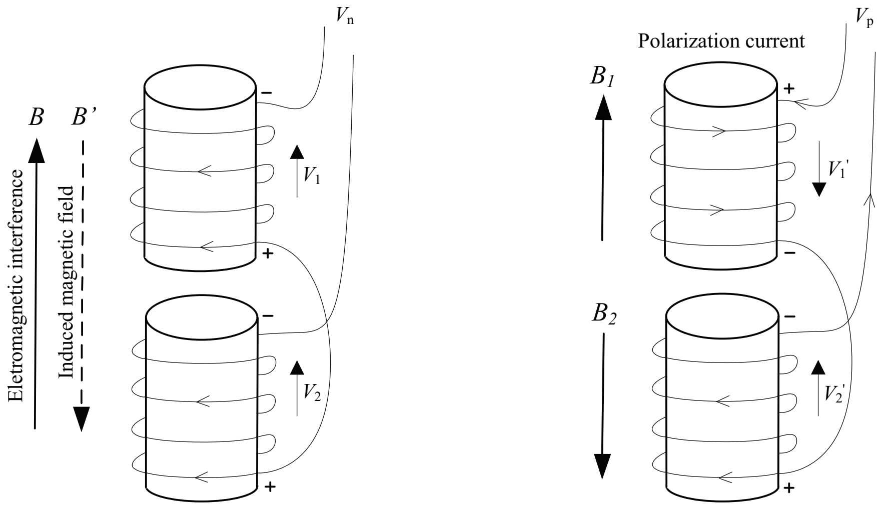

(a) Interferences counteraction.

(b) Receiving FID signal.

Figure 3-6: The anti-interference structure of the differential dual-coil.

total electromotive force V_n of the external EMI is canceled out as $V_n = V_1 + (-V_2) \approx 0$. According to the work flow of the Overhauser gradiometer mentioned before, during the polarization, there is a DC current through into the two coils. Meanwhile, two opposing induced magnetic fields B_1 and B_2 are generated. Due to the series-opposing structure, the directions of the two induced electromotive forces $V_1{}'$ and $V_2{}'$ are the same and their values are the same. Therefore, the total electromotive force V_p of the Larmor precession signal is $V_p = V_1' + V_2' \approx 2V_1'$. Based on these, the Larmor precession signal received by the entire sensor can be written as:

$$V = V_n + V_p \approx V_p \approx 2V_1' \tag{3.2}$$

Consequently, this differential structure cannot only suppress the external EMI that implies enhance the anti-interference capability of the sensor, but also improve the original electromotive force of Larmor precession signal.

To sum up, the completed composition of the sensor based on the structure of differential dual-coil is shown in Figure 3-7. The two series-opposing receiving coils were wound around the two grooves of the coil skeleton, and the inductance of was about 34 mH. The resonant cavity composited by multitude silver foils was inserted in the cavity of the sensor to induce the Larmor precession signal effectively. The dewar that full of sample wrapped by this resonant cavity were installed in the skeleton of receiving dual-coil together. As the energy of the resonant cavity was mainly concentrated

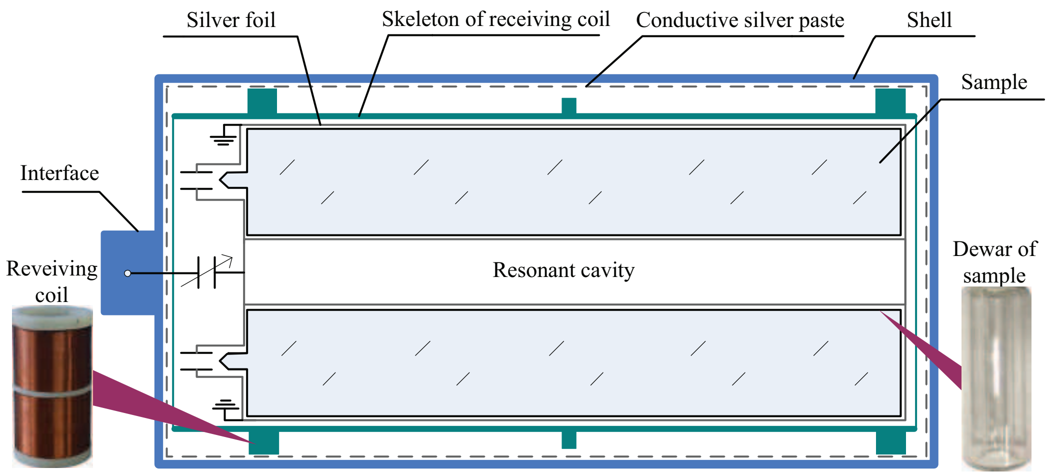

Figure 3-7: Composition of the sensor.

in the cavity, the silver foil was directly installed on the surface of the dewar to fully polarize the free radical. The conductive silver paste was used for further enhancing the shielding effectiveness[67]. In addition, three adjustable capacitors were placed at the interface of the resonant cavity to adjust the resonance frequency. Through the interface, the RF and DC signal from the instrument were applied to the resonant cavity and the receiving coil, respectively. Both of the polarization signals could be split automatically by an LC filter. Further information about the sensor production can be found in literature[51].

3.1.3 Design of Testing System for Sensor Parameters

Basically, the measurement accuracy of Overhauser magnetometer is determined by the quality of Larmor precession signal. Moreover, the signal's quality is determined by the polarization frequency accuracy of the free radical solution. As mentioned before, Overhauser magnetometer's sensor mostly uses the nitrogen oxygen free radical compound solution (refer to 4-Oxo-TEMPO in this thesis), while different solvents or concentrations may lead to different polarization frequencies and bandwidths, and the polarization degree is correlated to the polarization power and time. Only when free radical solution is fully polarized, the Larmor precession signal with higher SNR can be obtained[70]. Therefore, measuring the polarization frequency of the free radical solution accurately is very important, as well as the quality factor of the sensor. Generally, according to the component and composition ratio of free radical solution, some researchers adopted large instrument and equipment, measuring the polarization frequency based on physical [12,71] and chemical means [10,72]. The operations are relatively complex, and there are relatively few papers researching on the theoretical design and simulation of sensor and the composition ratio of free radical solution. Tan proposed an Overhauser magnetometer excitation and receiving system, which can measure the polarization frequency accurately and conveniently [41]. However, the measurement resolution and bandwidth cannot meet the nowadays' increasing needs of accuracy.

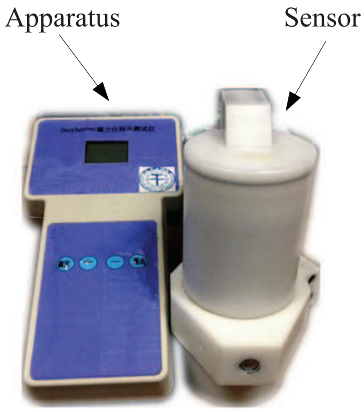

Figure 3-8: The proposed test apparatus.

Aimed to solve these problems, according to the principle of free radical solution polarization, a test apparatus for measuring the critical parameters (e.g., polarization frequency and quality factor) of Overhauser magnetometer's sensor was developed as shown in Figure 3-8. This apparatus can generate a stable Radio Frequency (RF) signal in the range of 50 MHz $\sim$ 100 MHz, providing adequate test bandwidth for free radical solution with different components, with the resolution being 1 Hz. Moreover, the Analog to Digital Converter (ADC) synchronous acquisition technology and the normalized processing algorithm are adopted, so that the measured data can be saved in synchronously, and uploaded to personal computer (PC) for subsequent analysis.

Overall Hardware Structure

The hardware structure of the proposed apparatus is shown in Figure 3-9. The apparatus consists of master control system, controllable RF signal source, weak signal amplification circuit, and high frequency peak detector. There are two operating modes: frequency measurement and assistant measurement, which are switched by relays "K" and "S". The frequency measurement mode is used to measure polarization frequency of different free radical solutions, while the assistant measurement mode is used to identify the measurement results.

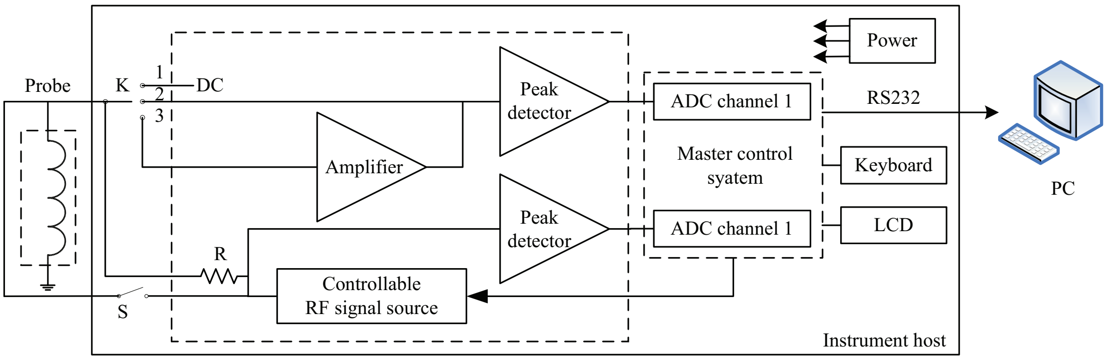

Figure 3-9: Hardware structure of the proposed test apparatus.

Controllable RF Signal Source

The apparatus has two operating modes: frequency measurement mode and assistant measurement mode. When it works in frequency measurement mode, a swept RF signal is adopted to the sensor. However, because of the electrical characteristics, as the frequency increasing, the amplitude would be decreased. In order to ensure the effectiveness of the polarization signal in high frequency band, the signal need to be amplified. In assistant measurement mode, based on the test result of the frequency measurement mode, a swept RF signal need to be adopted to polarize the sensor, to make the free radical solution occur DNP. As a result, the signal need to be power amplified. Based on this, we designed a controllable RF signal system, as is shown in Figure 3-10.

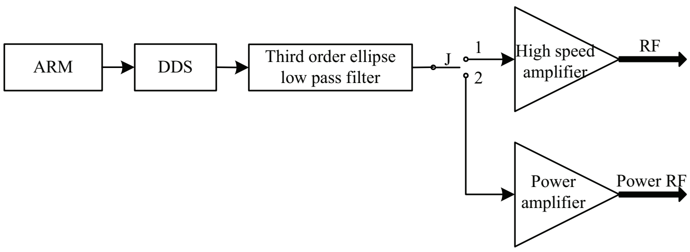

Figure 3-10: Controllable RF signal source.

The direct digital synthesizer (DDS) can generate stable sine wave signal in frequency range from 50 MHz to 100 MHz, and the step frequency is adjustable, which can meet the measuring requirement of Overhauser magnetometer's sensor (generally, the polarization frequency is around 60 MHz). Because the signal output of DDS contains higher harmonics, a third order ellipse low pass filter is adopted[43,73], and the amplitude of filtered signal is about 0.5 Vpp. The relay "J" is used to switch two measurement modes. Due to the high frequency, an ordinary amplifier cannot meet the frequency requirement. A high speed current operational amplifier is adopted to solve this problem. Through test, the amplitude of amplified signal RF is about 2 Vpp. The power amplifier adopts the RF NMOS tube. Through test, the maximum output power of the amplified signal power RF is about 2 W, which meets the effective polarization power requirement of free radical solution in sensor.

In polarization frequency measurement mode, the working process of the apparatus is as follows:

Step 1: Switch "K" in Figure 3-9 to "2", disconnect "S", and switch "J" in Figure 3-10 to "1".

Step 2: Control the signal source to generate RF signal, the frequency range is $f_1 \sim f_2$, and step frequency is Δf.

Step 3: Synchronous sampling two channels' signal amplitude of peak detection, which respectively uses the sensor and the 50 Ω resistor ("R" in Figure 3-9) as load. Moreover, a RC low band filter is adopted at the output of peak detector, which can further suppress the noise and improve the effectiveness of data.

Step 4: Set the frequency value of RF signal as $f_1 + \Delta f$, and repeat the *Step 1, 2, 3*. The working sequence of this mode is shown in Figure 3-11.

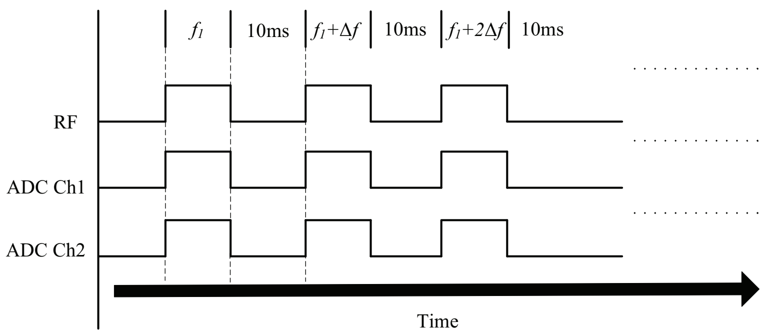

Figure 3-11: Working sequence of polarization frequency measurement mode.

In the assistant measurement mode, the working process of the apparatus are as follows:

Step 1: Switch "K" in Figure 3-9 to "1", connect "S", and switch "J" in Figure 3-10 to "2".

Step 2: Control the RF signal source generate high frequency power signal to polarize the sensor, according to the polarization frequency test result f_0, set the frequency range as (f_0-2MHz) $\sim$ (f_0+2MHz), and step frequency is Δf.

Step 3: Switch off the power RF signal, adopt a DC narrow pulse to the sensor.

Step 4: Switch "K" in Figure 3-9 to "3", switch off DC, then the FID signal will generate in the receiving coil of sensor. Adopt ADC sample the amplitude of signal, which has been amplified and peak detected.

Step 5: Set the frequency value of RF power signal as f_0 - 2MHz + Δf, and repeat the *Step 1, 2, 3, 4*. The working sequence of this mode is shown in Figure 3-12.

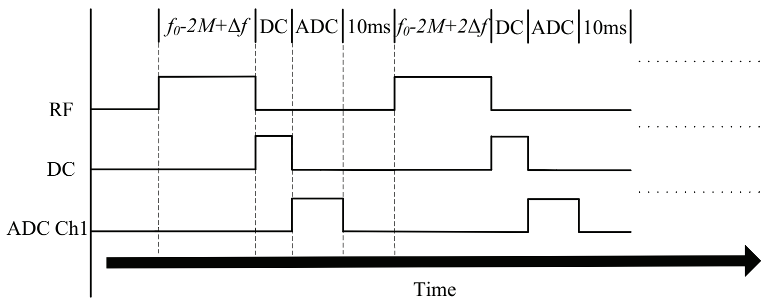

Figure 3-12: Working sequence of assistant measurement mode.

Normalization Processing

Due to the electrical properties of electronic device, the amplitude-frequency characteristic curve is not completely flat in the range of 50 MHz $\sim$ 100 MHz[41]. Aiming at solving this problem, we add an acquisition channel as reference. The normalized results can be obtained by calculating the ratio of two channels' data, which reflect the sensor's parameters effectively. Therefore, when the apparatus is in operation, sampling two channels' signal synchronously. The first channel adopts 50 Ω resistor as load and the measurement data called "data1", while the second channel adopts sensor as load and the measurement data called "data2". Then, "data2" is divided by "data1" to get the normalized data. In order to test and verify the feasibility of this method, we input an RF signal directly to the apparatus's test interface ("K" and GND in Figure 3-9). The sensor was replaced by using a resistor which has the similar impedance (about 50 Ω) as sensor. This means two test channels are both using pure resistance as load. The following steps of polarization frequency measurement mode were tested, and the results are shown in Figure 3-13.

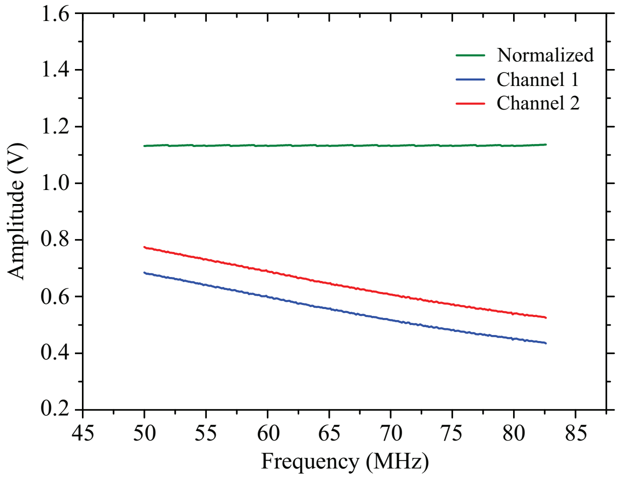

Figure 3-13: The normalized processing results.

From Figure 3-13, we observe that if the frequency of RF signal increases, the peak value will decrease, and this has a relationship with the load and the electrical properties of peak detector, which cannot be completely consistent. However, according to the normalized results, the obtained curve is approximately linear and smooth, which effectively solved the problem that apparatus's amplitude-frequency characteristic curve cannot be completely flat in 50 MHz $\sim$ 100 MHz.

Sensor Parametric Test

According to Figure 3-7, the equivalent circuit of resonant cavity can be expressed as shown in Figure 3-14.

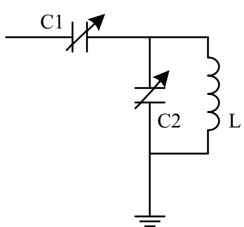

Figure 3-14: Equivalent circuit.

Figure 3-15a shows the simulation results of the equivalent circuit. We observe that the resonance frequency and the quality factor can be changed by adjusting C1 and C2. Based on the simulation results, we developed a circuit as is shown in Figure 3-14, set the proposed apparatus work in frequency measurement mode, sweep frequency range is 5 MHz $\sim$ 100 MHz and step frequency is 0.5 MHz. Connect the test interface to the input and GND of circuit, respectively, test following the steps as shown in Figure 3-11, and the results are shown in Figure 3-15b. We observe that the resonance frequency is about 55 MHZ and 65 MHZ under different parameter conditions, and the curve's overall trend is almost the same as simulation results. The difference between the bandwidth and the gain is caused by the electric parameters of devices themselves. Therefore, when designing a resonant cavity, in order to make sure that the resonance frequency is equal to the polarization frequency of the sample, the adjustable capacitors need to be fine-tuned repeatedly. This apparatus is then used to measure resonance frequency in every condition, and this is another significance why we develop this test apparatus.

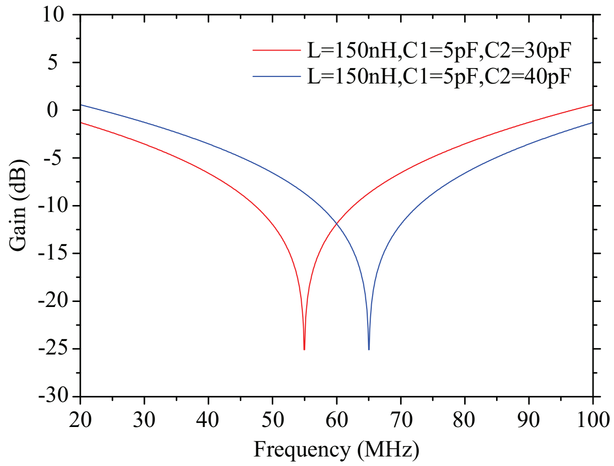

(a) Simulation.

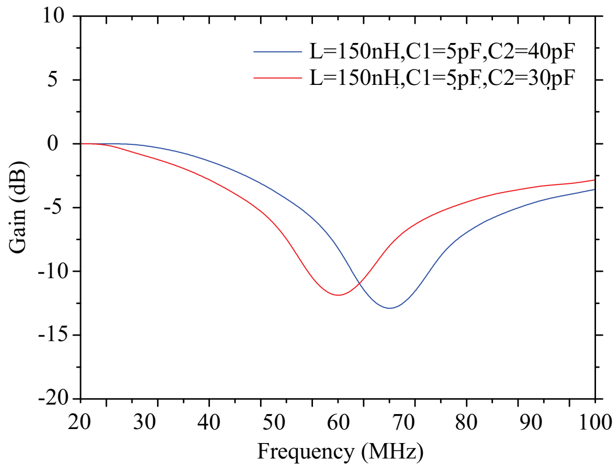

(b) Practical.

Figure 3-15: Simulation and actual test results for equivalent circuit.

Through the simulation experiments and theoretical analyses above, we adopted a commercial Overhauser magnetometer's sensor (polarization frequency: 60.7 MHz) as test object. In order to ensure the effectiveness of test results, the sensor's orientation is remained unchanged, and the polarization power and time are also constant. Figure 3-16a shows the test results of different adjustable capacitors in the sensor. We can observe that the polarization frequency measured by the proposed apparatus is about 60.7 MHz, which is consistent with the sensor's own polarization frequency. If the value of the adjustable capacitor changes, the resonance frequency and quality factor will be changed. Therefore, if it is not well-adjusted, the polarizability of free radical solution will not be complete, thereby the quality of FID signal generated in the receiving coil is poor. Therefore, when designing the resonant cavity of a sensor, the apparatus should be adopted to repeatedly measure whether the resonance frequency is equal to the polarization frequency of free radical solution.

To further verify the experimental results above, we switched the apparatus to assistant measurement mode. The polarization frequency range is 59 MHz $\sim$ 62 MHz, and the step frequency is 0.02 MHz. The results are shown in Figure 3-16b. The free radical solution in the sensor can be fully polarized by an RF power signal, in which frequency is about 60.7 MHz. In other words, the amplitude of FID signal is the maximum at this moment. The bandwidth is about 0.2 MHz, which is consistent with the result of Figure 3-16a. Therefore, using this apparatus can measure the polarization frequency and bandwidth accurately, so the validity and the necessity of this apparatus is verified.

Figure 3-17a shows the relationship between the output FID signal peak value and the polarization time (polarization frequency: 60.7 MHz). We observe that 1) when the peak value of RF signal is constant, if the polarization time increases, the output FID signal value will increase exponentially. However, if the polarization time is more than 4 s, the peak value has no significant increase; 2) when the polarization time is unchanged, if the polarization power (the RF signal peak value) increases, the output FID signal value will increase. Thus, it can be seen that this apparatus can also be adopted in the research for the relationship between the polarization time and power.

Figure 3-17b shows the relationship between the output FID signal peak value and the polarization power (polarization time: 2 s). We can observe that when the polariza-

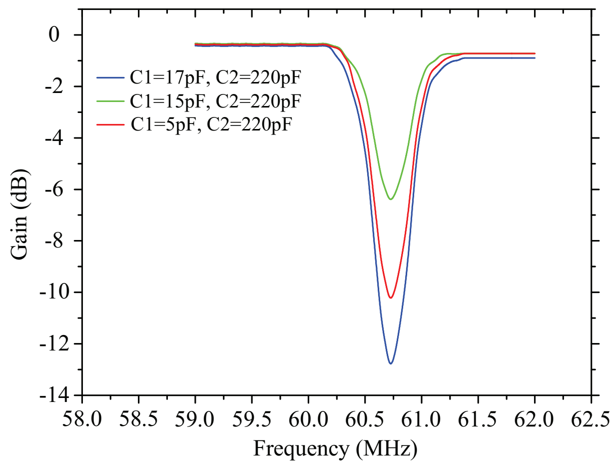

(a) Test with different parameters.

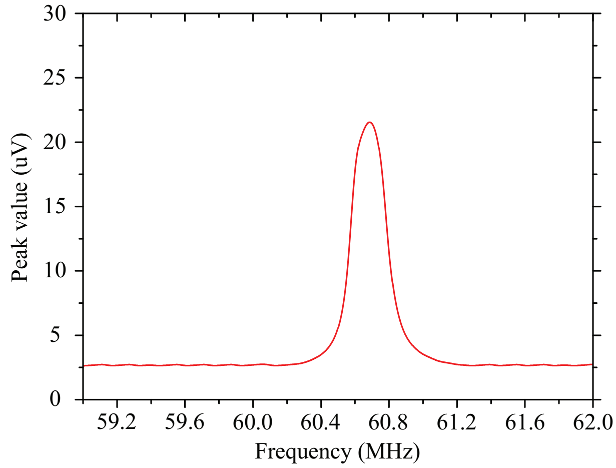

(b) Peak value vs. polarization frequency.

Figure 3-16: The resonant cavity test results and its identification.

tion time is constant, if the polarization power increases, the peak value of output FID signal will increase exponentially. However, if the polarization power is more than 1.5 W, the peak value has no significant increase. This indicates that the output FID signal's quality is related to the polarization power, which provides reference for designing Overhauser magnetometer.

In summary, the amplitude of output FID signal is directly depending on the polarization power: the greater the power, the greater the amplitude. When the power increases to a certain degree, the amplitude will be close to saturation. This is due to the physical properties of free radical solution in the sensor. According to the mentioned above, when an RF signal with special frequency is adopted to free radical solution, the electron spin resonance (ESR) will happen, thus promotes proton spin polarization, and causes energy level transition. The amplitude of FID signal fundamentally depends on

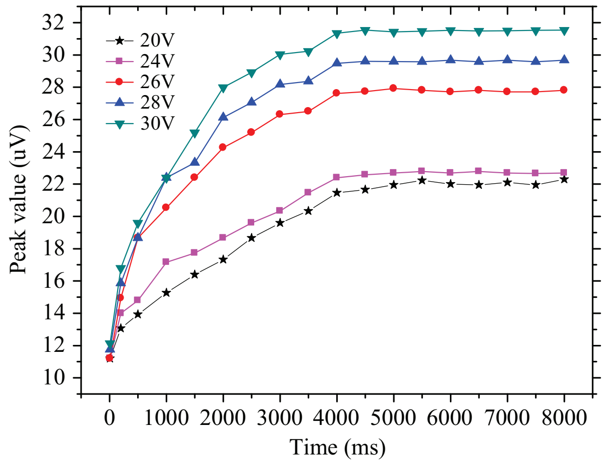

(a) Output FID peak value vs. time.

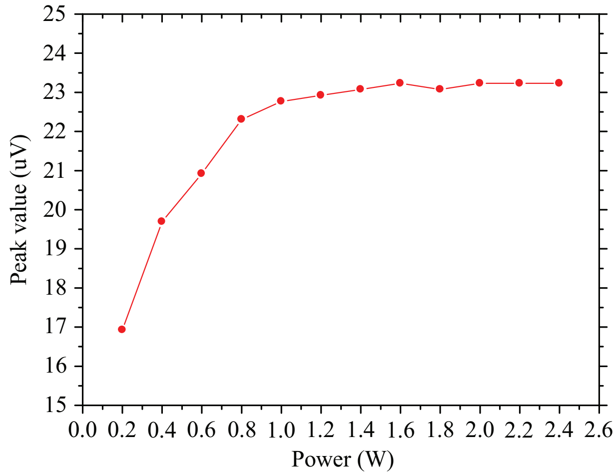

(b) Output FID peak value vs. power.

Figure 3-17: Sensing signal characteristics test.

the number of protons that generate energy level transition. The more number of activated protons, the greater the amplitude of FID signal. Due to the fact that the volume of free radical solution in the tested sensor is constant, the number of protons is constant. Therefore, when the polarization power increases, the number of activated protons will increase, thereby increasing the amplitude of FID signal. When the polarization power is high enough, all the protons have been activated, then the amplitude of FID signal remains unchanged.

3.2 The Signal Acquisition and Processing System

The signal acquisition and processing system consists of two parts: digital and analog. The digital module mainly including an micro controller unit (MCU) and an field programmable gate array (FPGA), which can be used to control relays, measure frequency, communicate with associated peripherals and transmit data. The analog module consists of polarization unit and signal conditioning unit. Figure 3-18 shows the overall framework of the signal polarization and acquisition system.

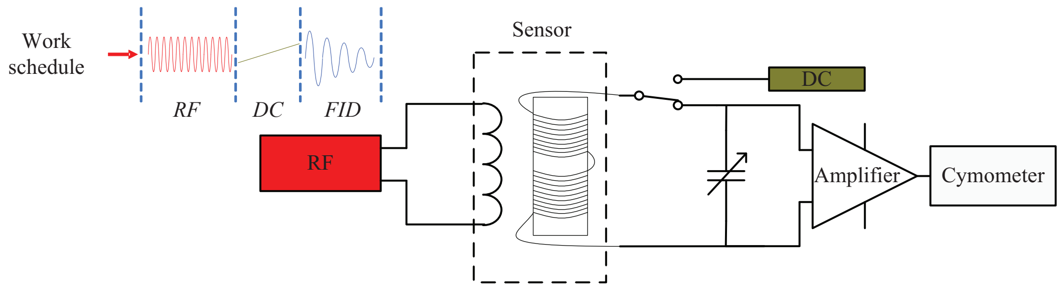

Figure 3-18: Framework of the polarization and signal acquisition system.

3.2.1 Polarization Unit

According to the principle of DNP, the RF polarization signal is the critical factor that determines the energy transformation degree from unpaired electrons to protons. The Miller oscillator and three-point capacitance oscillator circuits are commonly used in current Overhauser magnetometers[46,74] as the RF signal generator. Both oscillators depend on the properties of inductor. However, due to the instrument works for a long time, the ambient temperature of the inductor will increases, which leads to the value shift and the decrease of stability. To solve this, a kind of high-precision, high stability and programmable silicon oscillator called LTC6605 was adopted in this gradiometer. It requires only a single resistor to set the output frequency from 17MHz to 170MHz with a typical frequency error of 0.5 % or less[75], while the polarization frequency of the free radical solution adopted in the sensor is about 60.7 MHz. Meanwhile, as the RF signal will interfere the entire system, which leads to the error of magnetic field measurement. A shielding shell was used to suppress the interference. Figure 3-19 shows the practical RF polarization signal. The Vpp can reach up to 60 V and has the characteristic of a distortion degree of the signal is small, the frequency extension is stable etc.

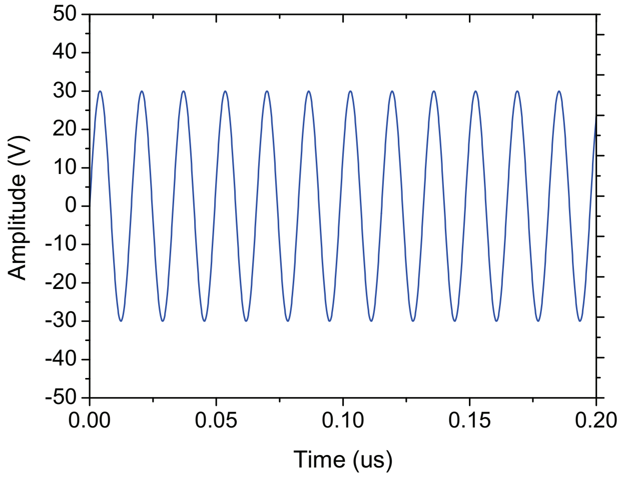

Figure 3-19: Practical RF polarization signal.

3.2.2 Signal Conditioning Unit

In general, the original FID signal is very weak, the particular voltage is about a few microvolts[76], and the signal is so small that it can easily be disturbed by noise. According to the coil parameters of the sensor and the quality factor of the resonance circuit, after running some tests, in the range of the geomagnetic field, the actual voltage value of the resonant FID signal is $2 \sim 30\ \mu\mathrm{V}$[77]. In order to obtain a higher SNR of the FID signal to measure the frequency of signal accurately, the gain of amplifier should reach several hundred thousand, even more one million[78]. However, the SNR of high gain amplifier is sensitive, hence the signal need apply the multilevel filter which can decrease the noise.

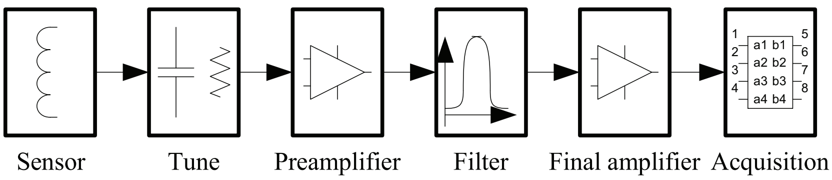

Figure 3-20: The structure of signal conditioning system.

Figure 3-20 shows the structure of signal conditioning system, which consists of resonant circuit, amplifier, narrow band filter and comparator. In order to get a higher SNR of original signal, a resonant circuit is used before the amplifier. Since the total noise level of the system mainly depends on the noise figure of the preamplifier. Then a N-channel JFET with noise figure less than 0.5 dB is used as the preamplifier. Meanwhile, metal film resistors are primarily used throughout the circuit to reduce the additional of Johnson noise[48]. The narrow-band filter is an important part of the signal conditioning circuit since it decrease the system bandwidth and improve the output SNR. Part of the band-pass is defined by the resonant circuit at the front. However, the noise of amplifiers is added subsequent to signal conditioning circuit. Hence, it is necessary to have an additional narrow-band filter later. The final amplifier is used to further amplify the filtered signal to make sure that its amplitude can reach up to the threshold of the comparator. In addition, a shielding shell is adopted to the tuner and the preamplifier to further eliminate the external electromagnetic interference. Thereby improving the SNR of the obtained FID signal. In the acquisition procedure, the amplified FID signal is shaped into square and measured by a cymometer. Overall, the role of the multilevel amplifier is to amplify the weak larmor precession signal, and the amplification factor is in the scope of 99 dB $\sim$ 113 dB as shown in Figure 3-21. The narrow-band filter attenuates the harmonics interferences effectively, and the SNR of FID signal is increased. The hysteresis compactor which threshold value is changed with the input signal is adopted, transforming the input sine wave signal into the square signal.

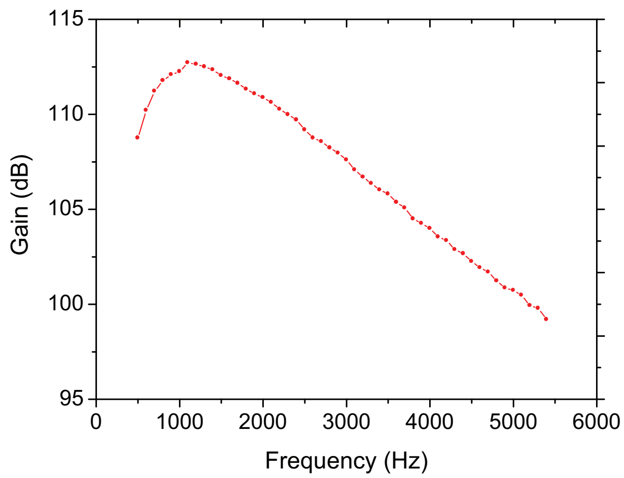

Figure 3-21: The amplitude-frequency response property of the system.

3.2.3 Theoretical Calculation of the Sensor and Preamplifier Noise

The noise degree of the system directly affects the frequency measurement accuracy. Furthermore, the total noise level mainly depends on the noise figure of the preamplifier. In this case, the noise refers to the noise floor of the system, the background noise and man-made noise are not taken into account. Due to the sensor and preamplifier are the critical source of the noise, we set up the equivalent circuit with various noise sources of the sensor and the preamplifier as shown in Figure 3-22.

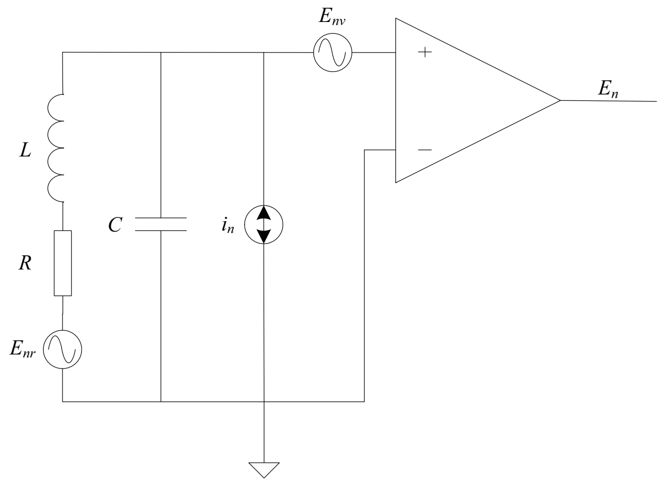

Figure 3-22: The noise model of the sensor and amplifier.

Basiclly, the output signal of the sensor through the amplifier via the shielded cable, which can generate the induced noise of the inductance and that of the shielded cable. Due to both of them are dependent on the external electromagnetic environment, they cannot be calculated theoretical. However, we can adopt several measures to make the induced noise as small as possible, such as the electromagnetic shielding of the sensor, the single-point grounding of the signal line, etc. Regardless of the induced noise, the noise of the output signal of a sensor and circuits can be quantitatively calculated. There are three main noise sources: the thermal noise E_{nr} generated by the inductance resistance R of the sensor, current noise E_{ni} generated by the input current i_n of the amplifier through the inductance resistance R of the sensor, and voltage noise E_{nv} generated by the amplifier[79]. Therefore, the total voltage noise E_n is:

$$E_n = \sqrt{E_{nr}^2 + E_{ni}^2 + E_{nv}^2} \tag{3.3}$$

In the sensor circuit, the thermal noise E_{nr} of the inductance resistance R can be written as:

$$E_{nr} = \sqrt{4KTR} \tag{3.4}$$

where, K is the Boltzmann constant and T is the absolute temperature. If the closed-loop gain of the preamplifier is G, the contribution of thermal noise E_{nr} at the preamplifier output is:

$$E_{nro} = E_{nr} \frac{1/j\omega C}{j\omega L + R + 1/j\omega C} \cdot G \tag{3.5}$$

where, C is the tuning capacitor. The contribution of voltage noise E_{nv} at the preamplifier output is:

$$E_{nvo} = E_{nv} \cdot G \tag{3.6}$$

and that of current noise E_{ni} is:

$$E_{nio} = i_n[(j\omega L + R)||(1/j\omega C)] \cdot G \tag{3.7}$$

thus, equation 3.5 can be simplified as:

$$\begin{aligned} E_{nro}^2 &= E_{nr}^2 \left| \frac{1/j\omega C}{j\omega L + R + 1/j\omega C} \right|^2 \cdot G^2 \\ &= E_{nr}^2 \frac{1}{(1-\omega^2 LC)^2 + \omega^2 C^2 R^2} \cdot G^2 \end{aligned} \tag{3.8}$$

and equation 3.7 can be simplified as:

$$\begin{aligned} E_{nio}^2 &= i_n^2 |[(j\omega L + R)||(1/j\omega C)]|^2 \cdot G^2 \\ &= i_n^2 \frac{R^2 + \omega^2 L^2}{(1-\omega^2 LC)^2 + \omega^2 C^2 R^2} \cdot G^2 \end{aligned} \tag{3.9}$$

Therefore, equation 3.3 can be written as:

$$\begin{aligned} E_n^2 &= E_{nr}^2 + E_{ni}^2 + E_{nv}^2 \\ &= \frac{E_{nr}^2 + E_{nv}^2[(1-\omega^2 LC)^2 + \omega^2 C^2 R^2] + i_n^2(R^2 + \omega^2 L^2)}{(1-\omega^2 LC)^2 + \omega^2 C^2 R^2} \cdot G^2 \end{aligned} \tag{3.10}$$

where, $\omega = 1/(LC)^{1/2}$. According to the parameters of the sensor (L = 34 mH, R = 19 Ω), we set the frequency as 2100 Hz, then C can be calculated as 167 nF refer to equation 4.27. For convenience to analysis the noise characteristics of the sensor, the total parameters calculated in this thesis are shown in Table 3.1.

The representation of the noise level at the preamplifier output allows a direct comparison of contribution of each noise source. We calculate each noise contribution at preamplifier output and the overall noise is also obtained as shown in Figure 3-23.

As shown in Figure 3-23, the contribution of the preamplifier voltage noise E_{nv} is

Table 3.1: The total parameters of the sensor and preamplifier.

Inductance of detection coil L (mH)	34
Resistance of detection coil r (Ω)	19
Gain of preamplifier G	50
Tuning capacitor C (nF)	167
Resonance frequency of circuit f_0 (Hz)	2100
Voltage noise produced by preamplifier E_{nv} ($\mathrm{nV} \cdot \mathrm{Hz}^{-1/2}$)	1.4
Current noise produced by preamplifier i_n ($\mathrm{pA} \cdot \mathrm{Hz}^{-1/2}$)	0.2
Boltzmann constant K (J/T)	1.38×10^{-23}
Kelvin Temperature T (K)	300

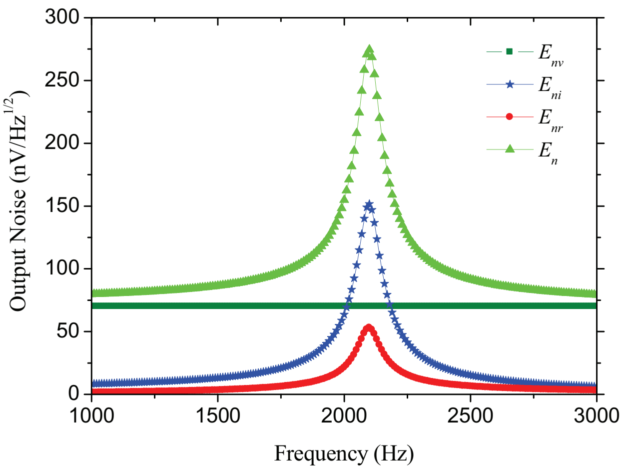

Figure 3-23: Calculated result of preamplifier output noise.

a considerable part at the overall noise frequency range. The contribution of the detection coil thermal noise E_{nr} will acquire maximum value at the resonant frequency and decrease progressively away from the resonant frequency. Impact of the preamplifier current noise i_n can be neglected for low current noise level of JFET. Although the matched resistance is much large than the coil resistance, it has little impact on the overall noise. In general, the contribution of the detection coil thermal noise E_{nr} is main part around the resonant frequency and the preamplifier voltage noise E_{nv} is the main contributor when away from resonant frequency. The overall preamplifier output noise E_n is mainly decided by the preamplifier voltage noise E_{nv} and the detection coil thermal noise E_{nr}. The results indicate that the noise power spectral density of E_n shows a band-limited white noise characteristic. The maximum value of the noise power spectral density appears at the resonant frequency.

Chapter 4

Improved Analog & Digital Signal Processing Algorithm

The first objective of this section is to establish different types of noise models for the FID signal, which are further applied to evaluate the influence of noise on the FID signal quality. Simulation is first conducted to identify how the measurement accuracy effected by different SNRs. Moreover, the error for the frequency measurement of the FID signal has been analyzed and the measurement accuracy for the SNR of the amplified FID signal is determined. The second objective is to develop a multi-channel frequency measurement algorithm to improve the accuracy of the measured magnetic fields in a broader dynamic range and in a noisier environment. The third objective is to propose a a secondary tuning algorithm based on singular value decomposition (SVD) and shot time Fourier transform (STFT), which cannot only improve the accuracy of the sensor's tuning but also shorten the time of tuning process.

4.1 Background Noise Modeling

Noise, by definition, is any variation in the measurement not caused by actual variations in the external magnetic field. Source of noise in the magnetometer include quantum shot noise, excess noise from the electronics, eddy currents and other technical noise sources form the sensor. Recently, improving the magnetic field measurement accuracy has attracted much research effort. Due to the exponential decay characteristic of FID signal[46], the extraction of high SNR signal within limited time in a noisy background is important for the measurement. Previous work is mainly focused on signal extraction and noise cancellation[80,81]. For theoretical simulation, the correlation adaptive filtering[82] and signal processing techniques like Gabor expansion[83] and Prony[84] were developed and well accepted. Wang[85] proposed a matrix mathematical model constructed by FID signal by combining with frequency division multiplexing (FDM). The results showed that the matrix mathematical model construction based on FDM could meet the requirements from a practical application. However, these methods are still in the stage of simulation, the performance needs to be validated. In a practical scenario, Denisov[14] proposed a linear regression method, which can widen the registration bandwidth and relax the requirements for the magnetometer hardware. In literature[77], the narrow-band noise of FID signal was analyzed and a multi-channel frequency measurement algorithm was proposed. The results showed that when an ordinary proton magnetometer was implemented with this method, the measurement accuracy and resolution can be improved tremendously and close to that of overhauser magnetometer. There are also many other FID signal processing methods being reported[6,79,86–88]. However, there is no research aiming at characterizing the noise of FID signal. Since the severity of the noise degree is a critical factor, most research is to achieve a high SNR signal. Moreover, the frequency measurement algorithm also depends on the SNR. Hence, we need to investigate the noise characteristics of FID signal and identify how the internal or external noises represented by different SNR values affect the measurement accuracy.

In this section, we propose to establish different types of noise models for the FID signal, which are further applied to evaluate the influence of noise on the FID signal quality. As mentioned in previous section, the accuracy of magnetic field measurement with the proton precession magnetometer is determined by the accuracy of FID signal frequency measurement. The SNR is closely related to the frequency measurement. The factors affecting the SNR of FID signal include: white noise, phase noise, narrow-band noise, colored noise, random noise and singular noise. Given the background noise, the FID signal can be modeled as:

$$y(t) = s(t) + \tau(t) \tag{4.1}$$

where $s(t)$ means the original signal and $\tau(t)$ stands for different types of noises.

4.1.1 White Noise

White noise is the major component of the noise source for FID signal, which is also the most common noise in electronic devices and circuits. The thermal noise of resistor and the shot noise of PN junction are all white noise. Since the power spectral density (PSD) of white noise is approximately evenly distributed, the mean of $\tau(t)$ almost approaches zero. Expanding equation 4.1, we can obtain the sinusoidal signal sequence of white signal in a noise environment:

$$\begin{aligned} y(n) &= Ae^{(-t/T_2)}\cos(\omega_0 t) + \tau(n) \\ &= Ae^{(-nt_s/T_2)}\cos(2\pi f_0 n t_s) + \tau(n) \qquad n = 0, 1, ..., N-1 \end{aligned} \tag{4.2}$$

where A is the initial amplitude of FID signal; f_0 is the standard frequency. n and t_s are the sampling points and sampling period, respectively. t stands for the sampling time from zero to the sampling point n. Hence t equals to nt_s. $\tau(n)$ stands for the white noise sequence whose mean is zero and variance is σ^2. In this case, SNR equals to A^2/σ^2. According to the Euler formula:

$$\begin{cases} e^{j\omega_0 t} = \cos\omega_0 t + j\sin\omega_0 t \\ e^{-j\omega_0 t} = \cos\omega_0 t - j\sin\omega_0 t \end{cases} \tag{4.3}$$

there is:

$$\cos\omega_0 t = \frac{e^{j\omega_0 t} + e^{-j\omega_0 t}}{2} \tag{4.4}$$

Hence equation 4.2 can be rewritten as:

$$y(n) = (1/2)A[\exp(-nt_s/T_2 + j\omega_0 n t_s) + \exp(-nt_s/T_2 - j\omega_0 n t_s)] + \tau(n) \tag{4.5}$$

Because $\exp(-nt_s/T_2)$ does not directly relate to the frequency of FID signal, $y(n)$ can be separated into two parts:

$$\begin{cases} y_1(n) = A'\exp(j\omega_0 n t_s) + \tau(n) = A'\exp(j2\pi f_0 n t_s) + \tau(n) \\ y_2(n) = A'\exp(-j\omega_0 n t_s) = A'\exp(-j2\pi f_0 n t_s) \\ y(n) = y_1(n) + y_2(n) \\ A' = (1/2)A\exp(-nt_s/T_2) \end{cases} \tag{4.6}$$

In an ideal situation, frequency f_0 and its estimation f is close to each other. To obtain the modulus square of the signal, we assume that this case is true and construct two new sequences as:

$$\begin{cases} {y_1}'(n) = \exp(j\omega n t_s) = \exp(j2\pi f n t_s) \\ {y_2}'(n) = \exp(-j\omega n t_s) = \exp(-j2\pi f n t_s) \end{cases} \tag{4.7}$$

thereby multiplying equation 4.6 with the conjugation of equation 4.7, we can get:

$$\begin{aligned} |z(n)|^2 &= y_1(n) * {y_1}'(n) + y_2(n) * {y_2}'(n) \\ &= [A' \exp(j2\pi f_0 n t_s) + \tau(n)] \exp(-j2\pi f n t_s) + A' \exp(-j2\pi f n t_s) \exp(j2\pi f_0 n t_s) \\ &= 2A' \exp[j2\pi(f_0 - f) n t_s] + \tau(n) \exp(-j2\pi f n t_s) \\ &= 2A' \exp(j2\pi \Delta f_w n t_s) + \tau'(n) \end{aligned} \tag{4.8}$$

where $\Delta f_w = f_0 - f$, which is the frequency estimation error. $\tau'(n) = \tau(n)\exp(-j2\pi f n t_s)$. The summation of $z(n)$ is implemented by statistical stacking M points in the $z(n)$ domain, and the total samples are $L = N/M$. Given an integer L, a new sequence can be obtained:

$$s(m) = \sum_{n=mM}^{(m+1)M-1} z(n) \qquad m = 0, 1, ..., L-1 \tag{4.9}$$

where $s(m)$ is a sine wave sequence. Frequency deviation is Δf_w while sampling interval is Mt_s. And there are L samples in total. Equation 4.9 can be described as the frequency measurement error of a signal that estimated by computing its $L-$points discrete Fourier transform (DFT). Due to the DFT effectively integrates the M data samples, the amplitude of the original signal is increased by M times. The amplitude of the white noise $\tau(n)$ remains approximately unchanged because of its even distribution. In consequence, the SNR of $s(m)$ is SNR' = MA^2/σ^2 = $M\times$SNR. Compared with $y(n)$, the SNR has been improved up to M times. However, this dose not indicate that the larger the number M the better the SNR will be. According to the principle of DFT, one of the critical factor is that $L \geq M$. Furthermore, the selection of M depends on some other factors such as the frequency of FID signal f_0, the total number of sampling points N, etc. Therefore, different considerations about M need to be confirmed based on different situations.

4.1.2 Narrow-band Noise

A narrow-band filter is commonly used to improve the SNR of FID signal[78,89] by further suppressing the noise. However, the narrow-band noise will be introduced by the filtering operation[80]. The narrow-band noise residing in the FID signal can be expressed as:

$$x(t) = A\sin(2\pi f_0 t) + a\sin[2\pi f_0 t + \psi(t)] \tag{4.10}$$

where a is the maximum amplitude of random noise and $\psi(t)$ is the phase of random noise. According to[80] there is $A \gg a$, then equation 4.10 can be written as:

$$x(t) = A\sin(2\pi f_0 t \pm \frac{a}{A}) \tag{4.11}$$

From equation 4.11, we observe the the amplitude of FID signal with narrow-band noise keeps unchanged but comes with a phase error. The phases error can be expressed as:

$$dt = \frac{T_0 \frac{a}{A}}{2\pi} = \frac{a}{A 2\pi f_0} \tag{4.12}$$

where T_0 is the period of FID signal. In the frequency measurement, a trigger error dt will be created at the first and last rising edges of the measured signal. Therefore, the absolute error of the measured time is twice of dt, and the relative error is:

$$\delta = \frac{2dt}{NT_0} = \frac{2a}{A 2\pi f_0 N T_0} = \frac{a}{A} \times \frac{1}{\pi N} \tag{4.13}$$

The count number of measured signal is N. Thus, the absolute error of frequency measurement is:

$$\Delta f_b = \delta \times f_0 = \frac{a}{A} \times \frac{f_0}{\pi N} = \frac{a}{A} \times \frac{1}{\pi N T_0} \tag{4.14}$$

where NT_0 stands for the actual gate time T. Given the peak signal-to-noise ratio SNR_{pp} = A/a, equation 4.14 changes to:

$$\Delta f_b = \frac{1}{\pi} \times \frac{1}{SNR_{pp} T} \tag{4.15}$$

Equation 4.15 gives the error of frequency measurement caused by the trigger error, especially when the FID signal contains narrow-band noise. From equation 4.15, we find the larger the SNR_{pp} or the longer the measured time T the smaller the absolute error. Therefore, in some applications when the required frequency measurement error is not greater than Δf_b, the SNR_{pp} needs to meet the following requirement:

$$SNR_{pp} \geq \frac{1}{\Delta f_b} \times \frac{1}{\pi T} \tag{4.16}$$

4.1.3 Overall Noise Model

There are also other noises such as the colored, random and singular noises, which are relatively weak. Furthermore, their noise distributions are irregular[90]. Hence, in the calculation of overall noise model, they can be ignored. For the white and narrow-band noises mentioned above, according to the noise distribution function, they need to be statistical averaged by multiple measurements, and the weighting coefficients will be obtained[91]. Then, the results will be added to the total noise expression. Based on[92], the distribution function of white noise can be written as:

$$P_w(t) = \frac{1}{\sqrt{2\pi}} \int_0^T \exp^{-t^2/2} dt \tag{4.17}$$

and that of narrow-band noise is:

$$P_b(t) = \frac{2}{T} \int_0^T \cos 2\pi f_0 t dt + \frac{2}{T} \int_0^T \sin 2\pi f_0 t dt \tag{4.18}$$

In this calculation, first, Monte Carlo method[93] is used to generate noises sequence according to each noise distribution. Second, we conduct multiple statistical tests of the weighting coefficients and superimpose them every time. Finally, calculate the mean of each sum of the weight, respectively. Thereby, the weighting coefficient of each noise is obtained. Overall, according to equation 4.8 and 4.15, through the weighted summation, superposition of the noise distribution functions (refer to equation 4.17 and 4.18) and experimental samples of all noises, we can further calculate the relationship between the SNR of FID signal and the accuracy of frequency measurement as:

$$\begin{aligned} \Delta f &= [\frac{1}{\hat{N}} \sum_{i=1}^{\hat{N}} \alpha^{(i)} P_w(t)] \times \Delta f_w + [\frac{1}{\hat{N}} \sum_{i=1}^{\hat{N}} \beta^{(i)} P_b(t)] \times \Delta f_b \\ &\approx (1/SNR_{pp}^2) \times \pi T + e^{-\alpha} \times \frac{1}{2\pi T \sqrt{SNR_{pp}}} - In\beta / \sqrt{SNR_{pp}} \end{aligned} \tag{4.19}$$

where α and β are weighting coefficients. $\hat{N}$ stands for the total number of superimposition, which is defined as 10. Through the statistical averaging process on $\alpha(i)$ and $\beta(i)$ based on the steps mentioned above, we can calculate that $\alpha \approx 3.712 \sim 4.803$ and $\beta \approx 1.001 \sim 1.013$. Examples and additional details are given in[92,94]. Then, we can obtain:

$$\begin{aligned} f &= f_0 + \Delta f \\ &\approx f_0 + (1/SNR_{pp}^2) \times \pi T + e^{-\alpha} \times \frac{1}{2\pi T\sqrt{SNR_{pp}}} - In\beta/\sqrt{SNR_{pp}} \end{aligned} \tag{4.20}$$

where f is the measured frequency of FID signal. f_0 is the standard frequency and Δf is the total measurement error. According to equation 4.20, the measured frequency value f is mainly determined by measurement time T and SNR_{pp}, which is approximately consistent with equation 4.15 despite the weighting coefficients calculation of different noises. The relationship between SNR_{pp} and the frequency measurement error can be obtained as shown in Figure 4-1. It is observed that the higher the SNR_{pp} the higher the accuracy of frequency measurement. When SNR_{pp} is in the range $0 \sim 5$; if SNR_{pp} increases, the error of frequency measurement will decrease faster, thereby improving the accuracy significantly. When SNR_{pp} is in the range $5 \sim 20$; if SNR_{pp} increases, the error of frequency measurement will decrease slower, and the improvement of accuracy is not obvious.

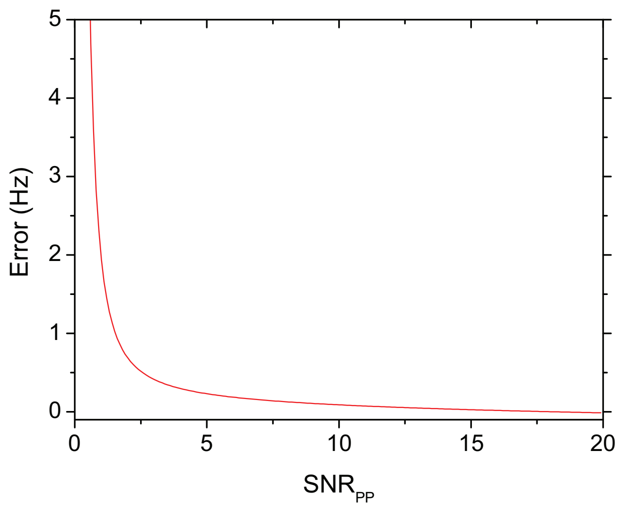

Figure 4-1: The relationship between frequency measurement accuracy and SNR_{pp} in simulation (T = 1.0, α = 4.803, β = 1.001, SNR_{pp} changes from 0.01 to 20 and step value is 0.1).

4.1.4 Model Evaluation

Simulation

Based on the theoretical analysis and the background noise model of FID signal for the proton precession magnetometer, we can quantify the relationship between SNR and the accuracy of frequency measurement by using the probability distribution of random noises generated by Monte Carlo simulation[93]. The simulation results are given in Table 4.1. To further identify whether the resolution can reach up to 0.001 Hz, we set the frequency of FID signal to 2100 Hz and 2100.001 Hz, respectively.

Table 4.1: The theoretical relationship between frequency measurement accuracy and SNR of FID signal.

SNR (dB)	Standard (Hz)	Measured (Hz)	Absolute error (Hz)	Root mean square error (Hz)
0.1	2100	2101.700	1.7	5.576×10^{-1}
3	2100	2100.600	0.6	6.547×10^{-2}
6	2100	2100.250	0.25	2.341×10^{-2}
9	2100	2100.092	0.092	5.973×10^{-3}
12	2100	2100.075	0.075	5.243×10^{-3}
15	2100	2100.046	0.046	3.648×10^{-3}
18	2100	2100.015	0.015	2.134×10^{-3}
20	2100	2100.009	0.009	1.776×10^{-3}
0.1	2100.001	2101.700	1.699	5.576×10^{-1}
3	2100.001	2100.600	0.599	6.547×10^{-2}
6	2100.001	2100.250	0.249	2.341×10^{-2}
9	2100.001	2101.092	0.091	5.973×10^{-3}
12	2100.001	2101.072	0.071	5.257×10^{-3}
15	2100.001	2101.048	0.047	3.689×10^{-3}
18	2100.001	2101.018	0.017	2.182×10^{-3}
20	2100.001	2101.012	0.011	1.806×10^{-3}

As shown in Table 4.1, when SNR is in the range $0.1 \sim 9$ dB, the absolute error will decreases rapidly with the increase of SNR. The measured accuracy will be improved significantly. When SNR is in the range $9 \sim 20$ dB, the absolute error will decreases slower as the SNR increases. And the improvement of accuracy is not obvious. In addition, the sensitive of frequency measurement can be evaluated by the root mean square error (RMSE), which reflects the degree of deviation of data from the average. From Table 4.1, the trend of RMSE changes with SNR is similar to the absolute error.

Test in the field

In practical applications, the major noise component of FID signal is the white noise, but there still exist phase, colored, singular and random noise interferences[76]. To further validate the theoretical analysis and calculations above, we adopted the developed prototype to verify the noise model.

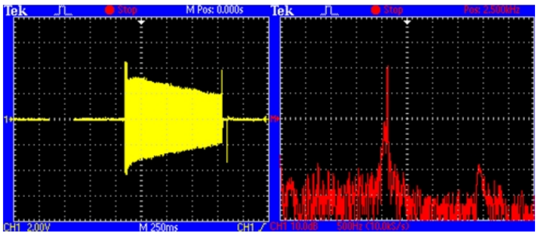

(a) SNR = 40dB.

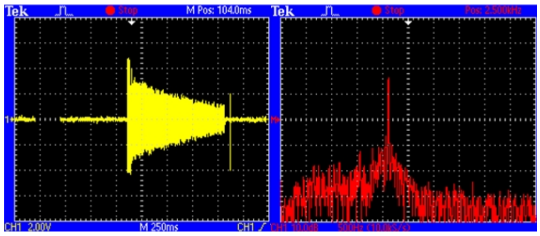

(b) SNR = 30dB.

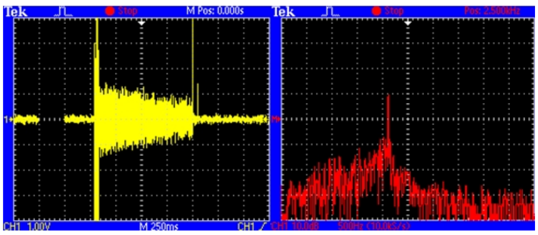

(c) SNR = 20dB.

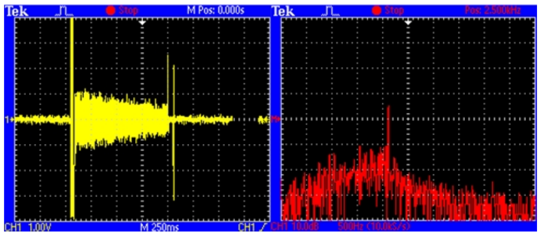

(d) SNR = 15dB.

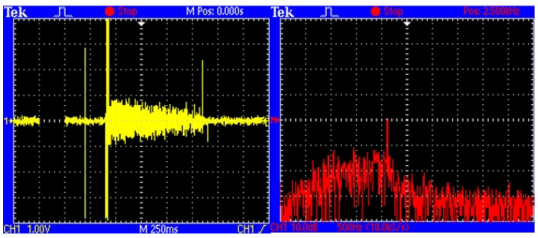

(e) SNR = 10dB.

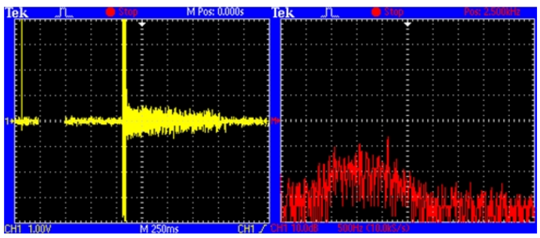

(f) SNR = 3dB.

Figure 4-2: The FID signal with different SNRs and corresponding FFT results.

We chose a test location with less interference, and the magnetic field strength is approximately 49670 nT, corresponding to a frequency of 2114.75 Hz. According to[53], the different SNRs of FID signal can be obtained by changing the polarized time and power. Figure 4-2 shows the FID signal with different SNRs and corresponding fast Fourier transform (FFT) results. From the signal, we observe that the longer the time the smaller the amplitude of the signal, which is consistent with the exponential decay characteristic of FID signal. From the FFT results, we observe that the SNR of obtained FID signal are approximately 40 dB, 30 dB, 20 dB, 15 dB, 10 dB and 3 dB, respectively, and each of the corresponding FFT value shows that the center frequency is around 2110 Hz, which corresponds to the FID signal frequency of the magnetic field at the test location.

For each of the SNR, 1000 sets of data were collected. Due to the existence of magnetic field diurnal variation, the data will be affected if only one instrument is used. Therefore, a second instrument of the same performance is used as a reference, and the influence of diurnal variation can be eliminated by the difference of the measured data of two instruments. The distance between two instruments is about 10 m, and measurement period is 20 s. After all measurements were completed, the averaged difference of the two samples was calculated to remove the constant magnetic field shift due to the location difference of the two instruments. Then, the mean square error (MSE) was calculated and obtained. The results are given in Table 4.2 and Figure 4-3.

Table 4.2: The practical relationship between frequency measurement accuracy and SNR of FID signal.

SNR (dB)	Magnetic field (nT)	Frequency (Hz)	Absolute error (Hz)	Mean square error (Hz)
3	49735.24	2117.53	0.265	0.256
6	49720.24	2116.89	0.137	0.120
10	49695.82	2115.85	0.046	0.042
15	49683.37	2115.32	0.041	0.036
20	49675.38	2114.98	0.037	0.034
30	49670.45	2114.77	0.035	0.024
40	49670.18	2114.76	0.030	0.015

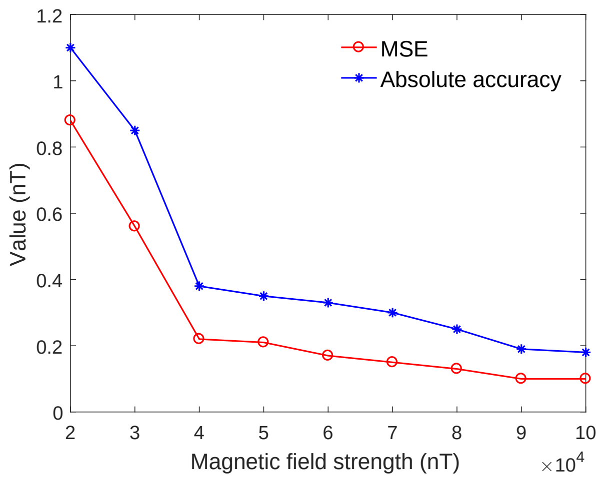

Figure 4-3: The relationship between the accuracy of frequency measurement and SNR in the field tests.

Generally, if the SNR of FID signal is much lower in a practical application, the error of frequency measurement can be too large and the measurement data do not make any sense[43,95]. Therefore, the SNR we measured ranged from 3 dB to 40 dB in the specific test environment. From Table 4.2 and Figure 4-3, we find that when the SNR increases in the range 3 $\sim$ 10 dB, the absolute error and mean square error (MSE) all decrease rapidly, which means a significant improvement in accuracy. When SNR is in the range 10 $\sim$ 40 dB, the absolute error and MSE will decrease slower, and the improvement of accuracy is not obvious. In addition, the trends of two curves are almost the same in Figure 4-1 and 4-3. The main difference is that the abrupt increase of absolute error or MSE corresponding to the SNR are 3 dB and 10 dB, respectively, which has a relationship with the test environment, such as the electrical characteristics of circuit and electromagnetic interference etc. Furthermore, in the simulation when the SNR reaches up to 10 dB, the frequency measurement accuracy cannot be improved anymore; while in the practical test, the SNR should be 30 dB or even higher. However, the test results agree well with the theoretical calculation.

As a whole, the trend of the simulation and the field test results are approximately consistent. The well-known fact that it is possible to get a lower frequency measurement error with a better SNR, which is behind unclear mathematical manipulations, is described in a quantitative way.

4.2 Multi-channel Frequency Measurement

From equation 2.9, we observe that the FID signal frequency is proportional to the strength of the magnetic field, which implies the accuracy of frequency measurement determines the accuracy of the derived magnetic field. Therefore, research on high-precision frequency measurement is very important. In general, the transverse relaxation time T_2 is no more than 1 s. For a weak geomagnetic field signal, it is difficult to measure due to the considerable noises. Before the 1990s, the proton precession magnetometer was used to measure the frequency of the FID signal after phase locked and frequency doubled. Due to the short duration of the FID signal, frequency measurement error cannot meet the high- accuracy requirement. After the 2000s, with the development of microelectronics technology, the FID signal was measured by technologies such as the equal precision frequency measurement by field-programmable gate array (FPGA) technology, which greatly improved the accuracy of the frequency measurement.

To date, numerous frequency measurement algorithms have been proposed. In terms of theoretical simulation, several methods for frequency measurement are designed in[96–100], such as the Newton-type technique, adaptive-based algorithm, time-frequency distributions based on the adaptive fractional spectrogram, autocorrelation factor-based algorithm, and estimation method using Kronecker's theorem. Based on the results of simulation, these methods all can achieve high accuracy and high sensitivity. However, all of these methods stayed only in the stage of theoretical simulation had not applied in actual environment. Their performance remains to be verified. Some methods have been applied to practical scenarios. Buajarern proposed an absolute frequency measurement using the optical frequency comb technique[101]. The experimental results show that the accuracy of frequency measurement can meet the high-resolution requirement. However, due to its dependence on a huge test system, this method cannot be applied in the proton magnetometer. Two instantaneous frequency measurement methods based on four-wave mixing and six-port technology, respectively, are designed in[102] and[103], but the experimental results show that the two methods would be better applied in the high-frequency measurement. Tong[104] and Dong[105] designed an all-phase fast Fourier transform (FFT) cymometer, but the experimental results show that the relative errors of measurement are larger than 0.02% in the frequency range 850 Hz $\sim$ 4300 Hz. The accuracy cannot meet the high-resolution requirement of the proton magnetometer. Zhang[79] proposed an interpolation algorithm using zero crossing to improve the accuracy of frequency measurement, but due to the fast decay of the FID signal-to-noise ratio (SNR), the interpolation error increases with time, so the best measurable time is limited. Wang[106] and Li[107] proposed an improved algorithm using weighted phase difference, but the algorithm is applicable only to the case of high SNR. Ye[108] proposed a frequency measurement based on Fourier algorithm for better accuracy. However, it requires a much longer time due to the iterative calculations in the algorithm. There are also many other methods to measure frequency[43,109–112], but few of them are aiming at FID signal.

To sum up, in this section, we propose a multi-channel frequency measurement algorithm to improve the accuracy of the measured magnetic fields in a broader dynamic range and in a noisier environment.

4.2.1 Principle of Equal Precision Frequency Measurement

The equal precision frequency measurement method is developed based on a direct frequency measurement method. The actual gate time is determined by the gating signal and the measured signal together in the acquisition, which is a multiple of the measured signal period. This method cannot only improve the accuracy of frequency measurement, but also realize the equal accuracy of measuring frequency in the whole frequency range.

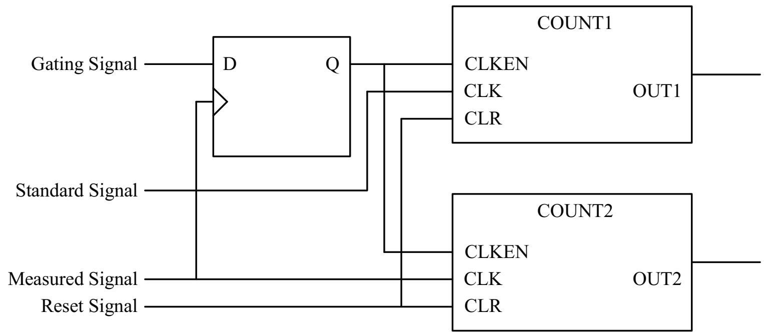

Figure 4-4: Block diagram of equal precision frequency measurement.

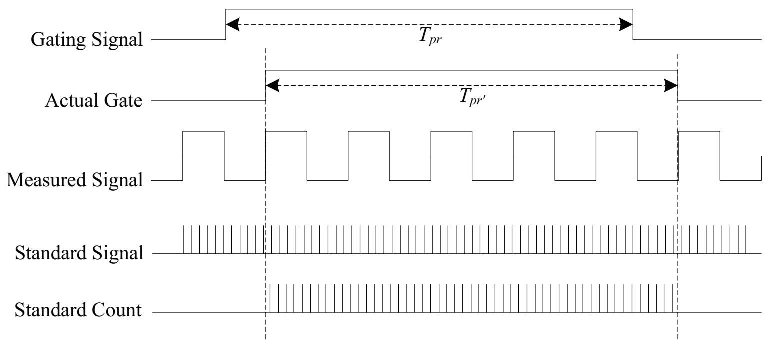

Figure 4-5: Time sequence diagram of equal precision frequency measurement.

Figure 4-4 is the block diagram of equal precision frequency measurement and Figure 4-5 is the time sequence diagram. COUNT1 and COUNT2 are two counters. When gating signal T_{pr} (gating time) becomes high, the rising edge of the measured signal, through the flip side Q of trigger D, starts COUNT1 to count the measured signal and COUNT2 to count the standard signal. When gating signal T_{pr} becomes low, the upcoming rising edge of the measured signal will close COUNT1 and COUNT2. The frequency of the measured signal f_x can be obtained using the reading values of the two counters and the frequency of the standard signal as:

$$f_x = \frac{N_x}{N_s} \times f_s \tag{4.21}$$

where f_s is the frequency of the standard signal, N_x is the counter value of the measured signal, and N_s is the counter value of the standard signal.

4.2.2 Mathematical Model of Frequency Measurement Error

According to the principle of equal precision frequency measurement, the actual gate time is determined by gating signal and measured signal together in the acquisition, which is a multiple of the measured signal period. Hence, there is no count error (± 1) for the measured signal, but still exists in standard signal[113].

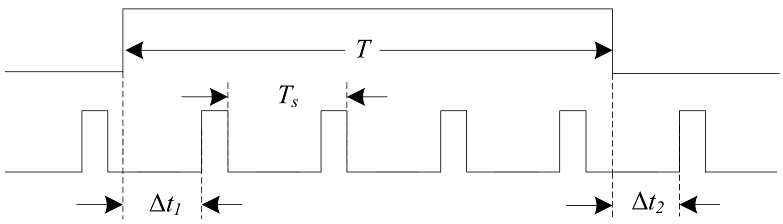

Figure 4-6: Schematic diagram of the count error.

Figure 4-6 shows the schematic diagram of the count error. T is the gating time, T_s is the frequency of standard signal, Δt_1 is the time from gating open time to the first count pulse edge, Δt_2 is the time from gating close time to the next count pulse edge. According to Figure 4-6, we can realize that:

$$T = N_s T_s + \Delta t_1 - \Delta t_2 = N_s + \frac{\Delta t_1 - \Delta t_2}{T_s} \times T_s \tag{4.22}$$

where, N_s is the counter value of the standard signal. ΔN_s is the count increment (count error), which equals to $(\Delta t_1 - \Delta t_2)/T_s$. Considering that $\Delta t_1 \leq Ts$, $\Delta t_2 \leq Ts$, there is $|\Delta t_1 - \Delta t_2| \leq T_s$. In this case, $|\Delta N_s| \leq Ts$, and the ΔN_s has only three possible values: $\Delta N_s = -1, 0, 1$. Therefore, the maximum absolute error of N_s is ± 1. In consequence, in equation 4.21, the value of N_s can have one count error (± 1). Assuming that the probability of causing the count error is P, the quantization error is $N_s = (1-P) \cdot 0 +$

$P \cdot |\pm 1| = P$, where $0 < P < 1$. Then, the relative error can be written as:

$$\delta = \frac{|\frac{N_x}{N_s} \cdot f_s - \frac{N_x}{N_s+\Delta N_s} \cdot f_s|}{\frac{N_x}{N_s+\Delta N_s} \cdot f_s} = \frac{\Delta N_s}{N_s} < \frac{1}{N_s} \tag{4.23}$$

Referring to[77], equation 4.23 can be represented as:

$$|\delta| = \frac{1}{T \cdot f_s} \tag{4.24}$$

where T is the actual gate time and f_s is the frequency of standard signal. For example, if the gate time is 0.5 s and the frequency of standard signal is 50 MHz, the relative error is ±0.04 ppm. Likewise, the maximum absolute error in the frequency range 850 Hz $\sim$ 4300 Hz is about ±0.00017 Hz, which corresponds to a magnetic field error of ±0.004 nT.

4.2.3 Proposed Method

From equation 4.24, we know that the relative error can be reduced by increasing N_s. Two ways are possible: 1) increasing the frequency of standard signal and 2) increasing the gate time. However, increase in f_s is limited and the gate time cannot be too long because of the exponent decay of the FID signal. To overcome the disadvantages of the aforementioned two ways, we propose a multichannel frequency measurement method that takes advantage of the parallel processing of FPGA.

For example, we can select n channels and choose the gate time to match T_2. After one cycle, the counter readings of the n channels of the standard signal are $N_{s1},...,N_{sn}$ and the counter readings of the n channels of the measure signal are $N_{x1},...,N_{x1}$. Following the same idea as that for equation 4.21, the frequency of the measured signal can be calculated:

$$f_x = \frac{N_{x1} + N_{x2} + ... + N_{xn}}{N_{s1} + N_{s2} + ... + N_{sn}} \times f_s \tag{4.25}$$

Based on equation 4.25, we know that the total count N_s has been increased but the gate time is kept nearly unchanged. This is equivalent to increasing the frequency measurement time. According to equation 4.24, the relative error δ' of frequency measurement now becomes:

$$|\delta'| = \frac{1}{nT \cdot f_s} \tag{4.26}$$

Equation 4.26 shows that the proposed method can reduce the error n times compared with general equal precision frequency measurement and increase the accuracy in the effective measuring time of the FID signal.

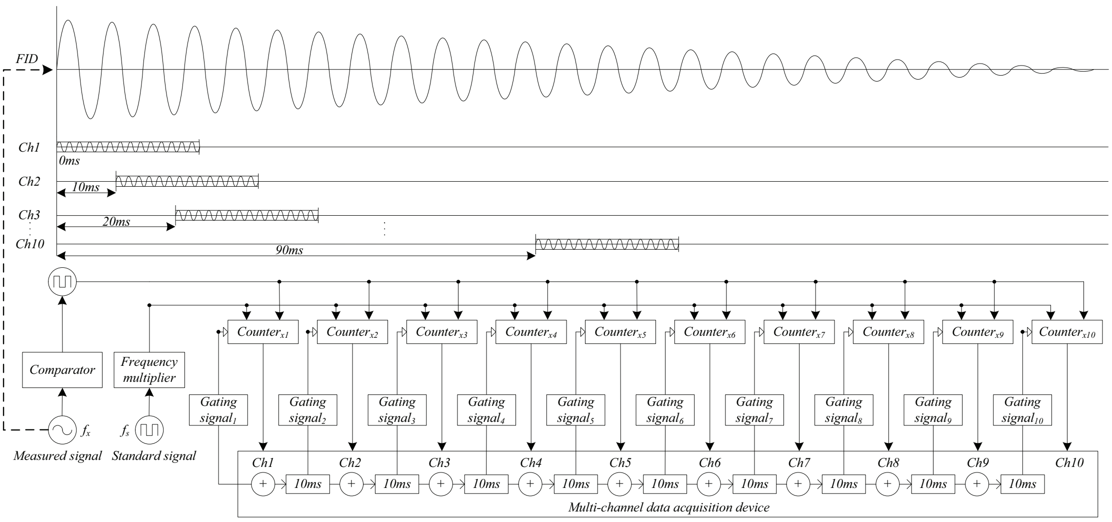

Figure 4-7: Schematic diagram of the multi-channel parallel frequency measurement algorithm.

In one practical implementation, we select ten channels. Figure 4-7 shows the sequence diagram of ten-channel frequency measurement. First, channel one starts to count frequency and then channel two starts after a 10 ms delay while channel one is still measuring frequency. The remaining eight channels proceed in turn like this until channel ten finishes. The frequency measurement time (counting time) of the proton magnetometer is usually 500 ms. However, using the proposed method, the total counting time is 500 ms $\times$ 10 = 5000 ms, and the actual frequency measurement time in one cycle is 500 ms + 90 ms = 590 ms. Only an extra 90 ms is taken and this is trivial compared with the completely sampling period. In summary, the proposed method can finish measuring the frequency of the FID signal without much increase in the sampling period but with great increase in N_s , which can greatly reduce the relative error.

In addition, since the trigger error is mainly caused by the glitches of the signal as shown in Figure 4-8. The signal is superposed by the square wave and white noise. During the frequency measurement, in the process of the first rising edge, the noise makes the trigger ahead of time ΔT_1, and makes the trigger ahead of time ΔT_2 in the process of the second rising edge. Therefore, in the whole period, the trigger error

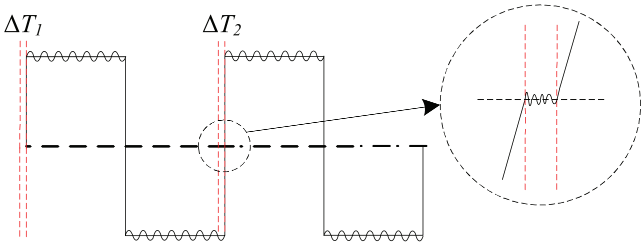

Figure 4-8: Schematic diagram of how the trigger error be generated.

caused by noise is $\Delta T_1 - \Delta T_2$. If the period of measured signal is T, the relative error of frequency measurement is $(\Delta T_1 - \Delta T_2)/T$. According to the principle of equal precision frequency measurement, the trigger error cannot be totally removed. There are many factors, such as the electrical noise, random noise, etc. In this study, in order to reduce the effect of the trigger error on the accuracy of frequency measurement, while using the proposed algorithm, a glitch filtering module is applied in FPGA, the specific operation are as follows.

Step 1: Once the rising edge is detected, delay dozens of counting clock rather than count immediately.

Step 2: If a level transition occurred during this time, it is proved to be a glitch, and the counting clock will not be opened.

Step 3: If not, it should be considered as a real rising edge, then open the counting clock.

The above methods can suppress the glitches of the signal effectively, further reducing the trigger error influence, thereby increasing the accuracy of frequency measurement.

4.3 Secondary Tuning Based on SVD & STFT

To improve the accuracy of magnetic field measurement, a variable capacitor is always applied to tune and obtain the effective signal from the coil of the sensor, which can improve the SNR (Signal Noise Ratio) of the FID signal[114]. Currently, the instruments of America and Canada have mainly adopted the scanning[115,116] and preset capacitance methods[117–119]; the domestic instruments have mainly adopted the blindly automatic tracking and second measurement with automatic tracking methods[43,120,121]. However, the core working principle of all the methods is the same, as is shown in Figure

4-9: after exciting the sensor, the capacitor is switched, and then the peak voltage of the untuned FID signal is tested, with the corresponding capacitor of the maximum peak being the value of tuning. The only difference is the detection method of the peak voltage. However, these methods have the disadvantages of a slower speed of tuning (approximately a few seconds), the possibility of mis-tuning, etc. Tan and Dong proposed a method based on the FFT (Fast Fourier Transform): apply an Analog to Digital Converter (ADC) to finish the acquisition of the amplified untuned FID signal, calculate the gathered data with autocorrelation, and then the spectrum can be obtained by FFT[122]. This method can improve the speed of tuning, but the method is only applicable to the case of a non-interferential environment.

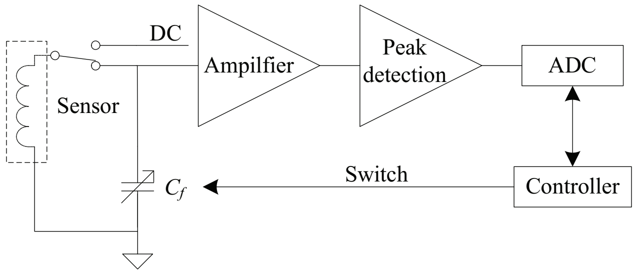

Figure 4-9: Schematic diagram of the conventional core tuning principle.

Aimed to solve these problems mentioned above, we propose a secondary tuning algorithm based on Singular Value Decomposition (SVD) and Shot time Fourier Transform (STFT). First, the space matrix is constructed by the acquisition of ADC for the untuned FID signal, and then the SVD is performed to eliminate the noise and obtain the useful signal. Finally, the STFT technique is applied to extract the time-frequency feature. Thus, a frequency value f_1 is determined primarily, switching the capacitor to finish the first tuning. After that, the conventional steps of magnetic field measurement are adopted with the first tuning capacitor, and then a frequency value f_2 can be obtained by measuring the frequency of the FID signal. f_2 is closer to the actual frequency f_0 than f_1 is. Then, apply the frequency value f_2 to control the tuning capacitor and center frequency of the narrow-band filter, which can improve the SNR of the signal, to increase the accuracy of the magnetic field measurement; this is the work process of secondary tuning. The proposed algorithm have some advantages, it not only improves the accuracy of the sensors tuning but also shortens the time of tuning process (no more than 1 s). Furthermore, the problem of sensor mis-tuning in strong-disturbance environments should be solved.

4.3.1 Sensor Tuning

The essence of the tuning of a proton precession magnetometer is *LC* series resonance, and the center frequency f_0 can be calculated via:

$$f_0 = \frac{1}{2\pi\sqrt{LC}} \tag{4.27}$$

where L is the inductance of the sensor, C is the variable tuning capacitor, R is the internal resistance of the sensor, and the quality factor Q of the resonance circuit is:

$$Q = \frac{\omega}{R} = \frac{2\pi f_0 L}{R} \tag{4.28}$$

and the bandwidth BW of the resonant circuit is:

$$BW = \frac{f_0}{Q} \tag{4.29}$$

The parameters of the sensor mentioned in this thesis are L = 34 mH and R = 19 Ω. According to equation 4.28 and 4.29 can figure put BW = 84 Hz. Therefore, the signal-to-noise improvement ratio $SNIR$ of the initial FID signal out of sensor is:

$$SNIR = 20\log(\sqrt{\frac{\Delta f}{BW}}) \approx 18.3dB \tag{4.30}$$

where, Δf is the frequency bandwidth of geomagnetic field that equals to 3450Hz. This demonstrates that after the resonance, the amplitude of the signal output of the sensor is Q times that of the untuned signal, which is equivalent to the SNR increasing by lg$Q$ (unit: dB).

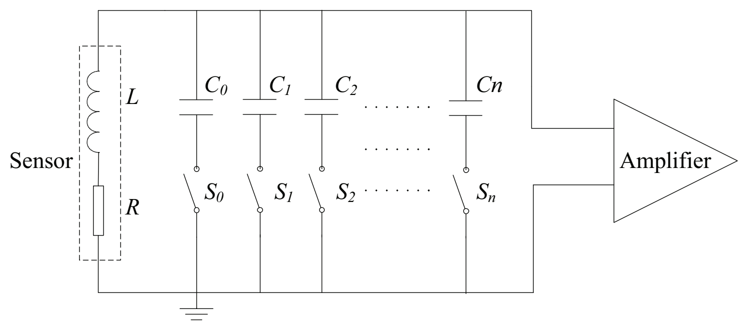

Figure 4-10: Schematic diagram of the adjustment of the variable capacitance.

In the range of the geomagnetic field 20000 nT $\sim$ 100000 nT, the frequency of the

FID signal is in the range of 850 Hz $\sim$ 4300 Hz. The inductance of an ordinary proton precession magnetometer sensor is $L = 34$mH, and according to equation 4.27, the range of the tuning capacitor can be calculated as being 28 nF $\sim$ 1022 nF. However, there is not a variable capacitor that has such a large adjustable range, so the problem can be solved by this method as shown in Figure 4-10. The rules of the capacitor selection are as follows:

$$\begin{cases} C_0 = 1nF \\ C_n = 2C_{n-1}, \quad n = 9 \end{cases} \tag{4.31}$$

Based on equation 4.31, we adopt ten analog switches to control ten capacitors, which can achieve the 1 nF $\sim$ 1023 nF adjustable range of the tuning capacitor, and the resolution is 1 nF. However, the change of the tuning capacitor would cause the change of the resonance center frequency; if the value of the capacitor changed by 1 nF, according to equation 4.27, the change of the resonance center frequency can be written as:

$$\begin{cases} \Delta f = \frac{1}{2\pi\sqrt{LC_2}} - \frac{1}{2\pi\sqrt{LC_1}} \\ C_2 - C_1 = 1nF \end{cases} \tag{4.32}$$

Hence, the curve between the variable of the resonant frequency and the tuning ca-

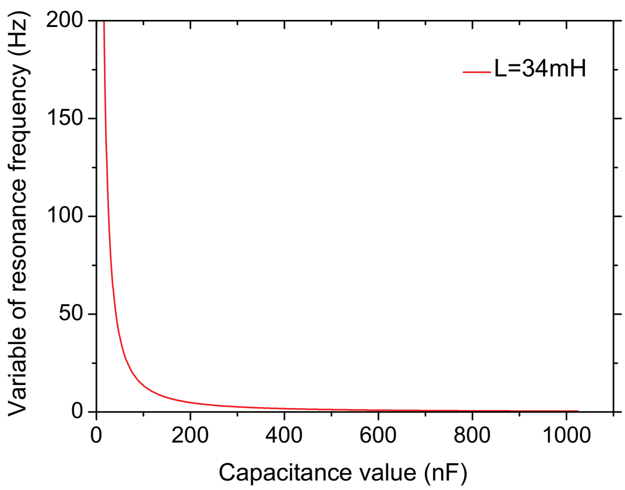

Figure 4-11: Curve between the variable of the resonant frequency and the tuning capacitance value.

pacitance value can be obtained, as shown in Figure 4-11. We observe that when the tuning capacitance value is lower, although it changed by 1 nT, the center frequency of the resonant circuit also changed by nearly 150 Hz. We suppose that, in the range of the geomagnetic field, the accurate tuning capacitance value is 40 nF; however, if the tuning capacitor value has a slight deviation, such as 38 nF, because of an imperfect algorithm as shown in Figure 4-11, the variable of the resonant frequency can reach up to 60 Hz, which may lead to mis-tuning. Therefore, the SNR of the FID signal will be decreased, as well as the accuracy of the magnetic field measurement.

In addition, the FID signal is a sine wave with the magnitude exponentially decaying, whose duration is 0.5 s $\sim$ 1 s. Therefore, a high-precision, high-speed tuning algorithm should be applied to achieve the best output SNR, thereby improving the accuracy of magnetic field measurement.

4.3.2 SVD Noise Elimination Technology

Through the analysis of the tuning principle of a proton precession magnetometer above, aiming at the current defects, such as slow tuning, the poor performance of adaption to the environment, etc, we propose a secondary tuning algorithm based on SVD and STFT. SVD is applied to the initial noise reduction for the space matrix, which is constructed by the acquisition of ADC for the untuned FID signal, and this can enhance the environmental adaptability of the tuning algorithm. According to the exponential decay characteristic of the FID signal, the STFT technique is applied to the denoised signal to extract the time-frequency feature. Then, the evolution over time of the signal spectrum can be clear, depicting the locality of the signal and retaining all the information as well. The algorithm flowchart is shown in Figure 4-12.

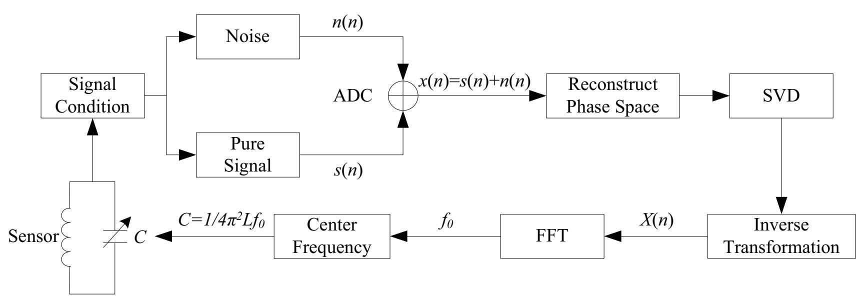

Figure 4-12: Flowchart of the second tuning algorithm.

In Figure 4-12, $s(n)$ is the ideal FID signal, and $n(n)$ is the noise signal. In this algorithm, we adopt SVD to reconstruct the untuned FID signal $x(n)$, and then the reconstructed signal $X(n)$ can be obtained. After that, the STFT is applied to extract the time-frequency feature to determine a frequency value f_1 primarily, switching the tuning capacitor to finish the first tuning. After that, we adopt the conventional steps of magnetic field measurement with the first tuning capacitor, and a frequency value f_2 can be obtained. Then, the frequency value f_2 is applied to control the tuning capacitor and center frequency of the narrow-band filter, and this is the secondary tuning. This algorithm can reduce the circuit bandwidth, improving the SNR, to increase the accuracy of the magnetic field measurement.

SVD is an effective method for feature extraction and is based on the nonlinear filtering method[123,124]. The decomposition value reflects the intrinsic attribute of data; therefore, the background suppression and denoising problems of small target detection can be solved[125,126]. The SVD has been successfully applied to geophysical signal-noise separation technology[127]; compared with other denoising methods, this method has the advantages of better denoising effect and lower signal distortion. The processing of the FID signal is part of the geophysical signal-noise separation, in addition, it belongs to the background suppression and denoising problem of small target detection as well, so SVD can be applied to FID signal processing.

The original sample sequence of an untuned FID signal is $x_i, i = 1,2,3,...,n$, and the steps for eliminating noises by SVD are as follows:

Step 1: Extract the subsequence $x_1,x_2,...,x_n$ from the original sample sequence as the first vector y_1 of the reconstructed phase space.

Step 2: Move this subsequence to the right by one step, forming a new sequence $x_2,x_3,...,x_{n+1}$ as the second vector y_2 of the reconstructed phase space.

Step 3: Repeat steps 1 and 2, and a column vector $y_1,y_2,...,y_m$ can be obtained.

Step 4: Because each of the vectors corresponds to a point of the reconstructed phase space, all vectors constitute the $m \times n$ dimensional matrix as:

$$D_m = \begin{bmatrix} x_1 & x_2 & \dots & x_n \\ x_2 & x_3 & \dots & x_{n+1} \\ \dots & \dots & \dots & \dots \\ x_m & x_{m+1} & \dots & x_{n+m-1} \end{bmatrix} \tag{4.33}$$

D_m is the reconstruction of the phase space, reformulating equation 4.33 using SVD:

$$D_m = USV^T \tag{4.34}$$

where U is the $m \times m$ orthogonal matrix called the left singular matrix, V is the $n \times n$ orthogonal matrix called the right singular matrix, S is the $m \times n$ diagonal matrix, and $\sigma_1, \sigma_2, ..., \sigma_r$ are its diagonal elements ($\sigma_1 \geq \sigma_2 \geq ... \geq \sigma_r$, r is the rank of D_m) called the singular value of D_m. According to[128], in equation 4.34, the matrix V can be obtained from the diagonal factorization ${D_m}^T D_m = VDV^T$, in which the diagonal entries of D appear in non-increasing order; the columns of U come from normalizing the non-vanishing images under D_m of the columns of V; the nonzero entries of S are the respective square roots of corresponding diagonal entries of D. In summary, the columns of U are eigenvectors for D_m and form an orthonormal basis $u_1, u_2, ..., u_m$, the columns of V are eigenvectors for D_m and form an orthonormal basis $v_1, v_2, ..., v_n$. Assembling the v_i as the columns of a matrix V and the u_i to form U, we have $D_m V = US$ for all $i \leq r$, where S has the same dimensions as D_m, has the entries σ_i along the main diagonal, and has all other entries equal to zero. Therefore, equation 4.34 can be expressed using partitioned matrices as follows:

$$D_m = \begin{bmatrix} u_1 & \cdots & u_r & | & u_{r+1} & \cdots & u_m \end{bmatrix} \begin{bmatrix} \sigma_1 & & & & & & 0 \\ & \sigma_2 & & & & & \\ & & \ddots & & & & \vdots \\ & & & \sigma_r & & & \\ & & & & 0 & & \\ & & & & & \ddots & \vdots \\ 0 & & \cdots & & & \cdots & 0 \end{bmatrix} \begin{bmatrix} v_1^T \\ \vdots \\ v_r^T \\ - \\ v_{r+1}^T \\ \vdots \\ v_n^T \end{bmatrix} \tag{4.35}$$

Because the untuned FID signal contains noises, D_m can be written as $D_m = D_s + D_n$. D_s is the matrix without noise, and D_n is the matrix of noise. Based on the above analysis, D_m can be rewritten as:

$$D_m = D_s + D_n = \begin{bmatrix} U_s & U_n \end{bmatrix} \begin{bmatrix} S_s & 0 \\ 0 & S_n \end{bmatrix} \begin{bmatrix} V_s^T \\ V_n^T \end{bmatrix} = U_s S_s V_s^T + U_n S_n V_n^T \tag{4.36}$$

where S_s is the $r \times n$ diagonal matrix of the main singular value and S_n is the diagonal matrix of the noise singular value. When the partitioned matrices of equation 4.35 are multiplied, D_m can be written as:

$$D_m = \begin{bmatrix} u_1 & \cdots & u_r \end{bmatrix} \begin{bmatrix} \sigma_1 & & \\ & \ddots & \\ & & \sigma_r \end{bmatrix} \begin{bmatrix} v_1^T \\ \vdots \\ v_r^T \end{bmatrix} + \begin{bmatrix} u_{r+1} & \cdots & u_m \end{bmatrix} \begin{bmatrix} 0 \end{bmatrix} \begin{bmatrix} v_{r+1}^T \\ \vdots \\ v_n^T \end{bmatrix} \tag{4.37}$$

From equation 4.37 it is clear that only the first r u's and v's make any contribution to D_m, the $(m-r)u$'s and v's belong to the noise part of D_m. Therefore, according to equations 4.36 and 4.37, the matrix D_s after noise reduction can be written as:

$$D_s = U_s S_s V_s^T = \begin{bmatrix} u_1 & \cdots & u_r \end{bmatrix} \begin{bmatrix} \sigma_1 & & \\ & \ddots & \\ & & \sigma_r \end{bmatrix} \begin{bmatrix} v_1^T \\ \vdots \\ v_r^T \end{bmatrix} \tag{4.38}$$

Then, apply the inverse process of SVD to obtain a matrix D', which is the characteristics signal after noise elimination.

4.3.3 STFT Time-Frequency Feature Extraction Technology

The standard Fourier transform translates the signal from the time domain to the frequency domain, which means that $f(x)e^{ix\omega}$ is superimposed on the entire time line. $e^{ix\omega}$ is used to limit the frequency; therefore, the standard Fourier transform only has local analysis capabilities in the frequency domain but not in the time domain. Because the FID signal exponentially decays with time, the signal needs to be divided into several small intervals to analyze the time-frequency feature accurately, and the Fourier transform is adopted to analyze each of the intervals to determine the frequency feature, thereby increasing the accuracy of signal feature extraction. STFT is the short time Fourier transform, which uses a movable window for the Fourier transform[129].

Consider the function x(t) to be the acquisition data of the FID signal by ADC, and its STFT can be written as[130]:

$$STFT_x(\tau, f) = \int x(t) g^*_{\tau,f}(t) dt = \int x(t) g^*(t-\tau) e^{-jf\tau} dt \tag{4.39}$$

where the window function $g(t)$ is used to intercept $x(t)$ for the short time Fourier transform, and then the Fourier transform of the segment signal in the time of is obtained. Moving the center position of the window function $g(t)$ constantly, the Fourier transforms of different times can all be obtained.

From the differences of the local spectrum at different times, we can see the time-frequency feature of the signal clearly. The function $STFT_x(\tau, f)$ reflects the relative content of the signal $x(t)$ component whose frequency is f at the time of τ. Unlike the FFT, the frequency resolution of STFT is not only related to the sampling period (sampling points) but is also dependent on the width of the window function. Equation 4.40 shows the relationship of the frequency resolution Δf, the sampling period T and the width of the window function N:

$$\Delta f = \frac{1}{NT} \tag{4.40}$$

According to equation 4.40, we can realize that by increasing the width of the window, the frequency resolution can be increased as well, thereby increasing the accuracy of the center frequency estimation. However, different window functions have an influence on the width and attenuation speed of the main lobe[129]. According to the characteristics of the FID signal, the Gaussian window is applied, which can improve the SNR of the exponentially decayed signal.

4.3.4 Performance Evaluation

Simulation

Establish the mathematical model for the FID signal based on equation 2.8. For simplified simulation, select $C\mu$ as a suitable constant and set the magnetic field to 49323 nT, corresponding to a frequency of 2100 Hz, and T_2 to 0.5 s. The simulation waveform is shown in Figure 4-13.

Figure 4-13 shows the ideal pure FID signal; however, the FID signal is mixed with noises (mainly white noise) in actual environments as mentioned before, especially the untuned signal, whose SNR is too low to be detected.

Figure 4-14 shows the FID signal that contains useful signal and white noise; according to the analysis of signal noise above, the SNR is set to 5dB, 0dB, and -5dB.

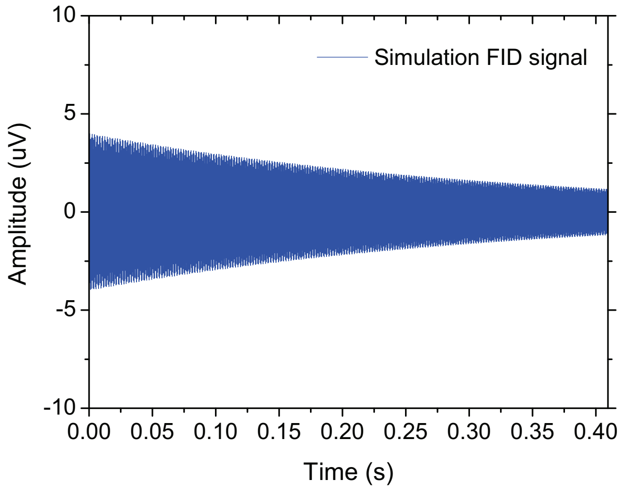

Figure 4-13: Simulation waveform of the FID signal. Sampling rate: 10000 Hz, sampling points: 4096.

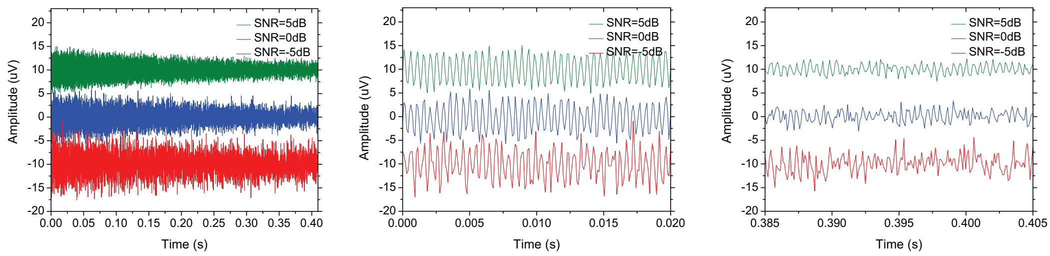

(a) The entire signal. (b) 0 ~ 0.02 s. (c) 0.385 ~ 0.405 s.

Figure 4-14: The ideal FID signals with different SNRs.

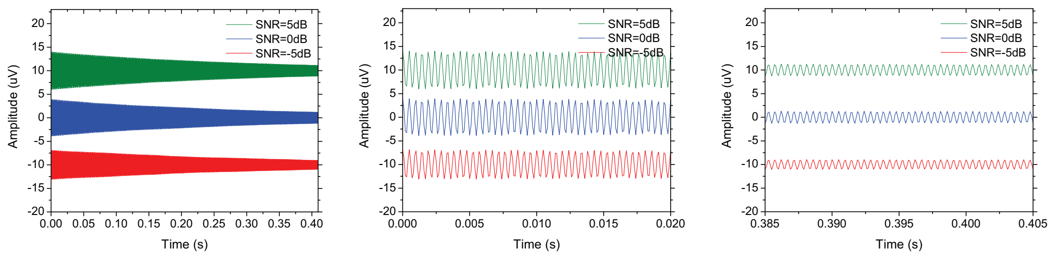

(a) The entire reconstruction. (b) 0 ~ 0.02 s. (c) 0.385 ~ 0.405 s.

Figure 4-15: The reconstructed FID signals with different SNRs.

Figure 4-15 shows the FID signal reconstructed by SVD. According to Figure 4-14 and 4-15 we can realize that, due to the low SNR of the FID signal, especially when the SNR is -5 dB, the useful signal almost cannot be observed in the time domain. However, when the signal is reconstructed, the noise of the signal (SNR = 5 dB, 0 dB) has almost been filtered. Although the amplitude of the reconstructed signal (SNR = -5 dB) is decreased, the curve of the signal is smooth and the overall trend can be observed clearly.

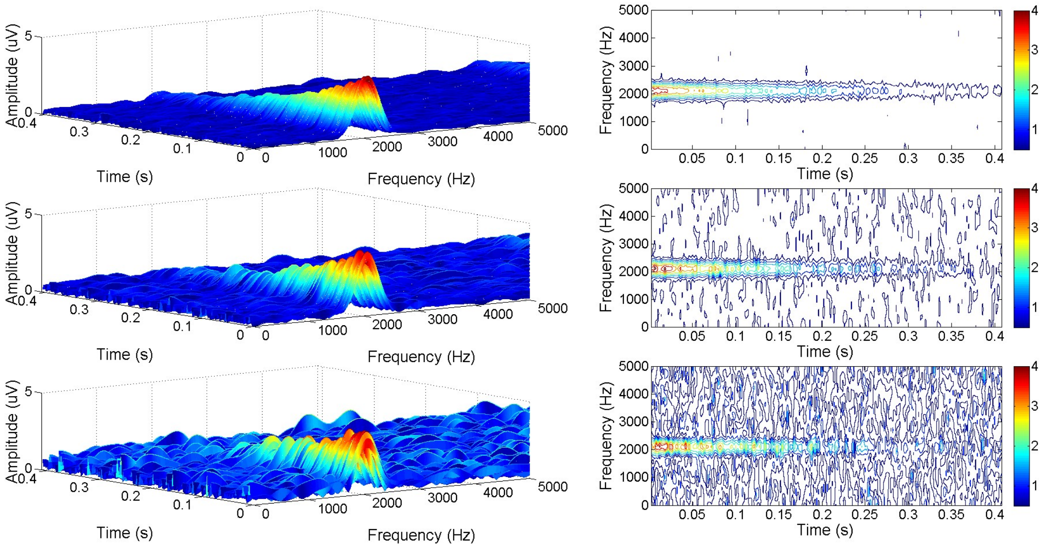

(a) Original FID signal.

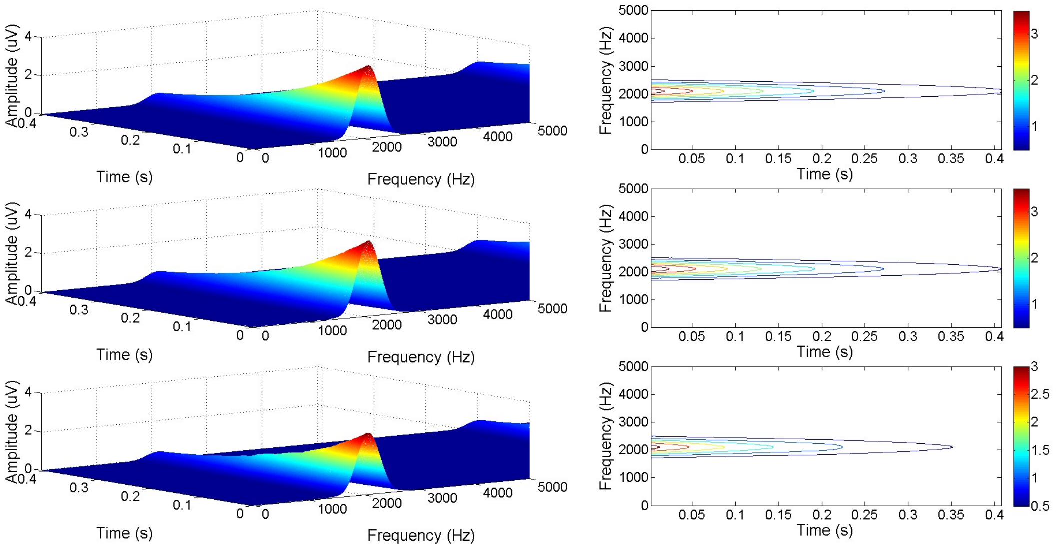

(b) Reconstructed FID signal.

Figure 4-16: The STFT results. From top to bottom, the SNR is 5 dB, 0 dB, and -5 dB; the left column is the 3D image, while the right column is the contour map.

The STFT results of the FID signal with different SNR are shown in Figure 4-16. Figure 4-16a shows the STFT of the original signal, and Figure 4-16b shows the STFT of the reconstructed signal. From Figure 4-16a, we observe that when the SNR of the FID signal is 5 dB, the frequency domain characteristic is significant through STFT, the surface of the three-dimensional image is smooth, and the center frequency of the signal can be obtained accurately. When the SNR is 0 dB, the center frequency can also be obtained; however, from the contour map, there exist miscellaneous frequency signals around the center frequency, which will increase the difficulty of tuning. When the SNR is -5 dB, the FID signal is almost drowned by the miscellaneous frequency signals, and the frequency domain characteristic is not obvious.

In a real environment, if abnormal or significant interference occurs around the sensor, the FID signal will decay rapidly. In addition, due to the low SNR, the quality of the data collected by ADC is poor, which will lead to detuning. In contrast, we can realize from Figure 4-16b that the frequency domain characteristics of the reconstructed signal with different SNR are all significant through STFT, the surface of the three-dimensional images are smooth, and we can accurately obtain that the center frequency of the signal is approximately 2100 Hz.

Based on the simulation study above, we can realize that the SVD can effectively reduce the noise of an FID signal with low SNR (untuned FID signal). The center frequency of the reconstructed signal can be obtained accurately through STFT. The feasibility of the secondary tuning algorithm based on SVD and STFT is verified theoretically.

Test in the Field

Based on the simulation experiments on the FID signal in an ideal environment, the results are encouraging. However, in practical applications, in addition to white noise, the FID signal is also accompanied by interference with phase noise, colored noise, singular noise and random noise (refer to **Section 4.1**). To further verify the proposed algorithm, we adopted the developed prototype to evaluate. Two tests, using either a commonly used tuning algorithm based on the autocorrelation and FFT or the proposed algorithm,

The magnetic field of the test location with less interference is approximately 49323 nT, corresponding to a frequency of 2100 Hz. According to the coil parameters of the sensor, the inductance is 34 mH, the resistance is 19 Ω, and we can calculate that the resonant frequency range is 2072 Hz $\sim$ 2128 Hz, so the passband bandwidth is 56 Hz. The output signal of the sensor was amplified and filtered, and then the ADC was applied to collect the data. The sampling point is 2048 and the sampling rate is 10 kHz, so the frequency resolution is 4.88 Hz.

Figure 4-17 shows the collected actual untuned FID signal; according to the sam-

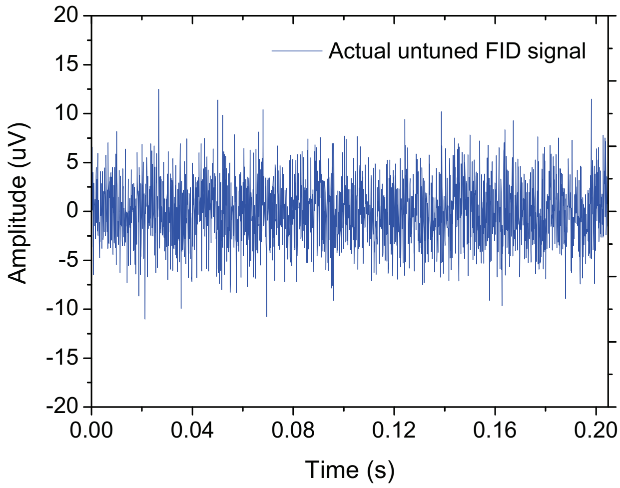

Figure 4-17: The actual untuned FID signal collected by ADC.

pling point and sampling rate, the sampling time is 204.8 ms. Figure 4-18 shows the STFT comparison results of the actual original signal, autocorrelation processed signal and SVD processed signal. From Figure 4-17, we observe that the signal has almost been drowned by noise, and the exponential decay trend of the signal cannot be observed clearly. From Figure 4-18, we observe that:

1) Based on the STFT result of the original signal, in the early stage of signal decay, the center frequency is 2100 Hz, corresponding to the FID signal frequency of the magnetic field at that test location. The longer the time, the smaller the amplitude of the signal, which is consistent with the exponential decay characteristic of the FID signal.

2) Based on the STFT result of the autocorrelation processed signal, we can see that the random noise has been decreased significantly, which can explain how the autocorrelation calculation can eliminate the random noise of the periodic signal. However, there still exists noise interference within 1000 Hz.

3) Based on the STFT result of the SVD processed signal, the random noise has been almost completely filtered out, and the feature of the center band is obvious. The results show that the proposed algorithm is significantly better than the algorithm based on the autocorrelation and FFT.

The test above was in a place with less interference; in practical applications, the external environment cannot be controlled, e.g., weak magnetic anomalies, passing vehicles, etc. will all cause interference for the tuning. To test the environmental adaptability of the proposed algorithm, we placed an iron (100 g) next to the sensor at a distance, which will change the external magnetic field environment around the sensor.

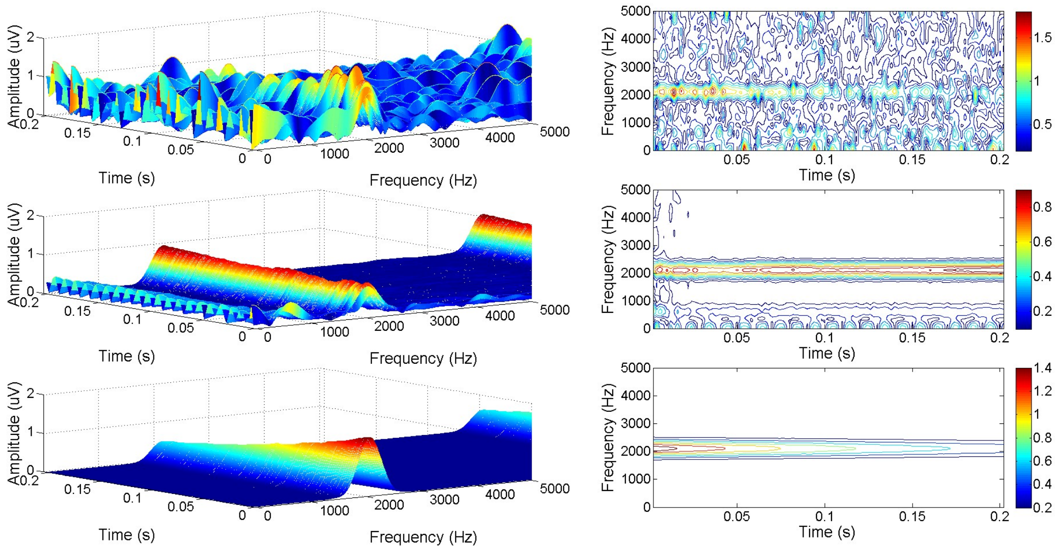

Figure 4-18: Comparison of different tuning algorithms for the FID signal. From top to bottom, the STFT results of the original signal, autocorrelation processed signal and SVD processed signal are shown; the left column is the three-dimensional image, and the right column is the contour map.

The gradient magnetic field will cause a heterogeneous, rapidly decaying FID signal output of the sensor and even cause a serious beat phenomenon, which increases the difficulty of tuning.

Figure 4-19 shows the STFT comparison results of the actual original signal, autocorrelation processed signal and SVD processed signal with environmental disturbance. Figure 4-19a represents the result when the distance from the iron to the sensor is 1 m, while Figure 4-19b represents 0.5 m.

From Figure 4-19a, we observe that:

1) Based on the STFT result of the original signal, we observe that the signal has almost been drowned out by external interference, and the center frequency band feature is not obvious. According to the time-frequency spectrum, there is a maximum amplitude value whose frequency value is 2100 Hz at 25 ms, 50 ms and 80 ms. This indicates that the signal appears to be a beat phenomenon.

2) Based on the STFT result of the autocorrelation-processed signal, we can see that the overall center frequency band is approximately 2100 Hz; however, there still exists a maximum amplitude value at 1000 Hz, 2500 Hz and 3700 Hz. Because the frequency value is in the frequency range of the FID signal, it cannot be removed during signal processing, which will cause interference with the tuning.

3) Based on the STFT result of the SVD-processed signal, we can see that the exter-

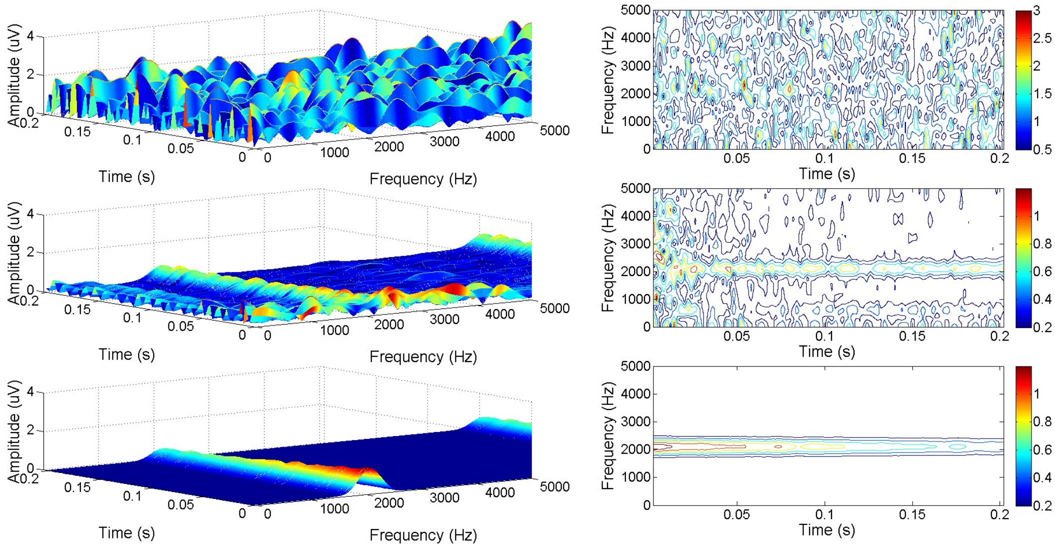

(a) The distance between the iron and sensor is 1m.

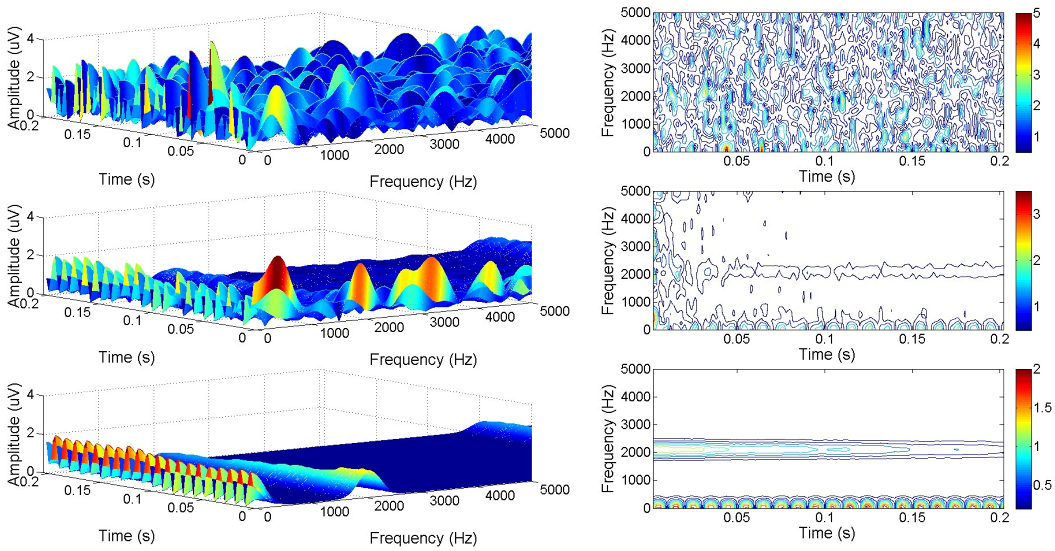

(b) The distance between the iron and sensor is 0.5m.

Figure 4-19: Comparison of different tuning algorithms for the FID signal with environmental disturbance. From top to bottom, the STFT results of the original signal, autocorrelation processed signal and SVD processed signal are shown; the left column is the three-dimensional image, and the right column is the contour map.

nal interference has been decreased significantly, and the center frequency is 2100 Hz, which matches the actual situation and further verifies that the proposed algorithm can suppress the environmental interference effectively.

From Figure 4-19b, we observe that:

1) Based on the STFT results of the original signal, the signal has almost been drowned out by external interference, and the center frequency band feature is not obvious. Moreover, the low-frequency signal interference is more serious.

2) Based on the STFT results of the autocorrelation-processed signal, we can see that the SNR is improved; however, the center frequency band feature is still not obvious. The maximum amplitude value appeared at 500 Hz, 2100 Hz and 3000 Hz, which will affect the accuracy of tuning.

3) Based on the STFT results of the SVD-processed signal, the random noise has been decreased obviously. In addition, there still exist noises below 500 Hz; because the frequency value is not in the frequency range of the FID signal, it can be removed during signal processing. Therefore, this will not cause interference for the tuning. The results further indicate that the proposed algorithm is significantly better than the algorithm based on the autocorrelation and FFT.

From Figure 4-18 and 4-19, we can further observe the processing effects of different algorithms for the FID signal, when the proposed algorithm is applied in practical applications:

Step 1: polarize the sensor for approximately 400 ms, then stop it and delay 5 ms, and enable ADC for signal acquisition for approximately 205 ms.

Step 2: apply the SVD to reconstruct the collected data, and then the STFT is adopted to extract the time-frequency feature to obtain a frequency value f_1 for approximately 50 ms. Based on this frequency value, switch the tuning capacitor to finish the first tuning.

Step 3: polarize the sensor for approximately 200 ms (after the first tuning, the tuning capacitor is open, so this time the signal output of the sensor has a higher SNR and the polarization time does not need to be too long), then stop it and delay 5 ms. Measuring the frequency of the FID signal for approximately 100ms, a frequency value f_2 is obtained. Based on this frequency value, switch the tuning capacitor and set the center frequency of the narrow-band filter to finish the second tuning. The entire process takes less than 1 s; moreover, the tuning result is accurate and repeatable.

According to the experiments above, three tuning algorithm tests using the peak detection, autocorrelation and FFT processing and the proposed method were conducted using the same test platform. The ARM timer was adopted to count the processing time of the three methods. Based on the above findings, the resonant frequency range is 2072Hz $\sim$ 2128Hz in the same magnetic field environment; according to equation 4.27, we can calculate that the tuning capacitance value range is 168nF $\sim$ 173nF. Thus, if the capacitance value obtained by the three methods is within this range, the tuning can be considered successful. The three methods were tested five times in a non-interferential environment, and the results are shown in Table 4.3. According to Table 4.3, we can

Table 4.3: Comparative table of the three methods without interference.

Peak detection		FFT		Proposed	
Cap/nF	Time/s	Cap/nF	Time/s	Cap/nF	Time/s
169	>5	169	1.15	169	0.97
173	>5	169	1.15	169	0.97
168	>5	169	1.15	169	0.97
170	>5	169	1.15	169	0.97
172	>5	169	1.15	169	0.97

observe that:

1) In view of the tuning speed, because the three algorithms are all applied to the sequential program structure, the program execution time is constant. The time taken by the peak detection method is approximately five times that of the FFT method and the proposed method.

2) In view of the tuning precision, the tuning capacitance values obtained by the three algorithms are all in the range 168nF $\sim$ 173nF. Therefore, it can be explained that the performance of the proposed method is comparable to the performance of the autocorrelation and FFT processing method in a non-interferential environment.

Table 4.4 shows the five repetitions of testing results for the three methods in an interferential environment. According to Table 4.4, we can observe that the tuning precision of the peak detection method and the FFT method decreased in an interferential environment. The obtained tuning capacitance value will lead to detuning phenomena, thereby reducing the SNR of the FID signal. Moreover, the instrument cannot be worked normally. However, based on the results of the proposed method, it has higher

Table 4.4: Comparative table of the three methods with interference.

Peak detection		FFT		Proposed	
Cap/nF	Time/s	Cap/nF	Time/s	Cap/nF	Time/s
179	>5	178	1.15	169	0.97
173	>5	173	1.15	169	0.97
165	>5	178	1.15	169	0.97
175	>5	168	1.15	169	0.97
172	>5	163	1.15	169	0.97

accuracy and higher speed than the peak detection method and the autocorrelation and FFT processing method. The external interference has little effect on it, and the results are repeatable, which further prove the superiority of the tuning algorithm based on the SVD and STFT.

Chapter 5

Test

5.1 Laboratory Test

5.1.1 Noise Level

As mentioned in section 3.2.3, aimed to verify the voltage noise and current noise of the preamplifier, as well as the thermal noise of the sensor, the experiment was conducted in this thesis. The preamplifier voltage noise can be measured by shorting the input to ground. The preamplifier current noise can be measured by connecting the input to the sensor[47]. Testing circuits are shown in Figure 5-1a and 5-1b, respectively.

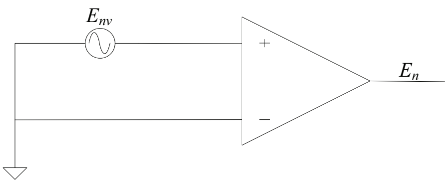

(a) Shorting the input to ground.

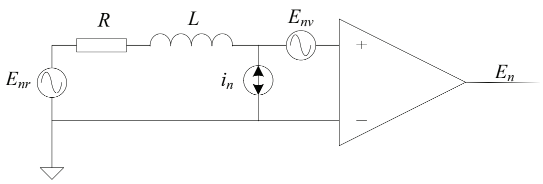

(b) Connecting the input to sensor.

Figure 5-1: Sensor and preamplifier noises test.

From Figure 5-1a, when the input of the preamplifier is shorten to ground. The output noise of the test circuit is related to the voltage noise of the preamplifier as:

$$E_n^2 = E_{nv}^2 \cdot G^2 \tag{5.1}$$

From Figure 5-1b, when the input of the preamplifier is connected to the sensor. The output noise of the test circuit is related to the voltage noise, current noise of the preamplifier, and the thermal noise of the sensor. The noise can be written as:

$$\begin{aligned} E_n^2 &= E_{nv}^2 \cdot G^2 + E_{nr}^2 \cdot G^2 + i_n^2 |R + j\omega L|^2 G^2 \\ &= E_{nv}^2 \cdot G^2 + E_{nr}^2 \cdot G^2 + i_n^2 (R^2 + \omega^2 L)^2 G^2 \end{aligned} \tag{5.2}$$

Obviously, the calculated result of the voltage noise have no correlation with the frequency, which implies it is a constant, while the current noise increases with the increase of frequency. The comparisons between calculated result and measured result of two group testing circuit are shown in Figure 5-2a and 5-2b, respectively.

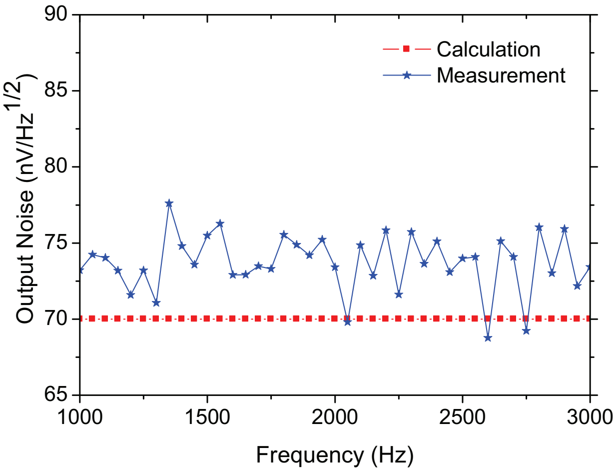

(a) Shorting the input to ground.

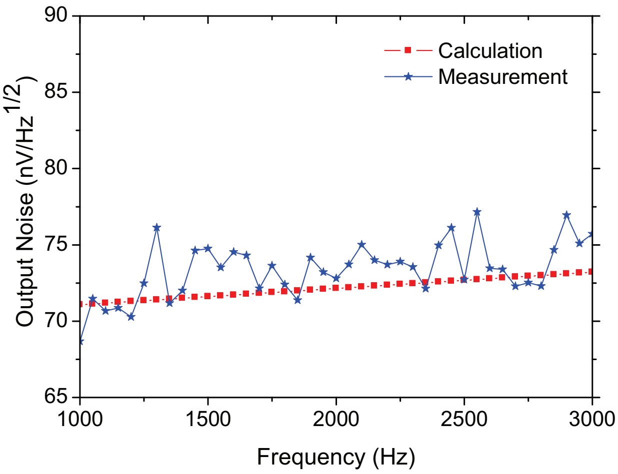

(b) Connecting the input to sensor.

Figure 5-2: Comparison between calculation and measurement.

The measured results are almost all larger than the calculations due to the environment noise and the measuring instrument noise, which will have an effect on the experimental results. However, the measured results are in well agreement with the calculation results overall. Through the comparison experiment, it can be verified that the value of the preamplifier voltage noise and current noise is suitable in the sensor and preamplifier noise model.

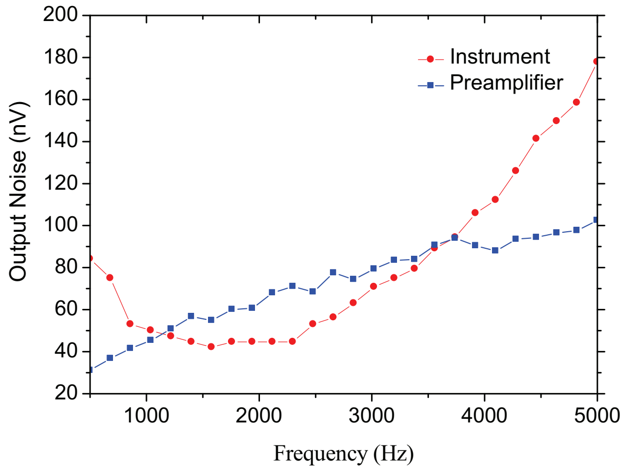

Figure 5-3: Comparison between preamplifier and prototype.

Figure 5-3 shows the output noise of the preamplifier and that of the instrument divided by the corresponding gain as shown in Figure 3-21. The half arc in the curve is due to the signal passing through the passive band-pass filter in the cascade amplifier circuit. The noise level of the preamplifier is comparable to that of the final output of the instrument, which implies that the background noise of the prototype is mainly derived from the preamplifier, the contribution of the post-amplifier is relative small. This is consistent with the Friis formula[131].

5.1.2 FID Signal Strength

As mentioned before, the electromotive force of FID signal generated by Overhauser magnetometer can be formulated by equation 2.8. According to the coil parameters of the sensor(L = 34 mH, R = 19 Ω) mentioned in section 3.1, there is:

$$\mu nAM \approx 6.4 \times 10^{-11} \tag{5.3}$$

If only consider the maximum electromotive force of the FID signal, $\sin^2\theta \times e^{-t/T_2}\sin\omega_0 t$ in equation 2.8 can be regarded as 1. Hence the maximum amplitude can be written as:

$$\varepsilon_{max} = 6.4 \times 10^{-11} \cdot \omega_0 = 6.4 \times 10^{-11} \cdot \gamma_p B_0 \tag{5.4}$$

Therefore, in the range of geomagnetic field from 20000 nT to 100000 nT, the amplitude of the FID signal output of the sensor is 0.34 μV $\sim$ 1.7 μV. Likewise, according to the coil parameters, equation 4.28 can be rewritten as:

$$Q = 0.0119 \cdot f_0 \tag{5.5}$$

According to equation 5.4, 5.5 and 2.9, we can obtained the voltage value of resonant FID signal in the range of geomagnetic field is 3.4 μV $\sim$ 86 μV. However, due to the limitations of the sensor and circuit characteristics, the Q factor of the resonance circuit cannot fully meet the theoretical value. After running some tests, in the range of geomagnetic field from 20000 nT to 100000 nT, the actual voltage value of resonant FID signal is 2 μV $\sim$ 30 μV. The theoretical and actual test results are shown in Figure 5-4.

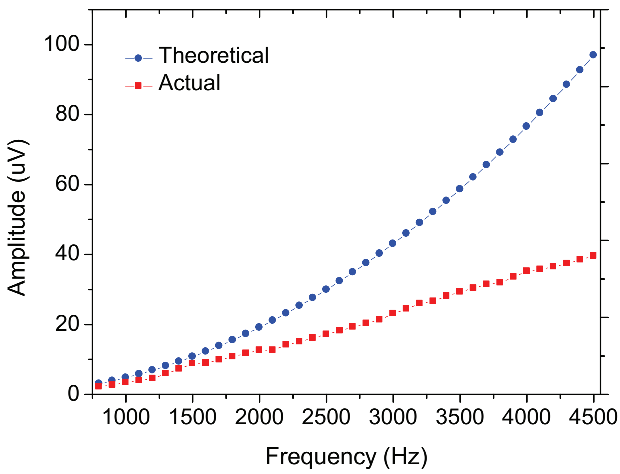

Figure 5-4: Curve of the amplitude of the resonant FID signal.

5.1.3 Frequency Measurement Accuracy

Test the Frequency Measurement Module

According to equation 2.9, the frequency of FID signal is proportional to the strength of magnetic field. Hence, a signal generator is used to generate a standard TTL square wave signal, and input it to the frequency measurement module of test instrument. The measurement time is 500 ms and the test results are shown in Table 5.1 and Figure 5-5, respectively.

Table 5.1: Test results of frequency measurement module (Unit: Hz).

Input signal	Test results	Absolute error	Effective resolution
800.0000	800.0000	0.0000	0.0000
1000.0000	1000.0000	0.0000	0.0001
1500.0000	1500.0000	0.0000	0.0001
2000.0000	2000.0000	0.0000	0.0001
2500.0000	2500.0000	0.0000	0.0001
3000.0000	3000.0001	0.0001	0.0002
3500.0000	3500.0001	0.0001	0.0002
4000.0000	4000.0002	0.0002	0.0002
4100.0000	4100.0002	0.0002	0.0003
4300.0000	4300.0002	0.0002	0.0003

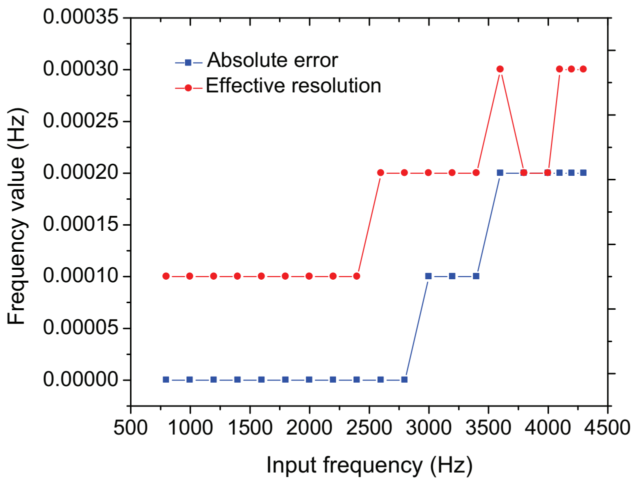

Figure 5-5: Test results of the absolute error and effective resolution.

In this procedure, 100 data are recorded sequentially from each of the measured frequency values during test the absolute error, and the absolute value of the maximum error is the absolute error. In terms of test the effective resolution, first, choose a frequency value and adjust its fourth decimal, which implies 0.0001 Hz. If the test result of the frequency measurement module unchanged, increase the input frequency with a step of 0.0001 Hz until the result changed. The maximum change of the frequency value is the effective resolution.

According to Table 5.1 and Figure 5-5, we observe that in the frequency range from 800 Hz to 4300 Hz, the absolute error of the frequency measurement module is less than 0.0002 Hz and the effective resolution is no more than 0.0003 Hz. If we convert them to magnetic field strength, the absolute error is 0.005 nT and the effective resolution is 0.007 nT.

Test with Micro-signal and Comparison

In general, the original FID signal is very small, the particular voltage is about a few microvolts[132,133], and the signal is so small that it can easily be disturbed by noise. In order to obtain a higher SNR of the FID signal, a resonance circuit is applied. According to the coil parameters of the probe and the Q factor of the resonance circuit, after running some tests, in the range of the geomagnetic field, the actual voltage value of the resonant FID signal is $2 \sim 30\ \mu$V[134]. Therefore, typically, we can simulate the local magnetic field using the signal generator to generate a standard sine wave signal from 800 Hz to 4300 Hz.

The primary voltage of the standard signal can then be divided by the resistance divider into micro signals of less than 10 μV and used as an input for the prototype device. The schematic of the test circuit is shown in Figure 5-6.

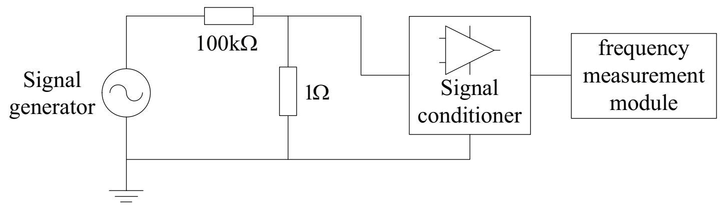

Figure 5-6: Schematic of test circuit.

As mentioned before, in the frequency range of geomagnetic field, the minimum value of original FID signal is about 2 μV. Therefore, if the frequency measurement accuracy can meet the requirement of a high-precision Overhauser magnetometer when the input signal is 2 μV, all the input signal which value is greater than 2 μV can meet the requirement. During the test, 100 data are recorded sequentially from each of the measured frequency values at two different times, and the data processing method is the same as that of the standard signal test. Figure 5-7 shows the test results (measurement time is 500 ms) when the input signal is 2 μV.

According to the Figure 5-7, in the frequency range from 800 Hz to 4300 Hz, the absolute error is less than 0.008 Hz, which converted to magnetic field strength is about 0.19 nT. While that of MSE is less than 0.0025 Hz, which converted to magnetic field strength is about 0.06 nT. Meanwhile, three tests using a single-channel proton magnetometer, a proposed multichannel proton magnetometer, and a commercial Overhauser magnetometer GEM-19, which has the metrological certification, were conducted, re-

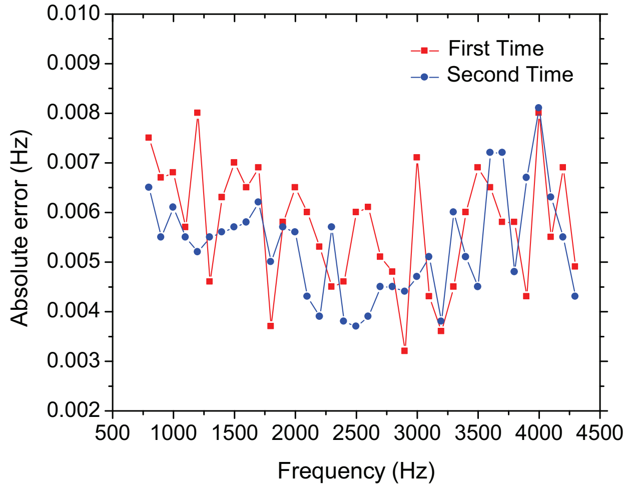

(a) Absolute error.

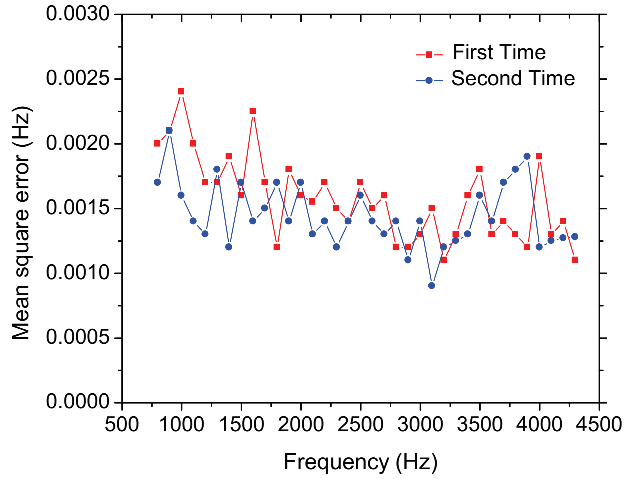

(b) MSE.

Figure 5-7: Test results when input signal is 2 μV.

spectively.

Table 5.2 and Figure 5-8 show the magnetic field absolute error results converted from the frequency measurements versus the peak-peak voltage (Vpp) of the input signal through the resistance divider. From Figure 5-8, we observe that if the Vpp of the input signal decreases, the absolute error of the measured magnetic field will increase and the accuracy will decrease. When Vpp is less than 2 μV, the absolute error is larger than 1 nT if the test is performed with a single-channel device. However, the absolute error is less than 0.15 nT if a multichannel device is used. The accuracy is tremendously improved and is close to that of the Overhauser magnetometer. The sensitivity of frequency measurement can be evaluated by standard deviation, which reflects the degree of deviation of data from the average. The smaller the standard deviation, the better the

Table 5.2: Performance comparison of three methods (Input signal: 2100 Hz).

Input signal	Test results		
Peak to peak (μV)	General (nT)	Multi-channel (nT)	Overhauser (nT)
1	49323.13 $\pm$ 1.30	49323.13 $\pm$ 0.15	49323.13 $\pm$ 0.05
2	49323.13 $\pm$ 1.20	49323.13 $\pm$ 0.13	49323.13 $\pm$ 0.03
3	49323.13 $\pm$ 0.80	49323.13 $\pm$ 0.11	49323.13 $\pm$ 0.02
4	49323.13 $\pm$ 0.50	49323.13 $\pm$ 0.08	49323.13 $\pm$ 0.01
5	49323.13 $\pm$ 0.40	49323.13 $\pm$ 0.07	49323.13 $\pm$ 0.01
6	49323.13 $\pm$ 0.35	49323.13 $\pm$ 0.06	49323.13 $\pm$ 0.01
7	49323.13 $\pm$ 0.30	49323.13 $\pm$ 0.05	49323.13 $\pm$ 0.01
8	49323.13 $\pm$ 0.25	49323.13 $\pm$ 0.04	49323.13 $\pm$ 0.01
9	49323.13 $\pm$ 0.20	49323.13 $\pm$ 0.03	49323.13 $\pm$ 0.01
10	49323.13 $\pm$ 0.20	49323.13 $\pm$ 0.03	49323.13 $\pm$ 0.01

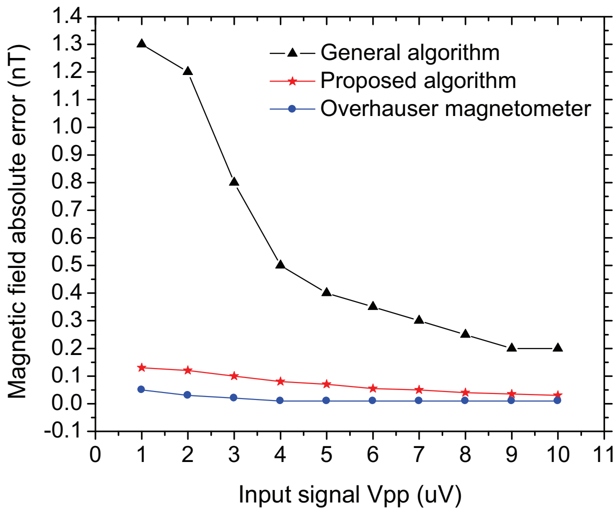

Figure 5-8: Curve of the magnetic field absolute error comparison.

stability and the higher the sensitivity of frequency measurement. Therefore, we can evaluate the sensitivity by calculating the standard deviation of the selected data from each of the three curves. The results are shown in Table 5.3.

According to Table 5.3, the absolute error measured by the prototype device is about 7.75 times (0.55/0.071 $\approx$ 7.75) smaller than that measured by the original device with a single channel. In theory, using the proposed method, we can reduce the error ten times based on equation 4.26. The experimental results agree well with the theoretical prediction. In addition, the sensitivity is reduced to 0.036 nT, which is improved by 11.4 times (0.410/0.036 $\approx$ 11.4). This indicates that the prototype has a higher precision and resolution.

Table 5.3: Comparison of three methods.

	General	Multi-channel	Overhauser
Average (nT)	0.550	0.071	0.017
Standard deviation (nT)	0.410	0.036	0.013

5.1.4 Magnetic Field Measurement Accuracy

The experiment was assembled in an artificial magnetic field generating space shown in Figure 5-9, which consists of a standard magnetic field generator (including a three-axis Helmholtz coil system and a high-precision constant current source) and a magnetically shielded room. Furthermore, due to its location was far away from all electromagnetic sources, this space not only shielded the EMI, but also cancelled the local geomagnetic field. It produced a stable artificial magnetic field of high precision in all directions including **x**, **y**, **z** axis, respectively.

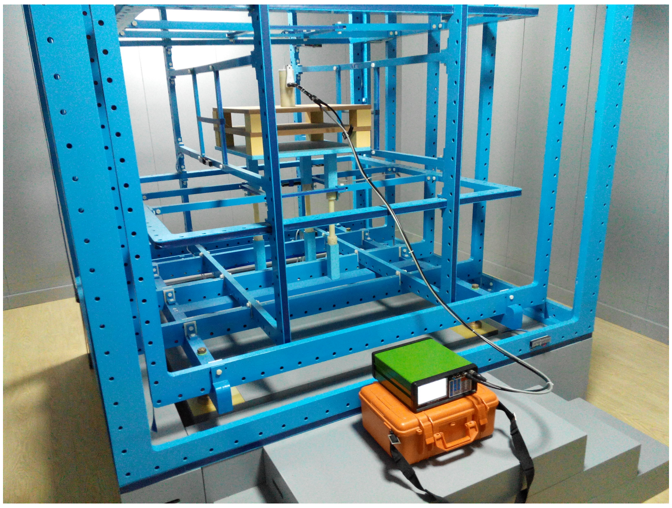

Figure 5-9: Artificial magnetic field generating space.

The generating range of the magnetic field space is from 20000 nT to 100000 nT, and the step value is 10000 nT. Table 5.4 shows the experimental results. We tested 100 points in every corresponding magnetic field that to be measured. First, calculate the average of each corresponding total measured points. Thus the mean square error (MSE) could be obtained. The maximum deviation can be regarded as the measurement accuracy. In this table, five random measured values were given. The measurement range of the proposed prototype can be from 20000 nT to 100000 nT. In addition, the accuracy is changed from 0.18 nT to 1.12 nT over the range of geomagnetic fields, while that of MSE is from 0.10 nT to 0.88 nT. Moreover, the results also show that the accuracy and MSE decrease with the increase of the external magnetic field. From equation 2.8 and 2.9, the initial amplitude of the FID signal is proportional to the precession frequency and extern magnetic field; hence, the performance of the frequency measurement may improve with increasing external magnetic field, which finally leads to an improvement in accuracy and MSE.

Table 5.4: Results of measurement range, accuracy and MSE (Unit: nT).

Standard	1st	2nd	3rd	4th	5th	Absolute accuracy	MSE
19997.41	19997.54	19998.28	19997.39	19996.73	19997.11	1.12	0.88
29995.54	29996.24	29995.63	29995.74	29995.68	29996.39	0.85	0.56
39990.52	39990.58	39990.65	39990.67	39990.75	39990.61	0.38	0.22
49984.71	49984.74	49984.70	49984.85	49984.72	49984.77	0.35	0.21
59978.27	59978.17	59978.23	59978.24	59978.29	59978.38	0.33	0.17
69972.52	69972.56	69972.47	69972.63	69972.45	69972.51	0.30	0.15
79967.85	79967.78	79967.74	79967.70	79967.63	79967.77	0.25	0.13
89959.44	89959.40	89959.38	89959.64	89959.38	89959.39	0.19	0.10
99950.73	99950.77	99950.80	99950.70	99950.65	99950.67	0.18	0.10

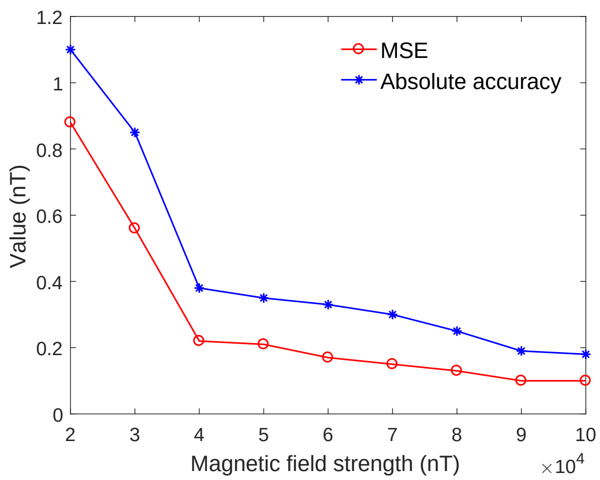

Figure 5-10: The relationship between measurement accuracy or MSE and magnetic field strength.

Figure 5-10 shows the overall relationship between the measurement accuracy or MSE and magnetic field strength. For a magnetometer, the sensitivity is the minimum step of the cymometer used to measure the FID frequency and its conversion into an equivalent magnetic field. Therefore, the sensitivity is actually determined by cymometer based on equation 2.9. Generally, in the magnetometer design, the equivalent magnetic sensitivity can be evaluated by MSE[77]. In consequence, Table 5.4 and Figure 5-10 indicate that the sensitivity of the proposed prototype can reach up to 0.1 nT, implying that the sensitivity of the cymometer is 0.004 Hz. Moreover, when the external magnetic field is larger than 40000 nT, the measurement accuracy is around 0.3 nT.

5.2 Field Test

5.2.1 Geomagnetic Observation

To further verify the performance of the prototype, a comparative test of a geomagnetic field observation was implemented for the prototype and a commercial Overhauser magnetometer in the field for a typical day March 3rd, 2016. The two instruments were installed at Wuhan Jiufeng Seismic Observatory, where was far from EMI sources, and they were separated by 10 m to prevent mutual interference. Moreover, the two instruments were started up simultaneously to avoid the influences from geomagnetic diurnal variations.

Figure 5-11 shows the comparison results. Here the variation of total field in nT versus time in hours is plotted. The trends in the geomagnetic field measurements from the two instruments are basically coincident, although the two curves did not overlap. The baseline difference is about 10 nT. The main cause is the magnetic field gradient at the locations of the sensors. Despite being 10 m apart, the Earth's magnetic field gradient can be ignored. In contrast, with the limitations in test conditions, the fixed magnetic anomaly generated by meteorological instability, passing pedestrians, etc. nearby the sensors also can give rise or fall to a magnetic field gradient. However, such magnetic anomalies are different from random EMI and do not affect a comparison of the two instruments.

To compare the measurement performance of the two instruments, first, the constant magnetic field shift due to the different two devices' locations was removed by the averaging difference of the two curves. Second, excluded the relative larger variations. Third, calculated the MSE of each curve. The 200 samples around 12:00 were chosen as the first data set; while that around 14:00 and 16:00 were chosen as the second and third data set, respectively. Table 5.5 shows the comparison results. The MSE of the two devices are all around 0.3 nT, which indicates that the measurement performance of the proposed prototype is close to that of a commercial Overhauser magnetometer.

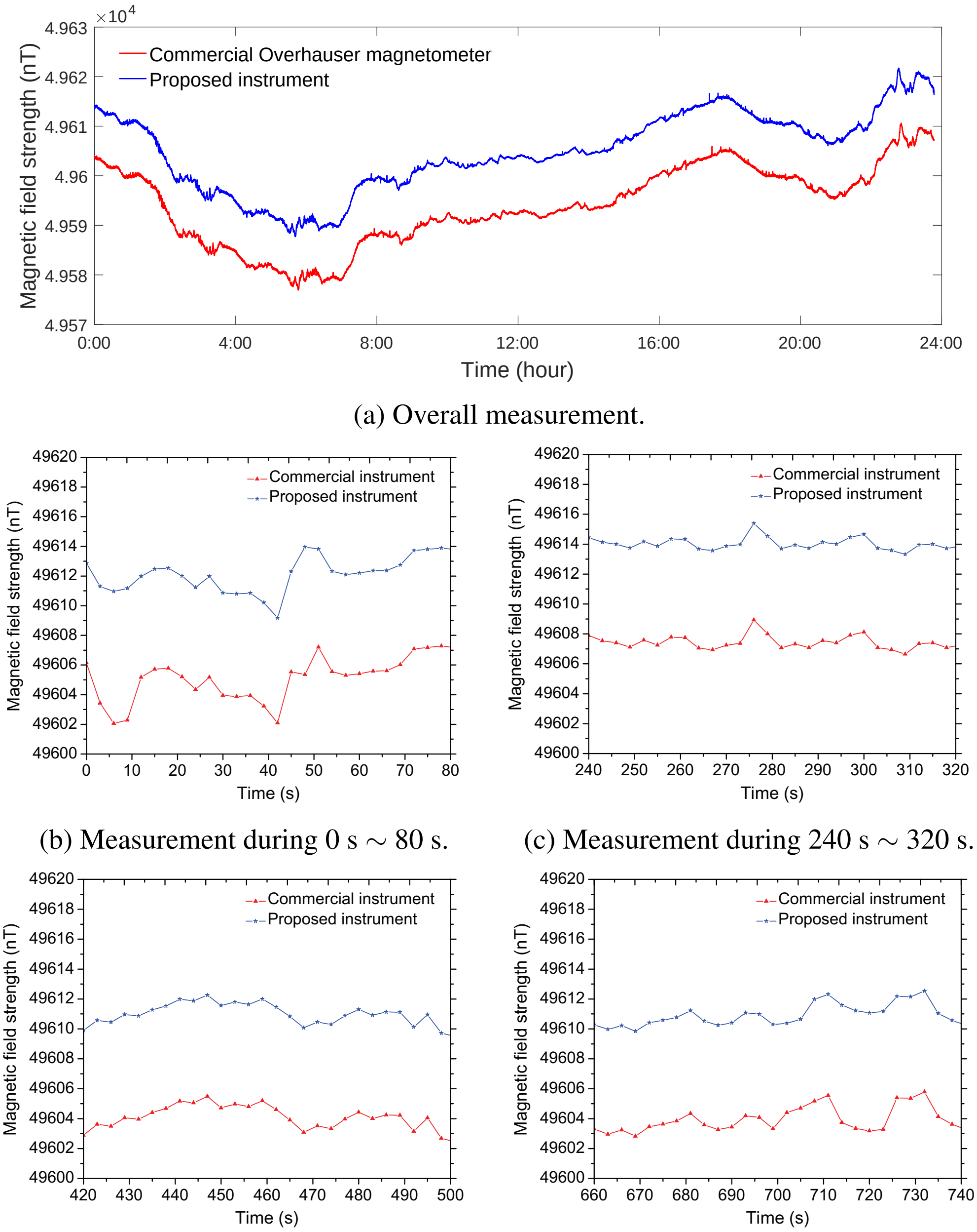

(a) Overall measurement.

(b) Measurement during 0 s ∼ 80 s.

(c) Measurement during 240 s ∼ 320 s.

(d) Measurement during 420 s ∼ 500 s.

(e) Measurement during 660 s ∼ 740 s.

Figure 5-11: The quality of magnetic field data recorded by proposed instrument is compared with that of a commercial Overhauser magnetometer.

5.2.2 Ferromagnetic Target Localization

The object of the ferromagnetic target localization experiment is an iron pipe with a weight of 25 kg. A flat ground of the experiment region is chosen to make sure that the distance between object and the sensor is probably unchanged when the sensor is

Table 5.5: MSE comparison results of two devices (Unit: nT).

Data set	Proposed prototype	Commercial Overhauser magnetometer
First	0.305	0.288
Second	0.317	0.298
Third	0.313	0.295

moved. The length and width of the experiment region are all 10 m. Figure 5-12 shows the schematic diagram of this test and the central coordinate of the iron pipe is (4, 4). The region is cut into 10 $\times$ 10 and the measure step distance is 0.5 m, which means 400 points should be measured in total. The distance of the sensor to the ground is adjustable. The buried depth of the ferromagnetic target is 2 m. Two experiments with different distances (1 m and 2 m) between the sensor and the ground are conducted, respectively. The results are shown in Figure 5-13.

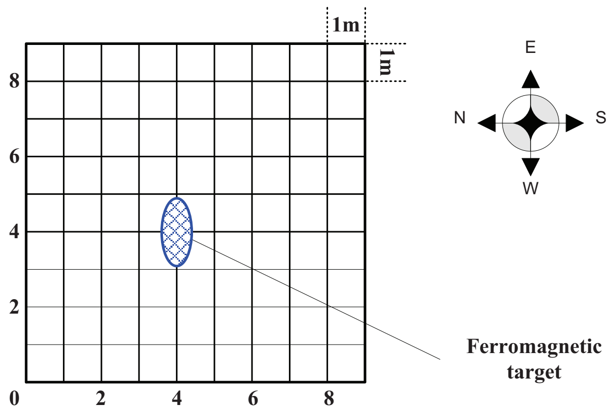

Figure 5-12: Schematic diagram of the test for ferromagnetic target localization.

From Figure 5-13a and 5-13b, there are two relative large magnetic anomaly points at (3, 3) and (5, 5), respectively. It should be the head and the tail of the iron pipe, which generated this kind of distribution characteristic of magnetic field[44]. The central coordinate of the ferromagnetic target is approximately at (4, 4), which is consistent with actual situation. However, there are numerous undulate points that could interfere the accuracy of localization. In Figure 5-13a and 5-13b, the distance between the sensor and the ground is 1 m. Due to the background magnetic field of the experiment region is not well-distributed, which could interfere the magnetic anomaly detection, the distance is increased to 2 m to further suppress this interference. Figure 5-13c and 5-13d shows the results, respectively. The location of ferromagnetic target is indefinite and is

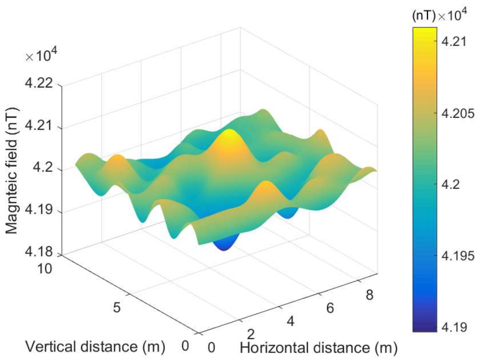

(a) Single sensor test (height of 1 m).

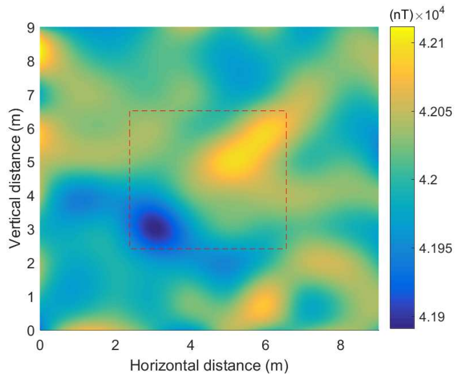

(b) Corresponding 2D image.

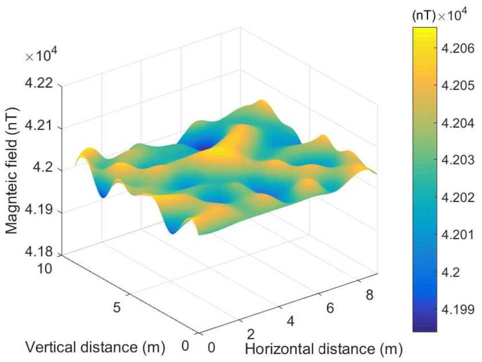

(c) Single sensor test (height of 2 m).

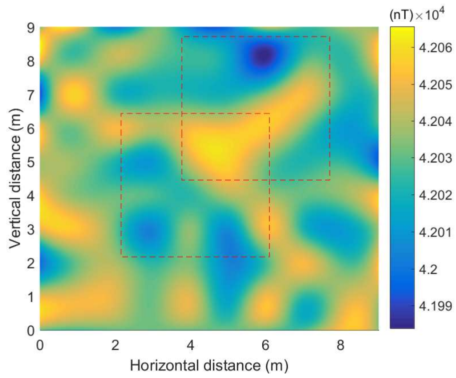

(d) Corresponding 2D image.

Figure 5-13: Comparison of magnetic anomaly survey data by single sensor with height of 1 m and 2 m, respectively.

drown by surrounding magnetic field due to the magnetic density decay of the target. Furthermore, there is an interference in the area around (6, 7), which makes it difficult to locate a magnetic anomaly accurately.

As a weak magnetic detection device, one thing needs to be emphasized that in addition to base station mode, this instrument has another operating mode that is gradiometer mode. This implies that it cannot only operate as a geomagnetic observatory but also measure the magnetic gradient. Then, another experiment is implemented. The distance between two sensors is set as 1 m and the structure of the vertical gradient measurement is adopted. As the same with single sensor test, two experiments with different distances (1 m and 2 m) between the subjacent sensor and the ground are conducted, respectively. The results are shown in Figure 5-14.

From Figure 5-14a and 5-14b, by comparison with Figure 5-13a and 5-13b, the undulations tested by dual sensor are eliminated effectively. The forming surface is much smoother, which indicates that the ability of anti-interference by dual sensor test is stronger than single sensor. Meanwhile, by comparison with Figure 5-13c and 5-13d,

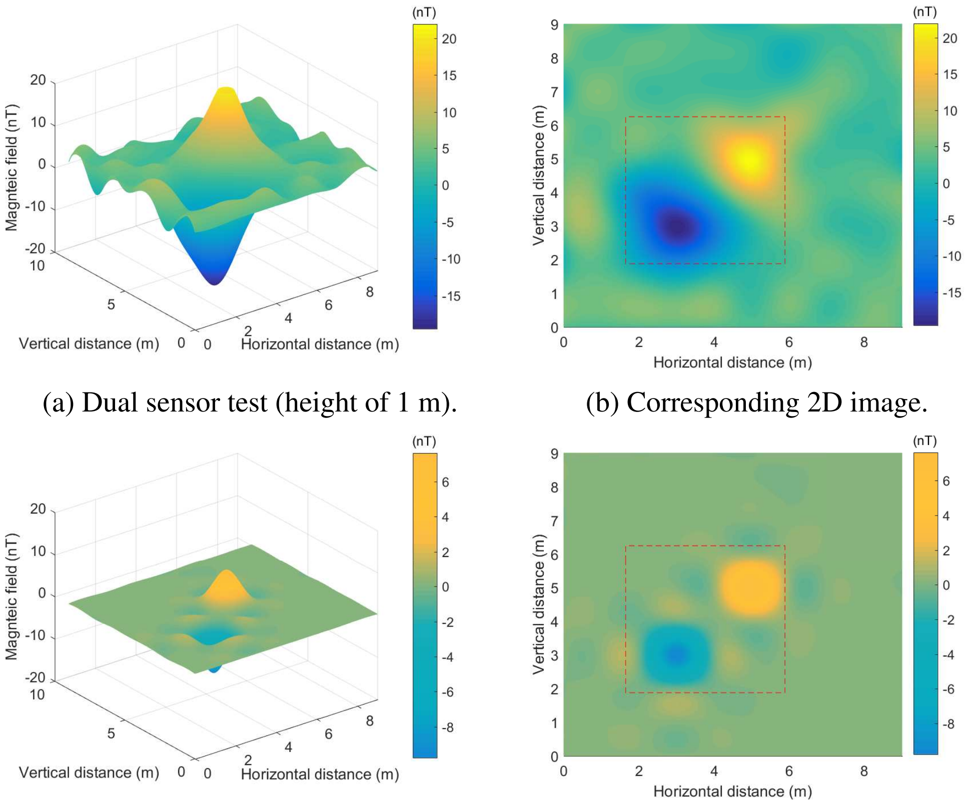

(a) Dual sensor test (height of 1 m).

(b) Corresponding 2D image.

(c) Dual sensor test (height of 2 m).

(d) Corresponding 2D image.

Figure 5-14: Comparison of magnetic anomaly survey data by dual sensor with height of 1 m and 2 m, respectively.

it is still obvious that the central coordinate of the iron pipe is at (4, 4) in Figure 5-14c and 5-14d. The undulations are further eliminated as well as the forming surface, which produces a greater response to the majority of magnetic anomalies than single sensor. It demonstrates that the interference of the background magnetic field is suppressed effectively. However, due to the increase of the distance between the dual sensor and the iron pipe, the absolute magnetic field strength shows an exponential decrease, which lead to the decrease of magnetic gradient at the same time. Therefore, the distance between the sensor and the ferromagnetic target should be adjusted according to different situations.

5.3 Specification

5.3.1 Resolution

The resolution is the smallest change in magnetic field that the magnetometer can resolve or report. It may not be equal to the least-significant digit of the instrument read-out at all settings. Basically, a magnetometer which has a counter resolution is smaller than the smallest change in magnetic field being detected, or quantization errors will result, improperly defining the shape and character of the anomaly. Because the resolution usually varies with sample rate, it is important to make sure that the resolution specification applies to the intended sample rate.

5.3.2 Sensitivity

The sensitivity can be defined as the larger of either the resolution or the noise. With this definition, the sensitivity specification provides a single number that can be used for performance comparison between magnetometers that are limited by their resolution and those that are limited by their noise. Generally, the sensitivity should be specified for all expected speeds of reading and associated bandwidths over a range of magnetic fields characteristic of the Earth and perhaps a range of temperature.

5.3.3 Sample Rate and Cycle Time

Sample rate is defined as the number of readings per second generated by the magnetometer. It is often specified as a frequency of reading in Hz. Cycle time, the number of seconds per reading, is the inverse of the sample rate. When constructing a magnetic-anomaly map, the field has to be sampled at a suitable spatial scale. This special scale should be small compared to the depth of the targets in order for the survey to locate the target accurately. The cycle time of the magnetometer and the speed with which it is moved over the ground determine the distance between measurements. In band-carried devices, the data density can be increased by moving slowly, at the expense of reduce production. In airborne and marine applications, this option is often impractical, as the vehicle may have some minimum operating speed. In any case, the desired sample rate will affect the choice of bandwidth.

5.3.4 Absolute Error and Drift

The absolute error is defined as the difference between the average of the readings of the magnetometer and the average of the field it measures. Drift is defined as the change in the absolute error with time. All magnetometers will have some absolute error and drift in their measurements. In most cases, the drift will be much less than the absolute error.

5.3.5 Gradient Tolerance

Gradient tolerance is defined as the ability of the magnetometer to obtain a meaningful reading a given gradient, not necessarily with the highest sensitivity. When the field has large gradients, errors in assessing the position of the sensor may dominate the error budget, then an increase in noise may be tolerable. Gradient tolerance depends on both the spectral line width and the size of sensor, smaller sensor tends to have high gradient tolerance. Magnetic gradients reduce the amplitude of the magnetometer signal, which can result in increased noise, lower sensitivity and increased dead zone. In applications such as airborne surveys, the sensor is far from field sources, hence gradient tolerance is not an important specification. In surveys of UXO or landfills, gradients can be very large, requiring a magnetometer that tolerates large gradients.

5.3.6 Range of Measurement

The magnetometer are designed to measure the Earth's field over the entire surface of the Earth. As mentioned before, the geomagnetic varies from approximately 20000 nT to 100000 nT. The magnetometer must measure the total field value over this entire range with no increased drift due to changes in the absolute field values. To sum up, according to the laboratory tests and field tests mentioned above, Table 5.6 shows the main technical specifications of the proposed prototype.

Table 5.6: Specifications for the proposed prototype.

Specifications	**Proposed prototype**
Sensitivity	10 pT/Hz$^{1/2}$@1 Hz
Resolution	0.02 nT
Absolute accuracy	$\pm$ 0.3 nT (Sampling rate: 3 seconds)
Dynamic range	20000 nT to 100000 nT
Gradient tolerance	10000 nT/m
Sampling intervals	Optional (Default: 3 seconds)
Operating temperature	0° to 60°C
Tuning mode	Manual and automatic
Power	15V, 800 mA peak during polarization, 200 mA standby
Input/Output	All control communication by keyboard, RS232 and USB link

Chapter 6

Conclusions

6.1 Contribution

The key contribution of this thesis is an improved Overhauser magnetometer combining with digital & analog signal processing algorithms. The contributions are featured with four key elements:

- The noise model of FID signal is first established and different types of noises are investigated, including white noise, narrow-band noise, phase noise, colored noise, random noise and singular noise. The impacts of these noises on FID signal are discussed. Secondly, the relationship between total noise and the error of frequency measurement are formulated. The simulation results show that when the SNR reached up to 10 dB, the improvement of accuracy is not obvious while in the field tests the SNR is about 30 dB. As a whole, the trend of the simulation and the field test results are approximately consistent. The well-known fact that it is possible to get a lower frequency measurement error with a better SNR, which is behind unclear mathematical manipulations, is described in a quantitative way. Moreover, this research can explain why the accuracy of magnetic field measurement with Overhauser or optically pumped magnetometer is better than ordinary proton magnetometer.

- A high-precision multi-channel frequency measurement algorithm is designed. The lab setup experimental data for the single channel, ten channels prototype, and the Overhauser magnetometer GEM-19 show that the ten-channel device improves the accuracy and the sensitivity by more than 7 and 11 times over the single channel device and approaches to those from the Overhauser magnetometer. Furthermore, the field data confirm that the ten-channel prototype device has an accuracy of 0.2 nT that is close to one for the commercial Overhauser magnetometer.

- Through analyzing the current commonly used tuning methods, domestic and foreign, for proton precession magnetometers, a secondary tuning algorithm based on the SVD and STFT is proposed. Based on the simulation and the practical application experiments, the results show that the proposed algorithm has higher accuracy and higher speed (no more than one second) for the tuning performance, even in the interferential environment. The proposed algorithm may make up for the insufficiency of the existing tuning methods by improving the magnetometer's ability to adapt to the environment, thereby solving the detuning phenomenon in the process of measurement.

6.2 Expectation

The future work should be focused on investigating whether a bigger size of the sample or sensor can further indicate the enhancement of the FID signal strength using DNP based approach. In addition, an extensive statistical analysis of other noise sources should be implemented, such as the noises from the magnetometer's sensor and conditioning circuits. A more exhaustive background noise model will be built to quantify the relationship between the SNR and frequency measurement accuracy for FID signal.

Acknowledgments

I would like to express my gratitude and special thanks to my supervisor, Professor Haobin Dong for his enthusiasm, patience and kindness. I have learned many aspects of carrying out research in the field of pattern recognition in the department of Geophysics & Geomatics in the faculty of Geodetection and Information Technology of University of Geosciences Wuhan (CUG), from his comments. Without his encouraging and enlightening guidance, knowledge, persistent support this work would not have been successful. I would also like to thank Jian Ge for his advises and suggestions, and from our fruitful discussions. Many thanks are given to Professors Zheng Liu from University of British Columbia (UBC), who helped me polished the English expression of this paper. Meanwhile, Hanming Gu, Yong He, Shenglin Jiang, Hongwei Li, Xing Jin, who reviewed this thesis and all staffs who have helped me in one way or another and made the time of my doctor thesis pleasurable and memorable both at CUG and UBC.

Bibliography

[1] Khomutov S, Sapunov V, Denisov A, et al. Overhauser vector magnetometer pos-4: Results of continuous measurements during 2015–2016 at geophysical observatory "paratunka" of ikir feb ras, kamchatka, russia[C]. E3S Web of Conferences, 2016: 00007.

[2] Tumanski S. Modern magnetic field sensors–a review[J]. Organ, 2013, 10(13): 1–12.

[3] Choi S, Kim C, Park C, et al. Estimation of hydrothermal deposits location from magnetization distribution and magnetic properties in the north fiji basin [C]. AGU Fall Meeting Abstracts, 2013: 1087.

[4] Mahavarkar P, Singh S, Labde S, et al. The low cost proton precession magnetometer developed at the indian institute of geomagnetism[J]. Journal of Instrumentation, 2017, 12(05): T05002.

[5] Sapunov V, Rasson J, Denisov A, et al. Theodolite-borne vector overhauser magnetometer: Dimover[J]. Earth, Planets and Space, 2006, 58(6): 711–716.

[6] Zikmund A, Janosek M, Ulvr M, et al. Precise calibration method for triaxial magnetometers not requiring earth's field compensation[J]. IEEE Transactions on Instrumentation and Measurement, 2015, 64(5): 1242–1247.

[7] Winslow R M, Johnson C L, Anderson B J, et al. Observations of mercury's northern cusp region with messenger's magnetometer[J]. Geophysical Research Letters, 2012, 39(8).

[8] Enkin N, Liu G, del Carmen Gimenez-Lopez M, et al. A high saturation factor in overhauser dnp with nitroxide derivatives: the role of 14 n nuclear spin relaxation [J]. Physical Chemistry Chemical Physics, 2015, 17(17): 11144–11149.

[9] Tenberg S, McNeil R P, Rubbert S, et al. Narrowing of the overhauser field distribution by feedback-enhanced dynamic nuclear polarization[J]. Physical Review B, 2015, 92(19): 195428.

[10] Seki Y, Kandori A, Hashizume T, et al. Microtesla nmr measurement of protons and fluorine nuclei using a squid gradiometer[J]. IEEE Transactions on Applied Superconductivity, 2013, 23(3): 1600904–1600904.

[11] Hatsukade Y, Abe T, Tsunaki S, et al. Application of ultra-low field hts-squid nmr/mri to contaminant detection in food[J]. IEEE Transactions on Applied Superconductivity, 2013, 23(3): 1602204–1602204.

[12] Martin R, Nazarre D, Périgo E. Traceability of dynamic magnetic fields by nmr magnetometry[C]. Precision Electromagnetic Measurements (CPEM 2014), 2014 IEEE Conference on, 2014: 356–357.

[13] Chukharkin M, Kalabukhov A, Schneiderman J F, et al. Improvement of ultra-low field magnetic resonance recordings with a multilayer flux-transformer-based high-squid magnetometer[J]. IEEE Transactions on Applied Superconductivity, 2013, 23(3): 1602704–1602704.

[14] Denisov A Y, Sapunov V A, Rubinstein B. Broadband mode in proton-precession magnetometers with signal processing regression methods[J]. Measurement Science and Technology, 2014, 25(5): 055103.

[15] Liang S, Yang G, Xu Y, et al. Simultaneously improving the sensitivity and absolute accuracy of cpt magnetometer[J]. Optics express, 2014, 22(6): 6837–6843.

[16] Fang J, Wang T, Zhang H, et al. Optimizations of spin-exchange relaxation-free magnetometer based on potassium and rubidium hybrid optical pumping[J]. Review of Scientific Instruments, 2014, 85(12): 123104.

[17] Belfi J, Bevilacqua G, Biancalana V, et al. Dual channel self-oscillating optical magnetometer[J]. JOSA B, 2009, 26(5): 910–916.

[18] Nikiel A, Blümler P, Heil W, et al. Ultrasensitive 3he magnetometer for measurements of high magnetic fields[J]. The European Physical Journal D, 2014, 68(11): 330.

[19] Packard M, Varian R. Proton gyromagnetic ratio[J]. Phys. Rev, 1954, 93: 941.

[20] Packard M. Free nuclear precession magnetometer[J]. Varian Associates, Palo Alto, California, Report, 1954.

[21] Overhauser A W. Polarization of nuclei in metals[J]. Physical Review, 1953, 92 (2): 411.

[22] Abragam A. Overhauser effect in nonmetals[J]. Physical Review, 1955, 98(6): 1729.

[23] Duret D, Leger J, Frances M, et al. Performances of the ovh magnetometer for the danish oersted satellite[J]. IEEE Transactions On Magnetics, 1996, 32(5): 4935–4937.

[24] Kernevez N, Glenat H. Description of a high sensitivity cw scalar dnp-nmr magnetometer[J]. IEEE Transactions on magnetics, 1991, 27(6): 5402–5404.

[25] Kernevez N, Duret D, Moussavi M, et al. Weak field nmr and esr spectrometers and magnetometers[J]. IEEE transactions on magnetics, 1992, 28(5): 3054–3059.

[26] Sapunov V, Denisov A, Denisova O, et al. Proton and overhauser magnetometers metrology[J]. Contributions to Geophysics & Geodesy, 2001, 31(1): 119–124.

[27] Hrvoic I. Overhauser magnetometers for measurement of the earth's magnetic field[C]. Proceedings of the Magnetic Field Workshop on Magnetic Observatory Instrumentation, Nurmijarvi, Finland, 1989: 15–25.

[28] Hrvoic I. Requirements for obtaining high accuracy with proton magnetometers [C]. Proceedings of the VIth workshop on geomagnetic observatory instruments data acquisition and processing, 1996: 70–72.

[29] Abragam A, Solomon I. Magnetic resonance devices for accurately measuring magnetic fields, in particular low magnetic fields, on board of a movable body [P]. 1968.

[30] Duret D, Bonzom J, Brochier M, et al. Overhauser magnetometer for the danish oersted satellite[J]. IEEE Transactions on magnetics, 1995, 31(6): 3197–3199.

[31] Hrvoic I. Proton magnetometers for measurement of the earth's magnetic field [C]. Proceedings of the International Workshop on Geomagnetic Observatory Data Acquisition and Processing, 1990.

[32] Khomutov S, Kusonsky O, Rasson J, et al. The using of the absolute overhauser magnetometers pos-1 in observatory practice: the results of the first 2.5 years[C]. XI IAGA Workshop on Geomagnetic observatory instruments, data acquisition and processing: Book of abstracts. Kakioka, Japan, 2004: 137.

[33] Hulot G, Eymin C, Langlais B, et al. Small-scale structure of the geodynamo inferred from oersted and magsat satellite data[J]. Nature, 2002, 416(6881): 620–623.

[34] Maus S, Rother M, Holme R, et al. First scalar magnetic anomaly map from champ satellite data indicates weak lithospheric field[J]. Geophysical Research Letters, 2002, 29(14).

[35] Smekalova T N, Smekalov S L, Voss O, et al. Magnetic surveying in archaeology: More than 10 years of using the overhauser gsm-19 gradiometer[M]. Germany: Wormianum, 2008: 12–20.

[36] Zhong Y. New insights into dynamic nuclear polarization under electron nuclear double resonance condition[C]. Magnetic Resonance Microscopy, 2011 Conference on, 2011: 397–398.

[37] Mandea M, Korte M. Geomagnetic observations and models[M]. New York: Springer, 2010: 10–18.

[38] Hovde D, Prouty M, Hrvoic I, et al. Commercial magnetometers and their application[J]. Optical Magnetometry, 2013: 387–405.

[39] Zhang C. Developments of several geophysical methods[J]. Chinese Journal of Engineering Geophysics, 2012, 9(4): 406–412.

[40] Dong H, Zhang C. Developments of several geophysical methods[J]. Chinese Journal of Engineering Geophysics, 2010, 7(4): 460–470.

[41] Tan C, Dong H, Ge Z. Overhauser magnetometer excitation and receiving system design[J]. Chinese Journal of Scientific Instrument, 2010, 31(8): 1867–1872.

[42] Dong H, Tan C, Zhang Y, et al. An overhauser magnetometer[P]. 2010.

[43] Liu H, Dong H, Ge J, et al. Magnetic field gradient detector based on the nuclear overhauser effect[J]. Chinese Journal of Scientific Instrument, 2015, 36(3): 592–600.

[44] Ge J, Lu C, Dong H, et al. The detection technology of near-surface uxo based on magnetic gradient method and overhauser sensor[J]. China Journal of Scientific Instrument, 2015, 36: 38–50.

[45] Wang J, Zhou Q, Zhang S. An rf circuit for overhauser magnetometer excitation[C]. Industrial Control and Electronics Engineering (ICICEE), 2012 IEEE International Conference on, 2012: 494–497.

[46] Zhang S, He J, Chen S, et al. Development of jom-1 model overhauser magnetometer[J]. Journal of Jilin University (Information Science Edition), 2015, 33 (4): 409–415.

[47] Liu T, Gu L, Zhang S, et al. Noise characteristics research of overhauser magnetometer sensor[C]. SPIE Optical Engineering+ Applications, 2015 International Society for Optics and Photonics, 2015: 960728–960728.

[48] Xiao C, Zhang S, Guo X, et al. An improved proton magnetometer for earth's magnetic field observation[C]. SPIE Optical Engineering + Applications, 2015 International Society for Optics and Photonics, 2015: 960729–1–960729–9.

[49] Martin R V, Nazarre D J. Improved nmr magnetometer for weak fields[C]. Precision Electromagnetic Measurements (CPEM 2016), 2016 IEEE Conference on, 2016: 1–2.

[50] Li Z, Chen S, Zhang S, et al. Overhauser magnetometer sensor design for magnetic field observation[C]. SPIE Optical Engineering + Applications, 2016 International Society for Optics and Photonics, 2016: 99690Q–99690Q.

[51] Ge J, Dong H, Liu H, et al. Overhauser geomagnetic sensor based on the dynamic nuclear polarization effect for magnetic prospecting[J]. Sensors, 2016, 16(6): 806.

[52] Liu H, Dong H, Ge J, et al. Research and develop of the test apparatus for measuring the excitation frequency of overhauser magnetometer probe[J]. Acta Electronica Sinica, 2017, 45(2): 1272–1280.

[53] Li Z, Chen S, Zhang S, et al. Overhauser magnetometer sensor design for magnetic field observation[C]. SPIE Optical Engineering + Applications, 2016 International Society for Optics and Photonics, 2016: 99690Q–99690Q.

[54] Davis D G, Bax A. Assignment of complex proton nmr spectra via two-dimensional homonuclear hartmann-hahn spectroscopy[J]. Journal of the American Chemical Society, 1985, 107(9): 2820–2821.

[55] Primdahl F, Merayo J M, Brauer P, et al. Internal field of homogeneously magnetized toroid sensor for proton free precession magnetometer[J]. Measurement Science and Technology, 2005, 16(2): 590.

[56] Lingwood M D, Han S. Dynamic nuclear polarization of 13 c in aqueous solutions under ambient conditions[J]. Journal of Magnetic Resonance, 2009, 201 (2): 137–145.

[57] Benial A M F, Ichikawa K, Murugesan R, et al. Dynamic nuclear polarization properties of nitroxyl radicals used in overhauser-enhanced mri for simultaneous molecular imaging[J]. Journal of magnetic resonance, 2006, 182(2): 273–282.

[58] Armstrong B D, Han S. A new model for overhauser enhanced nuclear magnetic resonance using nitroxide radicals[J]. The Journal of chemical physics, 2007, 127(10): 104508.

[59] Griesinger C, Bennati M, Vieth H M, et al. Dynamic nuclear polarization at high magnetic fields in liquids[J]. Progress in nuclear magnetic resonance spectroscopy, 2012, 64: 4–28.

[60] Dhas M K, Utsumi H, Jawahar A, et al. Dynamic nuclear polarization properties of nitroxyl radical in high viscous liquid using overhauser-enhanced magnetic resonance imaging (omri)[J]. Journal of Magnetic Resonance, 2015, 257: 32–38.

[61] Lingwood M D, Siaw T A, Sailasuta N, et al. Continuous flow overhauser dynamic nuclear polarization of water in the fringe field of a clinical magnetic resonance imaging system for authentic image contrast[J]. Journal of Magnetic Resonance, 2010, 205(2): 247–254.

[62] Arora K, Cazenave A, Engdahl E R, et al. Encyclopedia of solid earth geophysics [M]. New York: Springer Science & Business Media, 2011: 10–20.

[63] Close D, Malanify J, Umbarger C. Detection of the stable isotopes of carbon using a 3-mv van de graaff and the application to environmental and biological studies[J]. IEEE Transactions on Nuclear Science, 1974, 21(1): 731–734.

[64] Naito A, Ganapathy S, McDowell C. High resolution solid state 13c nmr spectra of carbons bonded to nitrogen in a sample spinning at the magic angle[J]. The Journal of Chemical Physics, 1981, 74(10): 5393–5397.

[65] Hartmann S, Hahn E. Nuclear double resonance in the rotating frame[J]. Physical Review, 1962, 128(5): 2042.

[66] Chen W. Nuclear magnetic resonance geophysical instrument theory[M]. Beijing: Geological Publishing House, 1992: 80–100.

[67] Ge J, Zhao Z, Dong H, et al. Design of the magnetic field sensor for proton precession magnetometer based on dc pulse polarization[J]. Chinese Journal of Scientific Instrument, 2014, 35(4): 850–858.

[68] Primdahl F. Scalar magnetometers for space applications[J]. Geophysical Monograph-Geophysical Union, 1998, 103: 85–100.

[69] Armstrong B D, Soto P, Shea J E, et al. Overhauser dynamic nuclear polarization and molecular dynamics simulations using pyrroline and piperidine ring nitroxide radicals[J]. Journal of Magnetic Resonance, 2009, 200(1): 137–141.

[70] Yang A, Yang G, Cai X, et al. A laser pump-re-pump atomic magnetometer[J]. Chinese Physics B, 2013, 22(12): 120702.

[71] Lobo N P, Ramanathan K. Combining adiabatic and hartmann–hahn cross-polarization for sensitivity enhancement in solid state separated local field 2d-nmr experiments of partially ordered systems[J]. Chemical Physics Letters, 2012, 536: 155–161.

[72] Lingwood M D, Ivanov I A, Cote A R, et al. Heisenberg spin exchange effects of nitroxide radicals on overhauser dynamic nuclear polarization in the low field limit at 1.5 mt[J]. Journal of Magnetic Resonance, 2010, 204(1): 56–63.

[73] Ma C, Yuan X, Han Y, et al. Study of a 3rd-harmonic 0.6 thz gyrotron[J]. Acta Electronica Sinica, 2012, 3: 015.

[74] Fan S, Chen S, Zhang S, et al. An improved overhauser magnetometer for earth's magnetic field observation[C]. SPIE Optical Engineering+ Applications, 2016 International Society for Optics and Photonics, 2016: 99721N–99721N.

[75] Zhang Z, Lin J, Zhou Y, et al. Analysis and decoupling design of a 30 mhz resonant sepic converter[J]. IEEE Transactions on Power Electronics, 2016, 31 (6): 4536–4548.

[76] Liu H, Dong H, Liu Z, et al. Noise characterization for the fid signal from proton precession magnetometer[J]. Journal of Instrumentation, 2017, 12(07): P07019.

[77] Dong H, Liu H, Ge J, et al. A high-precision frequency measurement algorithm for fid signal of proton magnetometer[J]. IEEE Transactions on Instrumentation and Measurement, 2016, 65(4): 898–904.

[78] Yi X, Lin J, Ge J, et al. Research and development of portable nuclear magnetic resonance groundwater exploration instrument based on double-turn coils [J]. Chinese Journal of Sensors and Actuators, 2013, 34(1): 1–10.

[79] Zhang S, Zhou Q, Chen S, et al. Design of jpm-1 proton magnetometer based on dsp[J]. Journal of Jilin University (Information Science Edition), 2014, 32(5): 509–515.

[80] Liu H, Dong H, Ge J, et al. Research on a secondary tuning algorithm based on svd & stft for fid signal[J]. Measurement Science and Technology, 2016, 27(10): 105006.

[81] Li T, Feng L, Duan Q, et al. Research and realization of short dead-time surface nuclear magnetic resonance for groundwater exploration[J]. IEEE Transactions on Instrumentation and Measurement, 2015, 64(1): 278–287.

[82] Wang H, Dong H, Xue X, et al. The study of proton magnetometer precession signal extraction technology[J]. Journal of Information and Computational Science, 2012, 9: 3753–3260.

[83] Lu Y, Joshi S, Morris J M. Noise reduction for nmr fid signals via gabor expansion[J]. IEEE Transactions on Biomedical Engineering, 1997, 44(6): 512–528.

[84] Zygarlicki J, Mroczka J. Prony's method with reduced sampling–numerical aspects[J]. Metrology and Measurement Systems, 2014, 21(3): 521–534.

[85] Wang H, Dong H, He L, et al. The study of matrix mathematical model construction of ppm fid signal associate with fdm.[J]. Journal of Convergence Information Technology, 2012, 7(16): 169–178.

[86] Nakao T, Furukawa T, Suematsu T, et al. Intensity estimation method of the fid signal based on the high-order prony method including evaluation used to the priori information in quantitative nmr[C]. Signal Processing and Information Technology (ISSPIT), 2014 IEEE International Symposium on, 2014: 000067–000072.

[87] Babayeva M, Kober T, Knowles B, et al. Accuracy and precision of head motion information in multi-channel free induction decay navigators for magnetic resonance imaging[J]. IEEE Transactions on Medical Imaging, 2015, 34(9): 1879–1889.

[88] Nakao T, Furukawa T, Suematsu T, et al. Application of intensity estimation method of the fid signal based on the high-order prony estimation method and selective evaluation criterion to purity estimation in quantitative nmr, dependence of the 13 c decoupling and the sample spinning[C]. Intelligent Signal Processing and Communication Systems (ISPACS), 2014 International Symposium on, 2014: 165–170.

[89] collaboration C, et al. Performance of electron reconstruction and selection with the cms detector in proton-proton collisions at sqrt (s)= 8 tev[J]. Journal of Instrumentation, 2015, 10(6): P06005.

[90] McDonough R N, Whalen A D. Detection of signals in noise[M]. New Jersey: Academic Press, 1995: 110–120.

[91] Scharf L L. Statistical signal processing[M]. Colorado: Addison-Wesley Reading, MA, 1991: 60–88.

[92] Davenport W B, Root W L, et al. An introduction to the theory of random signals and noise[M]. New York: McGraw-Hill, 1958: 65–85.

[93] Doucet A, De Freitas N, Gordon N. An introduction to sequential monte carlo methods[M]. New York: SMC Practice. Springer Verlag, 2001: 3–14.

[94] Wang H. The study of proton magnetometer fid signal processing algorithm[D]. China: University of Geosciences (Wuhan), 2012.

[95] Atkin E, Ivanov V, Ivanov P, et al. Development of the read-out asic for muon chambers of the cbm experiment[J]. Journal of Instrumentation, 2015, 10(4): C04006.

[96] Reza M S, Ciobotaru M, Agelidis V G. Power system frequency estimation by using a newton-type technique for smart meters[J]. IEEE Transactions on Instrumentation and Measurement, 2015, 64(3): 615–624.

[97] Ghadiri Modarres M, Mojiri M, Karimi Ghartemani M. New adaptive algorithm for delay estimation of sinusoidal signals with unknown frequency[J]. IEEE Transactions on Instrumentation and Measurement, 2015, 64(9): 2360–2366.

[98] Khan N A, Boashash B. Instantaneous frequency estimation of multicomponent nonstationary signals using multiview time-frequency distributions based on the adaptive fractional spectrogram[J]. IEEE Signal Processing Letters, 2013, 20(2): 157–160.

[99] Andersson F, Carlsson M, Tourneret J Y, et al. A new frequency estimation method for equally and unequally spaced data[J]. IEEE Transactions on Signal Processing, 2014, 62(21): 5761–5774.

[100] Buajarern J, Phuaknoi P, Ranusawud M, et al. Absolute frequency measurement by using optical frequency comb technique[C]. Electrical Engineering/Electronics, Computer, Telecommunications and Information Technology (ECTI-CON), 2013 10th IEEE International Conference on, 2013: 1–4.

[101] Darvin R C, Paranjape H, Mohanan S K, et al. Analysis of autocorrelation based frequency measurement algorithm for ifm receivers[C]. Electronics, Computing and Communication Technologies (IEEE CONECCT), 2014 IEEE International Conference on, 2014: 1–6.

[102] Emami H, Ashourian M. Improved dynamic range microwave photonic instantaneous frequency measurement based on four-wave mixing[J]. IEEE Transactions on Microwave Theory and Techniques, 2014, 62(10): 2462–2470.

[103] Lindner S, Vinci G, Barbon F, et al. Instantaneous frequency measurement based on low-cost six-port technology[C]. Microwave Conference (EuMC), 2013 European, 2013: 460–463.

[104] He T, Chen X, Hong L. High-precision frequency detection with apfft based on fpga[J]. Electronic Measurement Technology, 2013, 36(8): 80–83.

[105] Dong C, Ren L. The design of all-phase fft cymometer based on dsp[C]. Systems and Informatics (ICSAI), 2012 IEEE International Conference on, 2012: 303–305.

[106] Wang X, An G, Zhang X. Measurement frequency algorithm of weighted phase difference and its application in engineering[J]. Journal of Hebei University of Science and Technology, 2013, 34(5): 446–450.

[107] Li B, Xu J, Wei B. Implementation of instantaneous frequency measurement based on phase difference by fpga[J]. Modern Electronic Technology, 2013, 36 (010): 110–120.

[108] Ye F, Jiao Y, Zhou D, et al. A high-accuracy algorithm of frequency measurement based on fourier algorithm[J]. Power System Protection and Control, 2012, 40 (8): 44–48.

[109] Zhang P, Wang H, Li L, et al. Fpga-based high accuracy burst carrier frequency measurement method[J]. Electronics Letters, 2014, 50(14): 1026–1027.

[110] Malpani R, Abbas Z, Swarup K S. High precision frequency estimation using internet-based phasor measurement unit[J]. IEEE Transactions on Power Systems, 2010, 25(2): 607–614.

[111] Snyder I, Smith T. Frequency measurement methods and impact in presence of frequency responsive loads and distributed energy resources[C]. Power Systems Conference (PSC), 2014 Clemson University, 2014: 1–5.

[112] Welter L, Dreux P, Portal J M, et al. Embedded high-precision frequency-based capacitor measurement system[C]. On-Line Testing Symposium (IOLTS), 2013 IEEE 19th International, 2013: 116–121.

[113] Rutman J. Characterization of phase and frequency instabilities in precision frequency sources: Fifteen years of progress[J]. Proceedings of the IEEE, 1978, 66 (9): 1048–1075.

[114] Park P G, Kim W, Kim M, et al. Measurement and analysis of earth's magnetic field based on low-magnetic field standards[C]. Precision Electromagnetic Measurements (CPEM 2014), 2014 IEEE Conference on, 2014: 358–359.

[115] Sohn S, DelaBarre L, Vaughan J T, et al. 8-channel rf head coil of mri with automatic tuning and matching[C]. Microwave Symposium Digest (IMS), 2013 IEEE MTT-S International, 2013: 1–3.

[116] Tsai P, Ho C, Chen R, et al. Sensitivity integrity for tool monitoring, tuning and matching[C]. e-Manufacturing and Design Collaboration Symposium (eMDC), 2014 IEEE Conference on, 2014: 1–2.

[117] Karpov G. Pulsed nuclear magnetic resonance magnetometer[J]. Optoelectronics, Instrumentation and Data Processing, 2015, 51(1): 58–63.

[118] Latip M A, Salleh M M, Ab Wahab N. Tuning circuit based on varactor for tunable filter[C]. RF and Microwave Conference (RFM), 2011 IEEE International, 2011: 26–28.

[119] Sun Y, Moritz J, Zhu X. Adaptive impedance matching and antenna tuning for green software-defined and cognitive radio[C]. Circuits and Systems (MWSCAS), 2011 IEEE 54th International Midwest Symposium on, 2011: 1–4.

[120] Lin T, Zhang Y, Lee Y, et al. High-sensitivity cooled coil system for nuclear magnetic resonance in khz range[J]. Review of scientific instruments, 2014, 85 (11): 114708.

[121] Wang T, Wang S. Frequency-tuning negative-conductance boosted structure and applications for low-voltage low-power wide-tuning-range vco[J]. IEEE Transactions on Very Large Scale Integration (VLSI) Systems, 2015, 23(6): 1137–1144.

[122] Chao T, Haobin D. The study of proton magnetometer sensor fast tuning algorithm based on fft[C]. Electric Information and Control Engineering (ICEICE), 2011 IEEE International Conference on, 2011: 3747–3750.

[123] Mitra P, Gunjan R, Gaur M S. A multi-resolution watermarking based on contourlet transform using svd and qr decomposition[C]. Recent Advances in Computing and Software Systems (RACSS), 2012 IEEE International Conference on, 2012: 135–140.

[124] Winck R C, Book W J. The svd system for first-order linear systems[J]. IEEE Transactions on Control Systems Technology, 2015, 23(3): 1213–1220.

[125] Lee M, Choi C. Incremental *n*-mode svd for large-scale multilinear generative models[J]. IEEE Transactions on Image Processing, 2014, 23(10): 4255–4269.

[126] Li M, Bi W, Kwok J T, et al. Large-scale nyström kernel matrix approximation using randomized svd[J]. IEEE Transactions on Neural Networks and Learning Systems, 2015, 26(1): 152–164.

[127] Wang H, Cao M, Wang D, et al. The study of access frequency extraction technology of intelligent substation based on svd[J]. Journal of Information and Computational Science, 2014, 11(7): 2275–2282.

[128] Kalman D. A singularly valuable decomposition: the svd of a matrix[J]. The college mathematics journal, 1996, 27(1): 2–23.

[129] Kim B, Kong S, Kim S. Low computational enhancement of stft-based parameter estimation[J]. IEEE Journal of Selected Topics in Signal Processing, 2015, 9(8): 1610–1619.

[130] Krawczyk M, Gerkmann T. Stft phase reconstruction in voiced speech for an improved single-channel speech enhancement[J]. IEEE/ACM Transactions on Audio, Speech, and Language Processing, 2014, 22(12): 1931–1940.

[131] Friis H T. Noise figures of radio receivers[J]. Proceedings of the IRE, 1944, 32 (7): 419–422.

[132] Babilotte P, Coudert L H, Billard F, et al. Experimental and theoretical study of free induction decay of water molecules induced by terahertz laser pulses[J]. Physical Review A, 2017, 95(4): 043408.

[133] Liu H, Dong H B, Ge J, et al. An improved tuning control algorithm based on svd for fid signal[J]. Journal of Advanced Computational Intelligence and Intelligent Informatics, 2017, 21(1): 133–138.

[134] Nartowska E, Kozłowski T, Kolankowska M. Fid signal intensity in the nmr studies of cohesive soils at the positive temperature range[J]. Structure and Environment, 2016, 8(3): 179–182.